SLAC-R-1016

Investigation of the Charmless Decay B+- \rightarrow K+- K-+ K+- Using a Dalitz Plot Analysis at BaBar

By Alistair Jepson Hart

September, 2006

SLAC National Accelerator Laboratory, Stanford University, Stanford CA 94309

Work funded in part by DOE Contract DE-AC02-76SF00515

Investigation of the Charmless Decay $B^{\pm} \to K^{\pm}K^{\mp}K^{\pm}$ using a Dalitz Plot analysis at *BABAR*

Alistair Jepson Hart

A thesis submitted for the degree of
Doctor of Philosophy

Particle Physics Group,
School of Physics and Astronomy,
University of Birmingham.

September 2006.

Abstract

Results of an amplitude analysis of the $B^{\pm} \to K^{\pm}K^{\mp}K^{\pm}$ Dalitz plot are presented. The analysis is made using an integrated luminosity of $210.6\,\mathrm{fb}^{-1}$, recorded by the *BABAR* detector at the PEP-II asymmetric B Factory. This dataset corresponds to 231.8 million $B\overline{B}$ pairs.

Branching fractions and 90% confidence level upper limits are calculated and averaged over charge conjugate states ($\mathcal{B}$). For those modes that have significant branching fraction measurements *CP* violating charge asymmetry measurements are also presented (A_{CP}). However the asymmetry for all modes is consistent with zero.

A feature is found around $1.5\,\mathrm{GeV}/c^2$ that corresponds to no known resonance. We measure it to be a scalar resonance of mass $(1.523^{+0.028}_{-0.020})\,\mathrm{GeV}/c^2$ and width $(175^{+32}_{-27})\,\mathrm{MeV}/c^2$. It is listed here as $(KK)^0_0$. The results from the nominal fit are summarised below:

$$
\begin{aligned}
\mathcal{B}(B^{\pm} \to K^{\pm}K^{\mp}K^{\pm}\ \text{Inclusive}) &= (35.1 \pm 1.3 \pm 2.1) \times 10^{-6} \\
\mathcal{B}(B^{\pm} \to K^{\pm}K^{\mp}K^{\pm}\ \text{Non}-\text{resonant}) &= (18.6 \pm 3.4 \pm 1.8) \times 10^{-6} \\
\mathcal{B}(B^{\pm} \to \phi(1020)K^{\pm}; \phi(1020) \to K^+K^-) &= (4.3 \pm 0.6 \pm 0.3) \times 10^{-6} \\
\mathcal{B}(B^{\pm} \to f_0(980)K^{\pm}; f_0(980) \to K^+K^-) &= (8.7 \pm 3.1 \pm 1.4) \times 10^{-6} \\
\mathcal{B}(B^{\pm} \to (KK)^0_0K^{\pm}; (KK)^0_0 \to K^+K^-) &= (3.3 \pm 1.1 \pm 0.7) \times 10^{-6} \\
\mathcal{B}(B^{\pm} \to \chi_{c0}K^{\pm}; \chi_{c0} \to K^+K^-) &= (1.7 \pm 0.5 \pm 0.1) \times 10^{-6} \\
\mathcal{B}(B^{\pm} \to \phi(1680)K^{\pm}; \phi(1680) \to K^+K^-) &< 1.5 \times 10^{-6}
\end{aligned}
$$

$$\mathcal{B}(B \to f_2(1270)K^{\pm}; f_2(1270) \to K^+K^-) < 1.1 \times 10^{-6}$$

$$\mathcal{B}(B \to f_2'(1525)K^{\pm}; f_2'(1525) \to K^+K^-) < 2.4 \times 10^{-6}$$

$$\mathcal{B}(B \to f_0(1710)K^{\pm}; f_0(1710) \to K^+K^-) < 3.3 \times 10^{-6}$$

Acknowledgements

Firstly I would like to thank PPARC for funding me through this degree and the University of Birmingham Particle Physics Group for the opportunity that they have given me. On that note I'd also like to thank my supervisor Alan Watson for being a helping hand whenever I needed his advice and Chris Hawkes for essentially being an additional supervisor.

As regards my work on this analysis I must thank Matt for being a sounding-board and reliably remembering all the details that I am apt to forget. Tom, Sian and John for their experience, knowledge and general helpfulness.

I'd like to thank Kelly for everything she did to help me settle into life in California and for the TV! A special mention should also be made for Mitch, Jim, Wahid, Nick and (occasionally) Jamie and Debbie for the car-pooling scheme we shared which made the daily commute to SLAC far more bearable.

Other friends who made my time in California such great fun (in no particular order) include Ian, Stevo, Mike, Paul, Dave, Will, Edd, JamieG, Katherine and Mani — I couldn't have hoped to meet a finer bunch of physicists.

In Birmingham I'd like to thank Tam for her humour, convictions and considerable generosity in always attempting to buy the first round. Paul for all the footy banter, MattG for the poker nights and Ian for being such a cool opponent around the pool table. Oliver for his obscure sense of humour and Ethan and Bruce for their fine

tastes in ale.

Away from physics (yes, there is such a thing) there are a good number of people I wish to thank for keeping me sane during the slog of writing this thesis and always humouring my mantra of "I'll be finished in a month's time" for the past 18 months. I'd like to thank Phil, Edd, Guy and Rhod for all the beer, the parties, the festivals and the birthday on the wall — we should do something like that again...

Last, but certainly not least, I would like to thank my family for their support over these past four years and again for humouring me over the last 18 months. Without the free rent since May I'd be very poor indeed!

Declaration

I declare that the work in this thesis has not been previously submitted to any institution to fulfill the requirements of a higher degree.

The data used in this analysis were collected at the *BABAR* experiment by the *BABAR* collaboration. As a member of the collaboration I contributed to this effort by working data-taking shifts on the experiment and by maintaining and developing software for the Data Quality Group.

The data reconstruction and event selection described in Chapter 3 uses global code that is available to all *BABAR* members and some specific pre-selection code developed by the Charmless 3-body Working Group. The final selection as described in Section 3.5.3 was determined by the UK Charmless Group.

The analysis as described in Chapters 4 and 5 was performed by myself and Matthew Barrett using LAURA++ which was developed by Paul Harrison, John Back, Sian Morgan and Tom Latham with additions from Matthew Barrett and myself. The efficiency modelling and event migration studies in Sections 4.3 and 4.4 are the sole work of Matthew Barrett. The $B\overline{B}$ background study (Section 4.5.2), the likelihood scanning study (Sections 4.7 and 5.2) and the cross-checks as described in Section 5.4 are the sole work of the author.

Contents

Acknowledgements **iii**

Declaration **v**

1 Theory **1**

1.1 Introduction 1

1.2 *CP* Violation 2

1.2.1 *CPT* symmetry 3

1.2.2 The CKM matrix 4

1.2.3 Unitarity triangles 5

1.2.4 *CP* violation in decay 8

1.2.5 *CP* violation in mixing 10

1.2.6 *CP* violation in the interference between decays with and without mixing . . . 11

1.2.7 Current CKM constraints . . . 12

1.3 *B* meson physics . . . 12

1.3.1 Neutral meson mixing . . . 15

1.4 Dalitz Plot Theory . . . 16

1.4.1 Helicity angle . . . 19

1.4.2 Interference . . . 19

1.5 $B^{\pm} \to K^{\pm}K^{\mp}K^{\pm}$ Decay . . . 20

1.5.1 Motivation . . . 21

1.5.2 Previous experimental results . . . 23

2 The *BABAR* Experiment **26**

2.1 Introduction . . . 26

2.2 The Asymmetric *B* Factory — PEP-II . . . 28

2.2.1 The Interaction Point . . . 28

2.2.2 Backgrounds . . . 29

2.2.3 Performance . . . 31

2.3 The *BABAR* Detector . . . 32

2.4 The Silicon Vertex Tracker (SVT) 34
2.4.1 SVT Physics Requirements 34
2.4.2 SVT Design 35
2.4.3 SVT Performance 36
2.5 The Drift Chamber (DCH) 37
2.5.1 DCH Physics Requirements 37
2.5.2 DCH Design 38
2.5.3 DCH Performance 40
2.6 The Detector of Internally Reflected Cherenkov Radiation (DIRC) . . 42
2.6.1 DIRC Physics Requirements 42
2.6.2 DIRC Design 42
2.6.3 DIRC Performance 44
2.7 The ElectroMagnetic Calorimeter (EMC) 46
2.7.1 EMC Physics Requirements 46
2.7.2 EMC Design 46
2.7.3 EMC Performance 47
2.8 The Instrumented Flux Return (IFR) 48
2.8.1 IFR Physics Requirements 48

2.8.2 IFR Design 48

2.8.3 IFR Performance 50

2.9 The Trigger 50

2.9.1 The Level 1 Trigger 51

2.9.2 The Level 3 Trigger 51

2.10 The Data Acquisition System (DAQ) 52

3 Data Reconstruction and Event Selection 53

3.1 Introduction 53

3.2 Data Sample 54

3.2.1 B Counting 54

3.2.2 Monte Carlo Simulation 55

3.3 Event Reconstruction 56

3.3.1 Track Finding 57

3.3.2 Calorimeter Cluster Finding 58

3.3.3 Particle Identification (PID) 59

3.4 Discriminating Variables 65

3.4.1 The ΔE and $m_{\rm ES}$ variables 65

3.4.2 $\cos\theta_{Thr}$ . . . 66

3.4.3 Fisher Discriminant ($\mathcal{F}$) . . . 66

3.5 Event Selection . . . 68

3.5.1 Skimming . . . 70

3.5.2 NonCharm3BodyUser ntuple production . . . 71

3.5.3 Final Selection . . . 71

4 Analysis Method **76**

4.1 Introduction . . . 76

4.2 The Dalitz Plot Fit . . . 77

4.2.1 Fit Fractions . . . 79

4.2.2 *CP* Asymmetry . . . 80

4.3 Efficiency Modelling . . . 80

4.3.1 Self Cross-feed . . . 82

4.4 Event Migration Effects . . . 83

4.5 Background Estimation . . . 85

4.5.1 $q\overline{q}$ Background . . . 85

4.5.2 $B\overline{B}$ Background . . . 87

4.5.3 Determination of the Signal to Background ratio 92

4.6 The Signal Model 94

4.6.1 The $(KK)^0_0$ 97

4.6.2 Relativistic Breit-Wigner 98

4.6.3 Flatté 99

4.6.4 Choice of Nonresonant Model 100

4.7 Using a Likelihood Scan to Fix Fit Components 101

5 Analysis Results **103**

5.1 Introduction 103

5.2 Results of the Likelihood Scan 104

5.3 Dalitz Fit Results 105

5.3.1 Multiple Solutions 110

5.3.2 Precision of the fit 113

5.4 Cross-checks 115

5.4.1 Removal of components from the signal model 115

5.4.2 Inclusion of additional components in the signal model 115

5.4.3 Toy Monte Carlo fit-bias study 118

5.4.4 Full Monte Carlo tests 122

5.5 Systematic Uncertainty 126

5.5.1 Efficiency and Background Histograms 129

5.5.2 Background Fractions 129

5.5.3 Fit Bias 129

5.5.4 Model Dependency 131

5.6 Total Rate Measurement 132

5.7 Systematic Errors on the Total Rate Measurement 133

5.8 Upper Limits 136

6 Discussion and Conclusion **137**

List of Figures

1.1 The three down-type unitarity triangles. 6

1.2 The rescaled Unitarity Triangle 7

1.3 $B^{\pm} \to f_0(980)K^{\pm}$ decay diagrams. 9

1.4 2006 CKM-fitter results. 14

1.5 Box diagrams for B^0–$\overline{B}^0$ mixing. 16

1.6 An example Dalitz plot. 17

1.7 Dalitz plots showing different helicity patterns. 19

1.8 $B^{\pm} \to \phi(1020)K^{\pm}$ decay diagrams. 21

2.1 Overview of the SLAC linac and the PEP-II rings 28

2.2 Plan view of the PEP-II interaction region. 30

2.3 PEP-II integrated luminosity per month. 31

2.4 The *BABAR* Detector. 33

2.5 End view of the SVT 35

2.6 Side on view of the SVT 36

2.7 Side-on view of the DCH 38

2.8 Cell layout for the DCH layers 39

2.9 Tracking efficiency of the DCH. 40

2.10 dE/dx measurements in the DCH. 41

2.11 Elevation view of the DIRC. 43

2.12 Schematic diagram of a DIRC radiator bar and standoff box 44

2.13 DIRC pion/kaon separation as a function of track momentum. 45

2.14 A comparison of the invariant $\pi^{\pm}K^{\mp}$ mass spectrum with and without the DIRC. 45

2.15 Cross-sectional side-on view of the EMC 47

2.16 Diagram showing IFR barrel and endcap geometry 49

2.17 Cross-section of a RPC 49

2.18 A schematic of the data acquisition process at *BABAR*. 52

3.1 The ratio of multi-hadronic to Bhabha events versus the centre-of-mass energy. 55

3.2 Particle momentum distribution versus dE/dx for the SVT and DCH, and versus θ_C for the DIRC. 59

3.3 The distribution of Cherenkov angle against momenta for Monte Carlo kaon tracks 61

3.4 A plot of Δ_K with a cut at $r_\pi = 1$ 62

3.5 Kaon selection efficiency versus momentum for data and Monte Carlo using the tight kaon selector. 63

3.6 Particle misidentification selection efficiency versus momentum for data and Monte Carlo using the tight kaon selector. 64

3.7 The $|\cos\theta_{Thr}|$ distribution. 67

3.8 The distributions of the Fisher discriminant and its component parts. 69

3.9 ΔE-$m_{\rm ES}$ plane, showing Signal Strip, Signal Box and the Sideband. . 73

3.10 Signal significance as a function of Fisher selection value. 74

4.1 The Dalitz Plot. 78

4.2 Efficiency distribution across the Dalitz plot. 81

4.3 Efficiency distribution, corrected for low statistics bins [57]. 83

4.4 Dalitz distribution of self cross-feed events. 84

4.5 Migration of events within the Dalitz plot. 85

4.6 Dalitz plot distributions for continuum ($q\overline{q}$) background events. . . . 86

4.7 Square Dalitz plot distributions for $q\overline{q}$ background events. 87

4.8 Dalitz plot distributions for $B\overline{B}$ background events. 88

4.9 Square Dalitz plot distributions for $B\overline{B}$ background events. 92

4.10 The $m_{\rm ES}$ distribution of $B^{\pm} \to K^{\pm}K^{\mp}K^{\pm}$ nonresonant MC events. . . 93

4.11 The $m_{\rm ES}$ distribution for off-resonance data, fitted with an Argus function. 93

4.12 The $m_{\rm ES}$ distribution of the $B\overline{B}$ background. 94

4.13 Comparison mass projection plots for B^+ and B^-. 95

4.14 Mass pair projection plots for complete dataset. 96

4.15 Helicity plot of the 1.5 GeV/c^2 region 98

5.1 Likelihood scan of nonresonant α. 105

5.2 Likelihood scan of scalar mass. 106

5.3 Likelihood scan of scalar width. 106

5.4 Mass pair projection plots for the B^+ and B^- fits. 107

5.5 The goodness of the fit across the Dalitz plot. 114

5.6 B^+ pull plots. 123

5.7 B^- pull plots. 124

5.8 The $m_{\rm ES}$ fits to data events. 132

List of Tables

1.1 Current CKM fitter results. 13

1.2 Details of the B mesons. 15

1.3 Theoretical predictions for modes that contribute to $B^{\pm} \to K^{\pm}K^{\mp}K^{\pm}$. 22

1.4 Previous experimental results for modes that contribute to $B^{\pm} \to K^{\pm}K^{\mp}K^{\pm}$. 24

2.1 Parameters of the PEP-II machine. 29

3.1 Kaon selection requirements. 63

3.2 Summary of average selection efficiencies. 75

4.1 $B^{+}B^{-}$ background mode details. 89

4.2 $B^{+}B^{-}$ background mode details continued. 90

4.3 $B^{0}\overline{B}^{0}$ background mode details. 91

5.1 Dalitz plot fit results. 108

5.2 Asymmetry results. 109

5.3 B^+ Multiple solutions 111

5.4 B^- Multiple solutions 112

5.5 B^+ Omission test results. 116

5.6 B^- Omission test results. 117

5.7 B^+ Addition test results. 119

5.8 B^- Addition test results. 120

5.9 Magnitude and Phase pull results. 121

5.10 B^+ Fit Fraction distribution means and widths from toy MC samples 125

5.11 B^- Fit Fraction distribution means and widths from toy MC samples 125

5.12 Phase distribution means from toy MC samples using the nominal fit results. 125

5.13 Magnitude and phase results of first reweighted MC experiment . . . 127

5.14 Magnitude and phase results of second reweighted MC experiment . . 127

5.15 Magnitude and phase results of second reweighted MC experiment . . 127

5.16 Magnitude and phase results of third reweighted MC experiment . . . 128

5.17 Magnitude and phase results of third reweighted MC experiment . . . 128

5.18 Magnitude and phase results of third reweighted MC experiment . . . 128

5.19 Magnitude and phase results of third reweighted MC experiment . . . 128

5.20 Systematic uncertainties from the Dalitz fit. 130

5.21 Results for the fits to $m_{\rm ES}$ in the Signal Strip. 133

5.22 Selection requirement efficiency corrections. 135

5.23 90% confidence level upper limits on fit fractions. 136

6.1 Dalitz plot fit results. 138

6.2 Summary of branching fractions, 90% confidence upper limits and *CP* asymmetries 139

1

Theory

1.1 Introduction

The *BABAR* experiment was first conceived as a high luminosity tool to study *CP* violation in the B meson system, where "*CP*" is the product of the **C**harge conjugation and **P**arity symmetries.

In nature where we have a symmetry there is, in general, also a conservation law. For example the symmetry of the laws of nature under the group of spatial transformation (i.e. the laws of nature are the same everywhere), gives rise to the law

of conservation of momentum. Similarly it was assumed that left-right symmetry gave rise to a conservation of parity (P), particle-antiparticle symmetry gave rise to charge conservation (C), and event order symmetry led to time-reversal invariance (T).

This chapter discusses the theory concerning this analysis and gives an overview of CP violation in general.

1.2 CP Violation

Both C and P symmetries are conserved in classical physics, and it was assumed they applied universally until 1956, when Lee and Yang proposed that parity is not a symmetry of weak interactions [1], [2]. They also proposed experimental ideas to test this hypothesis. The first to be tested, by Wu *et al.* in 1957, involved measurements of the β decay of cobalt-60 [3].

Their experiment exploited the fact that β particles are mainly emitted from the poles of cobalt nuclei. The nuclei were placed in a strong magnetic field so that their spins aligned in the same direction. In a mirror image the north and south poles of the nuclei would be reversed since they will be spinning in the opposite direction to their real counterparts, and so parity conservation demands that beta particles be equally emitted from the two poles. However an anisotropy in the emitted β particles was observed — parity conservation was violated. This meant that the laws of physics are dependent on the 'handedness' of the experiment, giving rise to the phrase "God is weakly left-handed".

After the result was announced, still in 1957, Ioffe, Okun and Rudik showed that P violation meant C invariance must also be violated in weak decays [4]. It seemed however that a combined CP symmetry was conserved, but in 1964 Christenson,

Cronin, Fitch and Turlay found experimental evidence for *CP* violation [5]. At the time K-short (K_S^0) and K-long (K_L^0) were thought to be *CP* eigenstates,

$$\widehat{CP}|K_S^0\rangle = +1|K_S^0\rangle, \qquad \widehat{CP}|K_L^0\rangle = -1|K_L^0\rangle. \tag{1.1}$$

If *CP* is conserved then K_L^0 decays to a *CP* +1 state are forbidden, and K_S^0 decays to *CP* −1 states are likewise forbidden. However Christenson *et al* observed the decay of K_L^0 to the *CP* +1 state of $\pi^+\pi^-$, and so found the first evidence for the violation of the *CP* symmetry.

1.2.1 *CPT* symmetry

CPT invariance is implicit in the structure of the quantum field theories that are used to describe nature, and is thus far backed up by all experimental evidence. The conservation of *CPT* while *CP* is violated implies that T (time reversal symmetry) also must be violated.

Direct experimental evidence for T violation was first seen by the CPLEAR collaboration in 1998 [6]. They studied the decays $p\bar{p} \to K^+\pi^-K^0$ and $p\bar{p} \to K^-\pi^+\bar{K}^0$, where the neutral kaon decayed via ${K^0}_{t=0} \to e^-\pi^+\bar{\nu}_{t=\tau}$ or $\bar{K}^0_{t=0} \to e^+\pi^-\nu_{t=\tau}$. The type of neutral kaon present in the decay was determined from the accompanying $K^\pm$ or $e^\pm$, and measured at $t = 0$ and $t = \tau$. The asymmetry of these neutral kaon decays is equal to:

$$\frac{P(\bar{K}^0 \to K^0) - P(K^0 \to \bar{K}^0)}{P(\bar{K}^0 \to K^0) + P(K^0 \to \bar{K}^0),} \tag{1.2}$$

where the probability P that a K^0 ($t = 0$) is observed as a $\bar{K}^0$ at a time τ should be equal to the probability that $\bar{K}^0$ ($t = 0$) is observed as a K^0 at a time τ. A difference between these two probabilities was found, and thus proof of T violation.

1.2.2 The CKM matrix

The existence of quark mixing and quark decay lead to the introduction of the Cabbibo matrix as a method to describe the phenomenon of one quark changing into another quark via the weak force, It was introduced to relate the weak quark eigenstates to their mass eigenstates,

$$\begin{pmatrix} d' \\ s' \end{pmatrix} = V_C \begin{pmatrix} d \\ s \end{pmatrix}, \tag{1.3}$$

where d' and s' are the weak eigenstates and d and s are mass eigenstates. V_C is the Cabbibo matrix,

$$V_C = \begin{pmatrix} cos\theta_C & sin\theta_C \\ -sin\theta_C & cos\theta_C \end{pmatrix}, \tag{1.4}$$

where θ_C is the Cabbibo mixing angle ($\theta_C \approx 13°$). As θ_C is real there is no possibility of *CP* violation in this model.

After the discovery of *CP* violation it was obvious that the model needed to be updated. Kobayashi and Maskawa found that by including an additional generation of quarks the matrix then had three mixing angles and a complex phase. It is interesting to note therefore that the discovery of *CP* violation led directly to the prediction of the existence of top and bottom quarks by Kobayashi and Maskawa [7]. The new matrix was named the Cabibbo-Kobayashi-Maskawa (CKM) matrix and is written:

$$V_{CKM} = \begin{pmatrix} V_{ud} & V_{us} & V_{ub} \\ V_{cd} & V_{cs} & V_{cb} \\ V_{td} & V_{ts} & V_{tb} \end{pmatrix} \tag{1.5}$$

The standard parameterisation and the one adopted by the Particle Data Group is:

$$V_{CKM} = \begin{pmatrix} c_{12}c_{13} & s_{12}c_{13} & s_{13}e^{-i\delta} \\ -s_{12}c_{23} - c_{12}s_{23}s_{13}e^{i\delta} & c_{12}c_{23} - s_{12}s_{23}s_{13}e^{i\delta} & s_{23}c_{13} \\ s_{12}s_{23} - c_{12}c_{23}s_{13}e^{i\delta} & -c_{12}s_{23} - s_{12}c_{23}s_{13}e^{i\delta} & c_{23}c_{13} \end{pmatrix} \tag{1.6}$$

where $c_{ij} = \cos\theta_{ij}$, $s_{ij} = \sin\theta_{ij}$ and δ represents the complex phase. θ_{ij} is the mixing angle between the ith and jth generations. The Wolfenstein parameterisation [8] is

also commonly used. It expresses the matrix elements in expanding powers of λ:

$$V_{CKM} \approx \begin{pmatrix} 1-\lambda^2/2 & \lambda & A\lambda^3(\rho - i\eta) \\ -\lambda & 1-\lambda^2/2 & A\lambda^2 \\ A\lambda^3(1-\rho-i\eta) & -A\lambda^2 & 1 \end{pmatrix} + \mathcal{O}(\lambda^4) \tag{1.7}$$

where $\lambda = V_{us}(\approx 0.22)$ and $A(\approx 0.81)$ are well measured experimentally [9], and ρ and η correspond to the phase δ from Equation 1.6.

1.2.3 Unitarity triangles

The CKM matrix now describes quark mixing in the standard model. It is a unitary matrix ($VV^\dagger = 1$) and this implies two types of relation:

$$\sum_j |V_{ij}|^2 = 1, \tag{1.8}$$

where $i = u$, c or t, and $j = d$, s and b. This relation is called "weak universality" and implies that the sum of all the couplings of any up-type quark to the down-type quarks is the same across the generations. The second type of relation is:

$$\sum_i V_{ij} V_{ik}^* = 0, \quad (j \neq k) \tag{1.9}$$

for any fixed j and k and where i, j and k can this time represent any flavour of quark with the one proviso that i must be of a different up-down type to j and k. There are six such relations, each of which equates to the mixing of one flavour of quark to another, and so relate to mixing of the neutral mesons (see Section 1.3.1). Two of the six relations include the top quark, which doesn't form bound states, leaving only four relations that relate to actual particles:

$$V_{du}V_{dc}^* + V_{su}V_{sc}^* + V_{bu}V_{bc}^* = 0. \tag{1.10}$$

$$V_{ud}V_{us}^* + V_{cd}V_{cs}^* + V_{td}V_{ts}^* = 0. \tag{1.11}$$

$$V_{ud}V_{ub}^* + V_{cd}V_{cb}^* + V_{td}V_{tb}^* = 0. \tag{1.12}$$

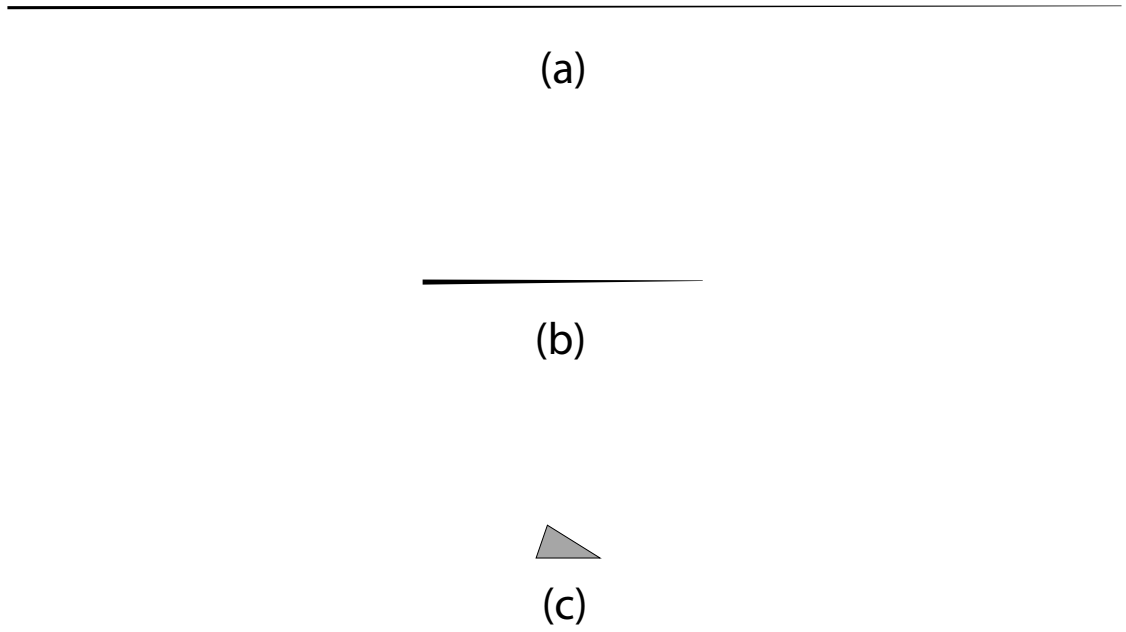

Figure 1.1: *The three down-type unitarity triangles drawn to a common scale using experimental results for the various V_{ij} [10]. (a) shows $V_{id}V_{is}^* = 0$ (K^0 mixing), (b) shows $V_{is}V_{ib}^* = 0$ (B_s^0 mixing) and (c) shows $V_{id}V_{ib}^* = 0$ (B^0 mixing), where $i = u$, c or t.*

$$V_{us}V_{ub}^* + V_{cs}V_{cb}^* + V_{ts}V_{tb}^* = 0. \tag{1.13}$$

Equation 1.10 describes D^0 mixing, 1.11 K^0 mixing, 1.12 B^0 mixing and 1.13 B_s^0 mixing. As the sum of the three complex quantities must cancel, each relation can be geometrically represented by a triangle in the complex plane. These are known as unitarity triangles.

Of the four remaining relations only one, Equation 1.12, has sides of similar magnitude. Figure 1.1 shows the three down-type unitarity triangles drawn to a common scale. The almost flat K^0 and B_s^0 triangles indicate that *CP* violation is small in the leading K^0 and B_s^0 decays. The short sides may exhibit significant *CP* violation, but the associated decays are very rare. The B^0 triangle, commonly referred to as *the* Unitarity Triangle, is rather more open and predicts large *CP* asymmetries in

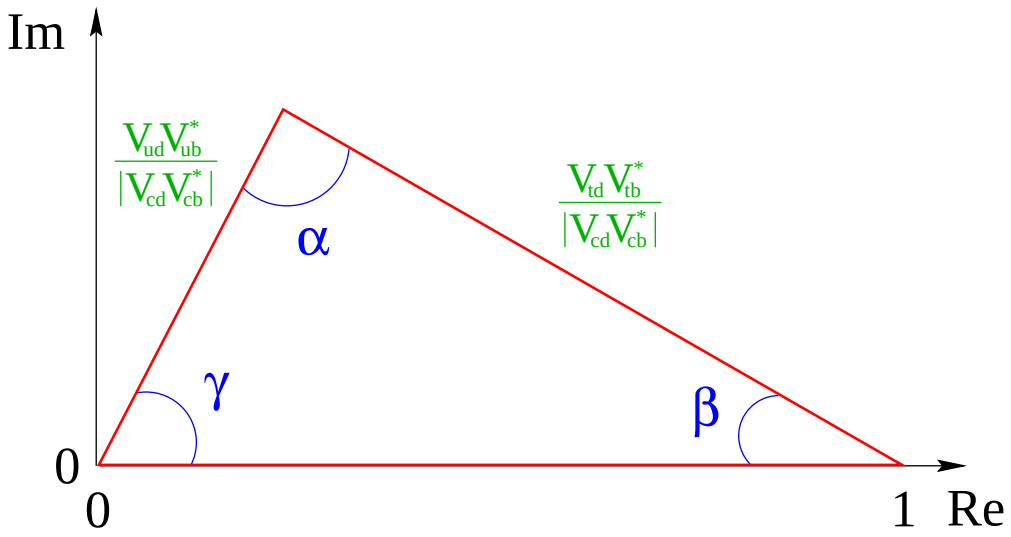

Figure 1.2: *The rescaled Unitarity Triangle*

B^0 decays. This means that one can (relatively) easily measure all three angles and the lengths of all three sides and if they don't sum to give a closed triangle it would be a sign of new physics.

The Unitarity Triangle can be simplified by rescaling; a phase convention is chosen making $(V_{cd}V_{cb}^*)$ real, then each side is divided by $|V_{cd}V_{cb}^*|$. This gives a real side of unit length, and puts two corners of the triangle at (0,0) and (1,0), thus leaving only one vertex to find. *BABAR* labels the angles of the Unitarity Triangle as α, β and γ, where each is given by

$$\alpha \equiv \arg\left[-\frac{V_{td}V_{tb}^*}{V_{ud}V_{ub}^*}\right], \quad \beta \equiv \arg\left[-\frac{V_{cd}V_{cb}^*}{V_{td}V_{tb}^*}\right], \quad \gamma \equiv \arg\left[-\frac{V_{ud}V_{ub}^*}{V_{cd}V_{cb}^*}\right]. \tag{1.14}$$

The angles are physical quantities and represent the amount of *CP* violation in the B meson system.

There are three types of *CP* violation,

- ◇ Violation in decay.

◇ Violation in mixing.

◇ Violation in the interference between decays with and without mixing.

1.2.4 *CP* violation in decay

CP violation in decay is often called *direct CP* violation. It occurs when the decay rate of one particle to another does not match that of its *CP* conjugate process.

If one considers the decay $B \to f$ with amplitude A_f and its *CP* conjugate $\overline{B} \to \bar{f}$ with amplitude $\bar{A}_{\bar{f}}$, then there is direct *CP* violation if

$$\left|\frac{A_f}{\bar{A}_{\bar{f}}}\right| \neq 1, \tag{1.15}$$

where

$$A_f = \langle B|H|f\rangle = \sum_j A_j e^{i(\delta_j+\phi_j)}, \quad \bar{A}_{\bar{f}} = \langle \overline{B}|H|\bar{f}\rangle = \sum_j A_j e^{i(\delta_j-\phi_j)}, \tag{1.16}$$

and A_j, δ_j and ϕ_j are the amplitude, strong phase and weak phase of contributing processes. H is the Hamiltonian. *CP* violation can occur when there are at least two processes of a similar magnitude, but with different strong and weak phases. The *CP* asymmetry of a decay is defined:

$$A_{CP} \equiv \frac{\Gamma(\bar{B} \to \bar{f}) - \Gamma(B \to f)}{\Gamma(\bar{B} \to \bar{f}) + \Gamma(B \to f)}, \tag{1.17}$$

where Γ is the decay rate.

As direct *CP* violation comes from interference between various processes contributing to a decay it can occur in the decays of $B^{\pm}$. The first discovery of direct *CP* violation in B decays came in the $B^0 \to K^+\pi^-$ channel [11]. Generally neutral decays are not "self-tagging" ($B^0 \to K^+\pi^-$ is due to the kaon), but charged decays have the advantage of always being self-tagging. That is, one can tell the flavour of

the B meson from the charge of the decay products. With neutral decays one also has to examine the spectator B to hopefully be able to identify the flavours, thus losing vital statistics.

Charmless decays of B-mesons, where $b \to u\bar{u}s$ or $b \to s\bar{s}s$, are expected to be good candidates for observing direct CP violation as most have similar magnitude contributions from both weak tree-level processes and loop diagrams. Figure 1.3 shows Feyman diagrams for processes contributing to the charmless decay $B^{\pm} \to f_0(980)K^{\pm}$.

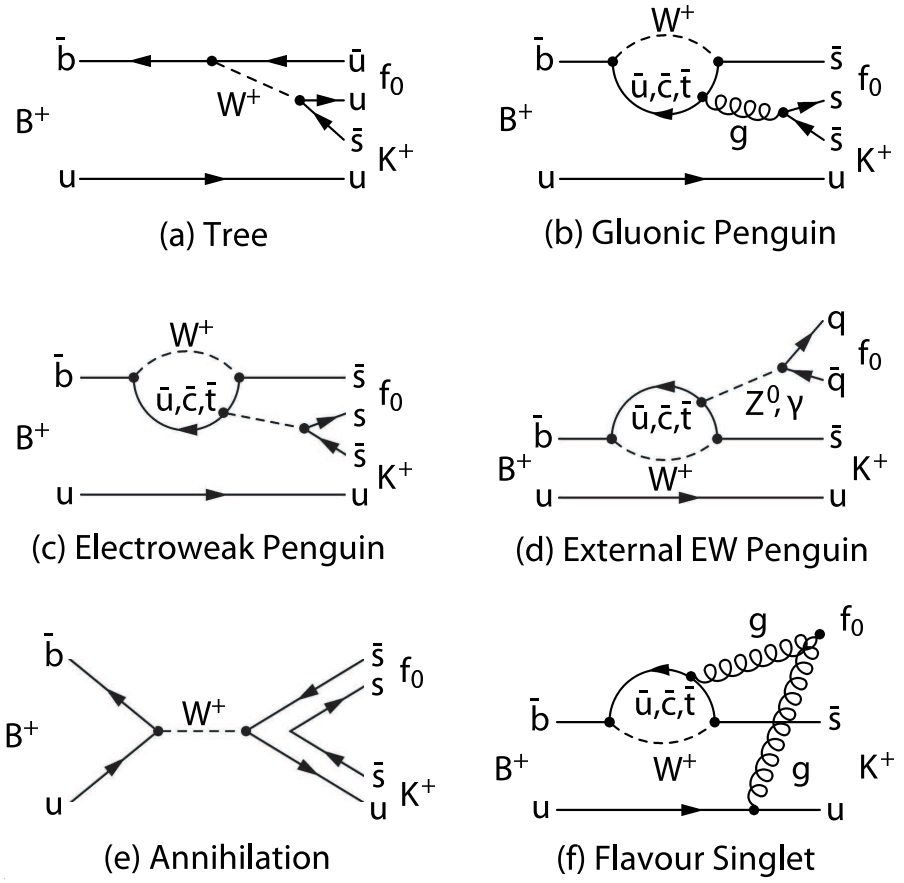

Figure 1.3: *$B^{\pm} \to f_0(980)K^{\pm}$ decay diagrams.*

1.2.5 *CP* violation in mixing

This form of *CP* violation is said to be *indirect* since the violation occurs in the mixing, rather than the actual decay. When *CP* violation was discovered in kaon decays it was indirect violation that was being observed.

CP violation in B meson mixing occurs when:

$$\left|\frac{p}{q}\right| \neq 1, \tag{1.18}$$

where p and q are complex coefficients and obey the normalisation condition $|p|^2 + |q|^2 = 1$. They are coefficients from B mixing, see Section 1.3.1. The ratio p/q is given by:

$$\frac{p}{q} = -\frac{2(M_{12} - \frac{i}{2}\Gamma_{12})}{\Delta m_B - \frac{i}{2}\Delta\Gamma_B}, \tag{1.19}$$

where M_{12} and Γ_{12} come from the matrices in equation 1.32 and Δm_B and $\Delta\Gamma_B$ are the differences in mass and lifetime between the mass eigenstates and are defined:

$$\Delta m_B \equiv M_H - M_L \tag{1.20}$$

$$\Delta\Gamma_B \equiv \Gamma_H - \Gamma_L. \tag{1.21}$$

Experimental measurements show that $\Delta\Gamma_B \ll \Delta m_B$ and therefore also $\Gamma_{12} \ll M_{12}$. Equations 1.20 and 1.21 then reduce to:

$$\Delta m_B \approx 2|M_{12}| \tag{1.22}$$

$$\Delta\Gamma_B \approx 2\Re(M_{12}\Gamma_{12}^*) \;\; / \;\; |M_{12}|. \tag{1.23}$$

Equation 1.19 then simplifies to:

$$\frac{p}{q} \approx -\frac{M_{12}}{|M_{12}|} \tag{1.24}$$

To first order $|p/q| = 1$, which means that there is very little *CP* violation directly from the mixing of B mesons. Second order corrections are expected to be small ($\mathcal{O}(10^{-2})$) [10].

1.2.6 *CP* violation in the interference between decays with and without mixing

This type of *CP* violation can occur with both direct and indirect *CP* violation, or it can occur separately. It occurs in decays to a *CP* eigenstate, i.e. a final state that is accessible to both B^0 and $\overline{B}^0$, for example $J/\psi K^0_S$. Lets call the final state f_{CP}. *CP* violation is observed if the quantity

$$|\lambda| \equiv \left| \frac{q}{p} \frac{\bar{A}_{f_{CP}}}{A_{f_{CP}}} \right| \neq 1, \tag{1.25}$$

where p and q again come from B mixing and $A_{f_{CP}}$ and $\bar{A}_{f_{CP}}$ are the decay amplitudes of the mode being studied. The time-dependent *CP* asymmetry is given by:

$$A_{CP}(t) = \frac{\Gamma(B \to f)(t) - \Gamma(\overline{B} \to f)(t)}{\Gamma(B \to f)(t) + \Gamma(\overline{B} \to f)(t)} \tag{1.26}$$

$$= \frac{(1 - |\lambda|^2)\cos(\Delta m_B t) - 2\Im(\lambda)\sin(\Delta m_B t)}{1 + |\lambda|^2} \tag{1.27}$$

where Δm_B is again the mass difference between the B^0 mass eigenstates.

The decay $B^0 \to J/\psi K^0_S$ proceeds mainly via a standard tree process and as such the *CP* violation in decay is minimal. Therefore one can make the approximation $|\lambda| = 1$, thus simplifying Equation 1.27 to:

$$A_{CP}(t) = -\Im(\lambda_{J/\psi K^0_S})\sin(\Delta m_B t), \tag{1.28}$$

where

$$\Im(\lambda_{J/\psi K^0_S}) = \sin(2\beta). \tag{1.29}$$

Therefore the angle β can be readily determined from the asymmetry of this and similar decays.

1.2.7 Current CKM constraints

The *CKM fitter* group [12] collate the results from the CKM sector of particle physics. They use the Wolfenstein parameterisation (Equation 1.7) with λ and A, but after rescaling the Unitarity Triangle the apex moves from (ρ, η) to $(\bar{\rho}, \bar{\eta})$. The relation between the two is given by [13]:

$$\rho + i\eta = \frac{\sqrt{1 - A^2\lambda^4}(\bar{\rho} + i\bar{\eta})}{\sqrt{1-\lambda^2}[1 - A^2\lambda^4(\bar{\rho} + i\bar{\eta})]}. \tag{1.30}$$

As mentioned earlier λ and A are well measured experimentally. λ, which is V_{us}, has been measured to be approximately 0.23 from kaon semi-leptonic decays. A is V_{cb}/λ^2 and V_{cb} is measured in semi-leptonic B-meson decays to be approximately 41×10^{-3}. These together with current best measurements of the Unitarity Triangle parameters are used as inputs for a global fit in *CKM fitter*. The latest fit results are shown in Table 1.1 and Figure 1.4.

1.3 B meson physics

A B meson is so named because the heaviest quark it contains is a b (or $\overline{b}$) quark. There are essentially four types of B meson, the B_d^0, $B_u^{\pm}$, B_s^0 and $B_c^{\pm}$. The first two of which are commonly referred to simply as B^0 and $B^{\pm}$, and will be for the rest of this thesis. The quark content and masses of the B mesons can be seen in Table 1.2.

The B^0 meson offers a useful environment for studying CP violation as the most open unitarity triangle corresponds to the transition of a b quark to a d quark and is the mechanism for B^0 mixing (see Section 1.2).

To create B^0 mesons the *BABAR* experiment collides electrons and positrons at a centre-of-mass energy of $10.58\,\mathrm{GeV}/c^2$, which corresponds to the mass of the bound $b\overline{b}$

Observable	central $\pm 2\sigma$
λ	$0.2272^{+0.0020}_{-0.0020}$
A	$0.809^{+0.029}_{-0.028}$
$\bar{\rho}$	$0.197^{+0.050}_{-0.087}$
$\bar{\eta}$	$0.339^{+0.047}_{-0.037}$
$\|V_{ud}\|$	$0.97383^{+0.00047}_{-0.00047}$
$\|V_{us}\|$	$0.2272^{+0.0020}_{-0.0020}$
$\|V_{ub}\|$	$(3.82^{+0.31}_{-0.29}) \times 10^{-3}$
$\|V_{cd}\|$	$0.22712^{+0.00199}_{-0.00205}$
$\|V_{cs}\|$	$0.97297^{+0.00048}_{-0.00047}$
$\|V_{cb}\|$	$(41.79^{+1.26}_{-1.27}) \times 10^{-3}$
$\|V_{td}\|$	$(8.28^{+0.92}_{-0.57}) \times 10^{-3}$
$\|V_{ts}\|$	$(41.13^{+1.25}_{-1.24}) \times 10^{-3}$
$\|V_{tb}\|$	$0.999119^{+0.000052}_{-0.000054}$
α (deg)	$97.3^{+8.7}_{-14.0}$
β (deg)	$22.86^{+2.03}_{-1.97}$
γ (deg)	$59.8^{+13.9}_{-7.9}$

Table 1.1: *Current best fit results using CKM fitter [12].*

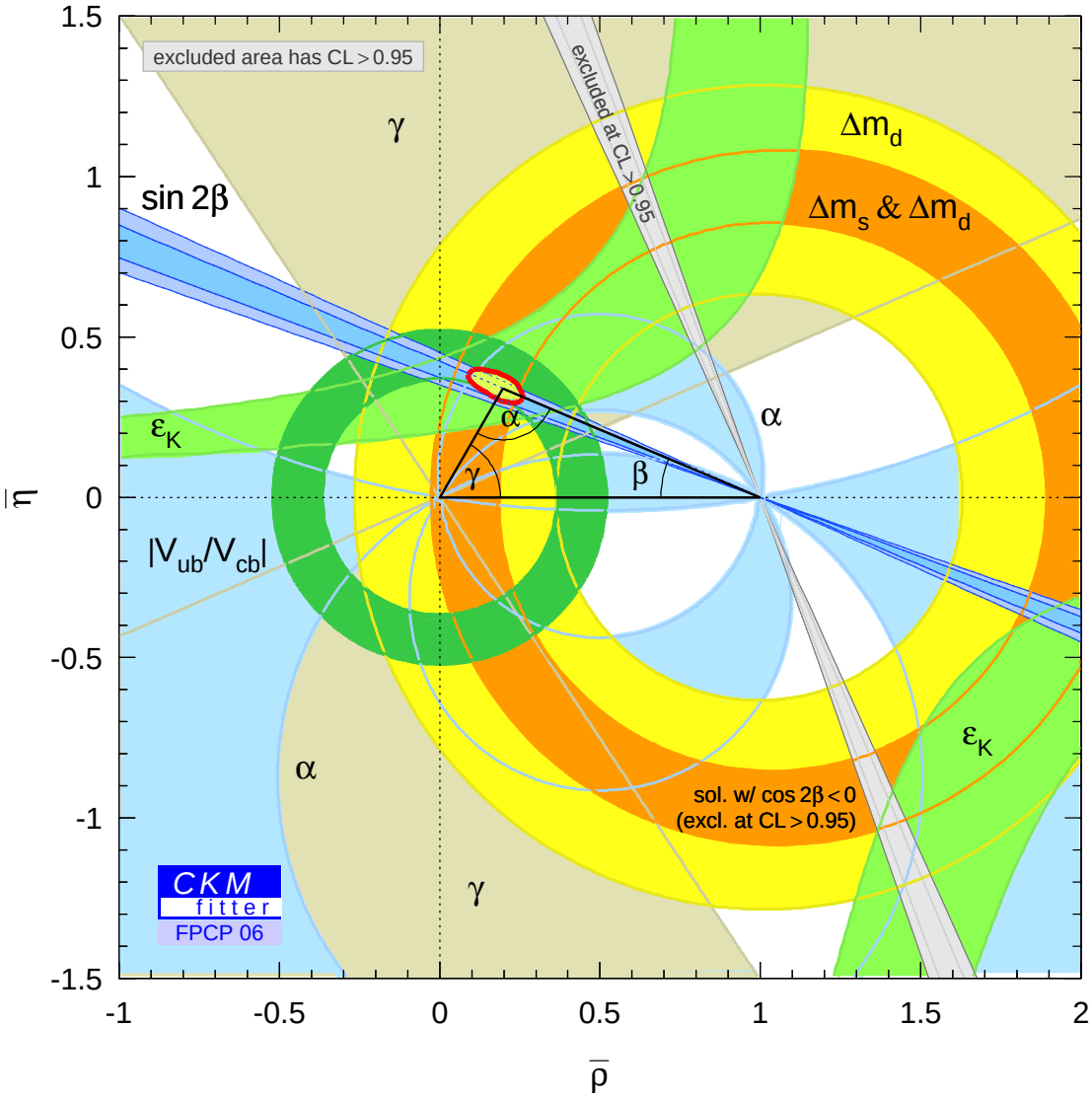

Figure 1.4: *Constraints in the $\bar{\rho}$-$\bar{\eta}$ plane from the latest CKM fitter publication [12].*

Particle	Quark content	Charge	Mass
B_d^0	$\overline{b}d$	0	$(5279.4 \pm 0.5)\,\mathrm{MeV}/c^2$
$\bar{B}_d^0$	$b\overline{d}$	0	$(5279.4 \pm 0.5)\,\mathrm{MeV}/c^2$
B_u^+	$\overline{b}u$	+1	$(5279.0 \pm 0.5)\,\mathrm{MeV}/c^2$
B_u^-	$b\overline{u}$	-1	$(5279.0 \pm 0.5)\,\mathrm{MeV}/c^2$
B_s^0	$\overline{b}s$	0	$(5369.6 \pm 2.4)\,\mathrm{MeV}/c^2$
$\bar{B}_s^0$	$b\overline{s}$	0	$(5369.6 \pm 2.4)\,\mathrm{MeV}/c^2$
B_c^+	$\overline{b}c$	+1	$(6.4 \pm 0.39 \pm 0.13)\,\mathrm{GeV}/c^2$
B_c^-	$b\overline{c}$	-1	$(6.4 \pm 0.39 \pm 0.13)\,\mathrm{GeV}/c^2$

Table 1.2: *Details of the basic B mesons. There also exist various excited state B^* mesons that are not covered here.*

state $\Upsilon(4S)$. This is the lightest meson that can decay to a $B\overline{B}$ pair. Approximately 21% of all hadronic events at *BABAR* produce a $\Upsilon(4S)$, and greater than 96% of $\Upsilon(4S)$ decays produce a $B\overline{B}$ pair. These decays are constituted almost equally of $B^0\overline{B}^0$ and B^+B^-. The heavier B_s^0 and $B_c^\pm$ are not produced and therefore not studied at *BABAR*.

Although a large proportion of the physics goals of *BABAR* were to do with studying *CP* violation in B^0 mixing, *CP* violation also occurs in $B^\pm$ decays.

1.3.1 Neutral meson mixing

When a meson 'mixes' it changes into the corresponding antimeson. This process must conserve charge, and so can only occur in the neutral mesons; K^0 ($\overline{s}d$), D^0 ($c\overline{u}$), B^0 and B_s^0. Mixing does not occur in all neutral mesons, for example the π^0 (a $u\overline{u}/d\overline{d}$ mixture) or the $\Upsilon(4S)$, as they are their own antiparticles.

B^0 and $\overline{B}^0$ are flavour eigenstates and have a definite quark content. Figure 1.5 shows box diagrams for B^0 mixing. The mass eigenstates for B^0 are labelled B_L ('light') and B_H ('heavy') due to the relatively large mass difference (a few MeV/c^2). However they share almost identical lifetimes (conversely K^0 mass eigenstates have very different lifetimes, but almost identical masses). B_L and B_H can be written as a linear combination of the flavour eigenstates:

$$|B_L\rangle \;=\; p|B^0\rangle \;+\; q|\bar{B}^0\rangle, \qquad |B_H\rangle \;=\; p|B^0\rangle \;-\; q|\bar{B}^0\rangle, \tag{1.31}$$

where p and q are complex and obey the normalisation condition $|p|^2 + |q|^2 = 1$. This combination is governed by the Schrödinger equation

$$i\frac{d}{dt}\begin{pmatrix} p \\ q \end{pmatrix} = H\begin{pmatrix} p \\ q \end{pmatrix} \equiv \begin{pmatrix} H_{11} & H_{12} \\ H_{21} & H_{22} \end{pmatrix}\begin{pmatrix} p \\ q \end{pmatrix} \equiv \left(M - \frac{i}{2}\Gamma\right)\begin{pmatrix} p \\ q \end{pmatrix}, \tag{1.32}$$

where M and Γ are 2×2 Hermitian matrices originating from mixing and decay respectively. The ratio of p/q is used for measuring CP violation, as detailed earlier in Section 1.2.5.

1.4 Dalitz Plot Theory

The decays of heavy mesons to three-body final states are generally dominated by intermediate resonances, which can be described as quasi-two-body decays, containing a resonance and meson. For example the decay $B^\pm \to K^\pm K^\mp K^\pm$ can proceed via $B^\pm \to \phi(1020)K^\pm$, where $\phi(1020) \to K^+K^-$.

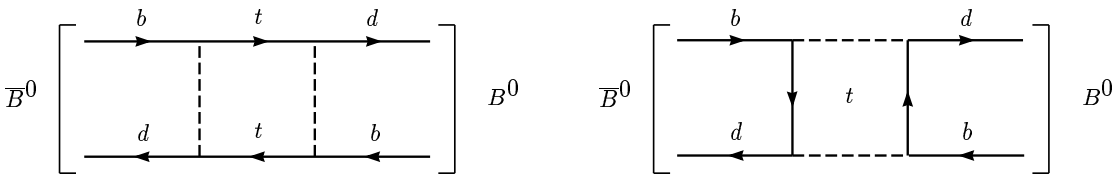

Figure 1.5: *Box diagrams for B^0–$\overline{B}^0$ mixing [14].*

Using the Dalitz plot technique [15] allows one to study the properties of the various resonances while also taking into account any interference between them.

Consider the decay of a B-meson at rest to three daughter particles. The B has mass m_B and the daughters have masses m_1, m_2, m_3, momenta p_1, p_2, p_3, and energies E_1, E_2 and E_3. The Lorentz invariant mass combinations are then m^2_{12}, m^2_{13} and m^2_{23} and plotting two against each other gives a Dalitz plot. Figure 1.6 shows an example plot.

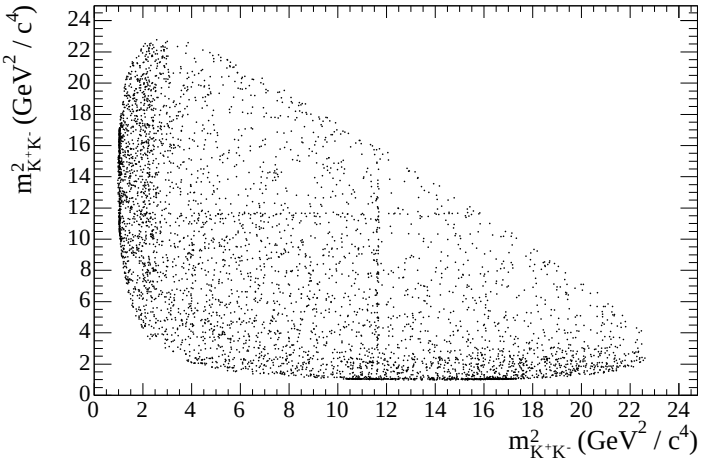

Figure 1.6: *A example Dalitz plot for $B^+ \to K^+K^-K^+$. The events were generated using a Toy Monte Carlo method. It is convenient to use the opposite-charge pairs as the axes because there are no resonances that decay to the same-charge pair $m^2_{K^+K^+}$.*

The Lorentz invariant phase space for such a three body decay can be written

$$dN \propto \delta^4\left(p_B - \sum_{i=1}^{3} p_i\right)\prod_{i=1}^{3}\frac{d^3p_i}{E_i} = \delta\left(m_B - \sum_{i=1}^{3} E_i\right)\frac{p_1^2 dp_1 p_2^2 dp_2 d\Omega_1 d\Omega_2}{E_1E_2E_3}. \quad (1.33)$$

As the B meson is spin-0 the decay is isotropic, and so fixing the direction of $\vec{p}_1$ gives $\int d\Omega_1 = 4\pi$. Thus $\int d\Omega_2 = 2\pi d\cos\theta_{12}$, where θ_{12} is the angle between $\vec{p}_1$ and $\vec{p}_2$. Then using:

$$E_3 = \sqrt{p_1^2 + p_2^2 + 2p_1p_2\cos\theta_{12} + m_3^2} \quad (1.34)$$

Equation 1.33 becomes:

$$dN \propto \delta\left(m_B - E_1 - E_2 - \sqrt{p_1^2 + p_2^2 + 2p_1p_2\cos\theta_{12} + m_3^2}\right) d\cos\theta_{12}\frac{p_1^2 dp_1 p_2^2 dp_2}{E_1E_2E_3}, \tag{1.35}$$

which reduces to:

$$dN \propto \frac{E_3}{p_1p_2}\frac{p_1^2 dp_1 p_2^2 dp_2}{E_1E_2E_3} \tag{1.36}$$

$$\propto \frac{p_1 dp_1}{E_1}\frac{p_2 dp_2}{E_2}, \tag{1.37}$$

and since $E_i dE_i = p_i dp_i$

$$dN \propto dE_1 dE_2 \tag{1.38}$$

$$\propto dm_{12}^2 dm_{23}^2, \tag{1.39}$$

and thus the decay rate for a three-body decay is proportional to

$$|\mathcal{M}|^2 dm_{12}^2 dm_{23}^2, \tag{1.40}$$

where $\mathcal{M}$ is the matrix element for the decay. The distribution of points across the Dalitz plot thus depends upon $\mathcal{M}$. If $\mathcal{M}$ is constant across the plot then one would see a uniform density, which is consistent with nonresonant decay. However if resonances are present then $\mathcal{M}$ would have a kinematic dependence and the resonances will form bands on the Dalitz plot, as can be seen in Figure 1.6.

The boundary of the Dalitz plot is described by

$$m_{12}^2 + m_{13}^2 + m_{23}^2 = m_B^2 + m_1^2 + m_2^2 + m_3^2. \tag{1.41}$$

The extreme edges of the boundary for each axis describe a situation where the momenta of the two particles are parallel or anti-parallel, i.e.

$$\left(m_{ij}^2\right)_{\max} = (E_i + E_j)^2 - (p_i - p_j)^2 \tag{1.42}$$

$$\left(m_{ij}^2\right)_{\min} = (E_i + E_j)^2 - (p_i + p_j)^2 . \tag{1.43}$$

1.4.1 Helicity angle

The helicity angle, $\theta_{H_{ij}}$, is defined to be the angle between particles j and k in the ij rest frame. Its cosine is given by

$$\cos\theta_{H_{ij}} = \frac{(m^2_{jk})_{\max} + (m^2_{jk})_{\min} - 2m^2_{jk}}{(m^2_{jk})_{\max} - (m^2_{jk})_{\min}}. \tag{1.44}$$

It is a useful quantity as the spin of a resonance can be identified by its distribution in $\cos\theta_H$. A scalar (spin 0) particle has a uniform distribution in $\cos\theta_H$, whereas the distribution for a vector (spin 1) particle is $\cos^2\theta_H$ and for a tensor (spin 2) it is $|3\cos^2\theta_H - 1|^2$. Figure 1.7 shows plots of each distribution.

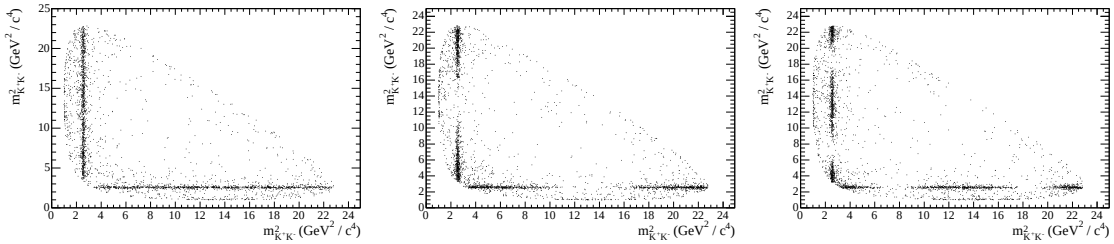

Figure 1.7: *Symmetrical Dalitz plots showing different helicity patterns of a fictitious resonance, with mass 1.6* GeV/c *and width 50* MeV*. The left most plot shows it as a scalar resonance, the central plot a vector and the right hand plot shows a tensor distribution.*

1.4.2 Interference

The main advantage that a Dalitz plot analysis has over a quasi-two-body approach when studying resonances is that the Dalitz approach can take into account and measure the interference between the different processes that contribute to the three-body final state. Consider the case of two such processes, a and b. Their decay amplitudes are given by $\mathcal{M}_a$ and $\mathcal{M}_b$ and the relative phase between the two is δ.

The total matrix element is then

$$|\mathcal{M}|^2 = \left|\mathcal{M}_a + \mathcal{M}_b e^{i\delta}\right|^2 \quad (1.45)$$

$$= |\mathcal{M}_a|^2 + |\mathcal{M}_b|^2 + 2\mathrm{Re}\left(\mathcal{M}_a \mathcal{M}_b^* e^{i\delta}\right) \quad (1.46)$$

As the decay rate is proportional to $|\mathcal{M}|^2$ it is important to take into account these cross-terms to properly measure the branching fractions of the various modes.

1.5 $B^{\pm} \to K^{\pm}K^{\mp}K^{\pm}$ Decay

$B^{\pm} \to K^{\pm}K^{\mp}K^{\pm}$ is a three-body B decay. Decay modes that contribute to this final state include the charmless decay channels $B^{\pm} \to K^{\pm}K^{\mp}K^{\pm}$*(nonresonant)*, $B^{\pm} \to f_0(980)K^{\pm}$, $B^{\pm} \to \phi(1020)K^{\pm}$and the non-charmless decay $B^{\pm} \to \chi_{c0}K^{\pm}$, where each of $f_0(980)$, $\phi(1020)$ and χ_{c0} decay to K^+K^-.

A "charmless" decay is one that occurs without a $b \to c$ transition. The charmless decays in this analysis occur via $b \to u\overline{u}s$ and $b \to s\overline{s}s$ transitions, and they are therefore suppressed, with branching fractions of the order 10^{-5}. This suppression of normal tree processes means that most charmless decays have large contributions from loop diagrams — generally named "penguin" processes (the $\phi(1020)$ mode actually has no contributing tree process). Figures 1.3 and 1.8 show decay diagrams for the various processes that contribute to $B^{\pm} \to f_0(980)K^{\pm}$ and $B^{\pm} \to \phi(1020)K^{\pm}$.

Initial analyses of $B^{\pm} \to K^{\pm}K^{\mp}K^{\pm}$ and its various constituent modes have been carried out at the intensity level [16], [17], [18]. In these cases the interference between intermediate resonances had to be treated as a source of systematic uncertainty. A full amplitude level Dalitz analysis is preferable as this source of uncertainty can be removed and the level of interference can be measured.

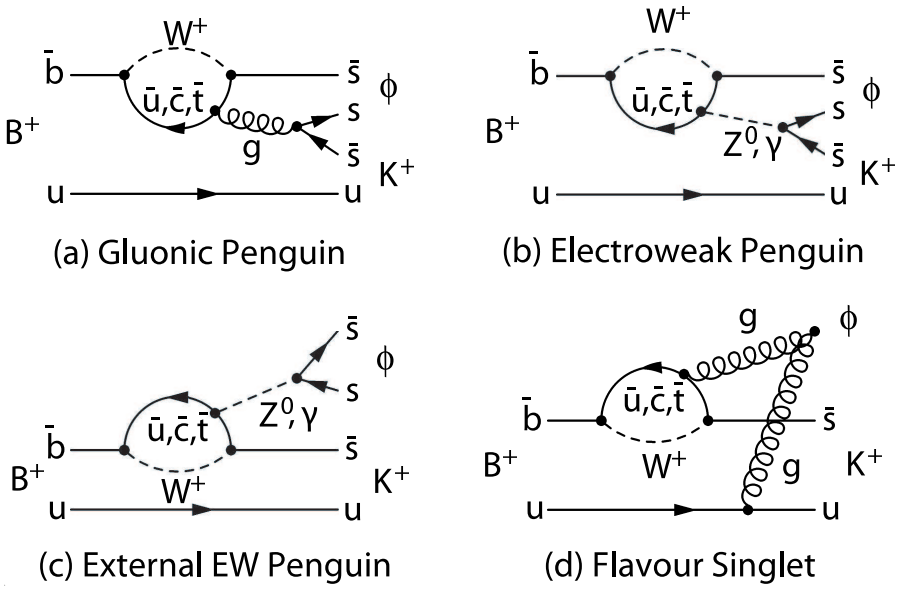

Figure 1.8: *$B^{\pm} \to \phi(1020)K^{\pm}$ decay diagrams.*

1.5.1 Motivation

There are a number of motivating factors for studying the $B^{\pm} \to K^{\pm}K^{\mp}K^{\pm}$ Dalitz plot. Most simply it is a natural progression from previous analyses of charmless two-body final state decays. Charmless decays provide new possibilities for *CP* violation searches. *CP* violation in $B^{\pm} \to \phi(1020)K^{\pm}$ is predicted by the Standard Model not to exceed a few percent [19], but $b \to s\bar{s}s$ is considered as a good potential source of new physics [20]. A major goal is therefore to measure any potential direct *CP* violation.

Much theoretical progress has been made in understanding strong interaction effects, with many predictions of branching fractions for pseudoscalar-pseudoscalar and pseudoscalar-vector processes. Table 1.3 shows the relevant predictions for this analysis. Further constraining the charmless B decay measurements will aid progress in this field.

Mode	Authors	Model	BF ($\times 10^{-6}$)	A_{CP} (%)
$B^{\pm} \to \phi(1020)K^{\pm}$	Chen *et al.* [21]	PQCD	$10.2^{+3.9}_{-2.1}$	–
	Cheng *et al.* [22]	QCDF	$4.3^{+3.0}_{-1.4}$	–
	Du *et al.* [23]	NF	3.8-3.9	–
	Du *et al.* [23]	QCDF	6.2-7.2	$1.0 - 1.4$
	Beneke *et al.* [19]	QCDF	2.5-11.6	$0.6 - 1.7$
	Chiang *et al.* [24]	$SU(3)$ fit	8.7 ± 0.4	–
$B^{\pm} \to f_0(980)K^{\pm}$	Cheng *et al.* [25]	QCDF	5.5-10.9	–
$B^{\pm} \to \chi_{c0}K^{\pm}$	Colangelo *et al.* [26]	QCDF	110-350	–

Table 1.3: *Theoretical predictions for modes that contribute to $B^{\pm} \to K^{\pm}K^{\mp}K^{\pm}$. Note that the branching fraction (BF) for $\phi(1020) \to K^+K^-$ is $(49.2 \pm 0.6)\%$. The BF for $f_0(980) \to K^+K^-$ is unknown and BF($\chi_{c0} \to K^+K^-$) $= (5.4 \pm 0.6) \times 10^{-3}$. PQCD = Perturbative Quantum chromodynamics factorisation, QCDF = QCD Factorisation, NF = Naive Factorisation, and SU(3) = Global fit to SU(3) flavour $B \to VP$ measurements.*

Measuring the branching fraction for $B^{\pm} \to f_0(980)K^{\pm}$, where $f_0(980) \to K^+K^-$, is important for further the understanding of the $f_0(980)$. Currently very few branching fractions of the $f_0(980)$ have been measured and it is of great interest to discover how strong its coupling to $K\overline{K}$ is.

As the $f_0(980)$ mass is just below the K^+K^- threshold a coupled-channel Breit-Wigner (or Flatté) is used to describe its amplitude [27],

$$\mathcal{A}(m) = \frac{1}{(m_0^2 - m) - im_0(\Gamma_\pi + \Gamma_K)}, \tag{1.47}$$

where m_0 is the $f_0(980)$ mass and

$$\Gamma_\pi(m) = g_\pi\sqrt{m^2 - 4m_\pi^2} \tag{1.48}$$

$$\Gamma_K(m) = g_K\sqrt{m^2 - 4m_K^2} \tag{1.49}$$

where m_π and m_K are the invariant masses of the pion and kaon, and g_π and g_K are experimentally determined coupling constants. There are a number of different measurements for g_π and g_K [28], [29] and [30], but we choose to use the results from the BES collaboration [28], as the BES numbers are the only ones to come directly from a joint $\pi^+\pi^-/K^+K^-$ analysis.

Now if I_K/I_π is defined to be the ratio of the integrals of the square of the amplitude across the $K^{\pm}K^{\mp}K^{\pm}$ and $K^{\pm}\pi^{\mp}\pi^{\pm}$ Dalitz plots, then the branching fraction ratio is given by

$$R \equiv \frac{BF(f_0(980) \to K^+K^-)}{BF(f_0(980) \to \pi^+\pi^-)} = \frac{3}{4}\frac{I_K}{I_\pi}\frac{g_K}{g_\pi}, \tag{1.50}$$

where BES gives $g_\pi/g_K = 4.21 \pm 0.25 \pm 0.21$. I_K/I_π is then calculated to be 0.29 and therefore $R = 0.92 \pm 0.07$.

The Particle Date Group list $f_0(980) \to K^+K^-$ merely as *seen* [9]. Recent $B^{\pm} \to K^{\pm}\pi^{\mp}\pi^{\pm}$ Dalitz analysis results give the product branching fraction of $B^{\pm} \to f_0(980)K^{\pm}$, where $f_0(980) \to \pi^+\pi^-$, as $9.2^{+0.8}_{-1.1} \times 10^{-6}$ [31], and so one could expect to see a BF for $B^{\pm} \to f_0(980)K^{\pm}$, where $f_0(980) \to K^+K^-$, of $\sim 8.7 \times 10^{-6}$.

A further physics goal is to determine the size and nature of the nonresonant contribution. Three-body decays of D-mesons have been studied extensively. A number of Three-body B-meson Dalitz analyses have now also been published. In most cases the nonresonant component was small and constant over the Dalitz plot [32], [33]. However a previous Belle collaboration Dalitz analysis of $B^{\pm} \to K^{\pm}K^{\mp}K^{\pm}$ showed a large, non-flat, nonresonant contribution [34].

1.5.2 Previous experimental results

$B^{\pm} \to K^{\pm}K^{\mp}K^{\pm}$ has a good signal to background ratio for a charmless B decay, but it is not expected to yield any large branching fraction asymmetries. *BABAR* has

previously measured the $B^{\pm} \to K^{\pm}K^{\mp}K^{\pm}$ branching fraction to be $(29.6 \pm 2.1 \pm 1.6) \times 10^{-6}$, with an asymmetry of $0.02 \pm 0.07 \pm 0.03$ using a sample of 81.8 fb.

Many different analyses, carried out by various collaborations, have investigated the constituent decays of the $B^{\pm} \to K^{\pm}K^{\mp}K^{\pm}$ Dalitz plot, but most have been intensity level analyses. Recently BELLE published a $B^{\pm} \to K^{\pm}K^{\mp}K^{\pm}$ Dalitz analysis [34], and they did not find any evidence for the $f_0(980)$. Past experimental results are collated in Table 1.4.

Mode	Collaboration	BF ($\times 10^{-6}$)	A_{CP} (%)
$B^{\pm} \to K^{\pm}K^{\mp}K^{\pm}$ (charmless total)	*BABAR* [17]	$29.6 \pm 2.1 \pm 1.6$	$2 \pm 7 \pm 3$
	BELLE [34]	$30.6 \pm 1.2 \pm 2.3$	–
$B^{\pm} \to K^{\pm}K^{\mp}K^{\pm}$ (nonresonant)	BELLE [34]	$24.0 \pm 1.5 \pm 1.8^{+1.9}_{-5.7}$	–
$B^{\pm} \to \phi(1020)K^{\pm}$ ($\phi(1020) \to K^{+}K^{-}$)	BELLE [34]	$4.72 \pm 0.45 \pm 0.35^{+0.39}_{-0.22}$	–
$B^{\pm} \to \phi(1020)K^{\pm}$ ($\phi(1020) \to$ all)	*BABAR* [35]	$10.0^{+0.9}_{-0.8} \pm 0.5$	$4 \pm 9 \pm 1$
	BELLE [34]	$9.60 \pm 0.92 \pm 0.71^{+0.78}_{-0.46}$	–
	CDF [36]	$7.6 \pm 1.3 \pm 0.6$	-7 ± 17
	CLEO [16]	$5.5^{+2.1}_{-1.8} \pm 0.6$	–
$B^{\pm} \to f_0(980)K^{\pm}$ ($f_0(980) \to \pi^{+}\pi^{-}$)	*BABAR* [32]	$9.47 \pm 0.97 \pm 0.46^{+0.42}_{-0.75}$	$8.8 \pm 9.5 \pm 2.6^{+9.5}_{-5.0}$
	BELLE [34]	$7.55 \pm 1.24 \pm 0.69^{+1.48}_{-0.96}$	–
$B^{\pm} \to f_0(980)K^{\pm}$ ($f_0(980) \to K^{+}K^{-}$)	BELLE [34]	< 2.9	–
$B^{\pm} \to \chi_{c0}K^{\pm}$ ($\chi_{c0} \to K^{+}K^{-}$)	*BABAR* [18]	$1.49^{+0.36}_{-0.34} \pm 0.11$	–
	BELLE [34]	$0.86 \pm 0.26 \pm 0.06^{+0.20}_{-0.05}$	–
$B^{\pm} \to \chi_{c0}K^{\pm}$ ($\chi_{c0} \to$ all)	*BABAR* [18]	270 ± 70	–
	BELLE [34]	$196 \pm 35 \pm 33^{+197}_{-26}$	–

Table 1.4: *Previous experimental results for modes that contribute to $B^{\pm} \to K^{\pm}K^{\mp}K^{\pm}$. The BELLE results all come from their Dalitz analysis of $B^{\pm} \to K^{\pm}K^{\mp}K^{\pm}$. Measurements for $B^{\pm} \to f_0(980)K^{\pm}$ ($f_0(980) \to \pi^{+}\pi^{-}$) are listed as a guide — the $f_0(980) \to K^{+}K^{-}$ decay is predicted to be $\sim 0.92 \times BF(f_0(980) \to \pi^{+}\pi^{-})$.*

The measurement that stands out the most is that of the BELLE Dalitz analysis

which found no evidence of the decay $B^{\pm} \to f_0(980)K^{\pm}$ ($f_0(980) \to K^{+}K^{-}$). This is perhaps explained by the fact that they use older g_{π}/g_K numbers from E791 [29].

2

The *BABAR* Experiment

2.1 Introduction

The *BABAR* experiment was designed primarily to study *CP* violating asymmetries in the decays of B mesons. It was constructed at the Stanford Linear Accelerator Center (SLAC) to take advantage of the SLAC linac, which is used to accelerate electrons and positrons before feeding them into the *BABAR*'s e^+e^- collider, named PEP-II (Positron Electron Project-II). An overview of the layout of the experiment can be seen in Figure 2.1. PEP-II has two storage rings, one containing 9 GeV

electrons, and the other containing positrons at 3.1 GeV. They travel along two vacuum tubes, guided by magnets before being focussed to collide in the centre of the *BABAR* detector. The design luminosity is 3 x $10^{33}\,\mathrm{cm}^{-2}\mathrm{s}^{-1}$ (about 1/4 million $B\overline{B}$ pairs per day – the best achieved is just over 3/4 million). This luminosity is required as many of the decays used to measure *CP* violation have very low branching fractions in the region of 10^{-4}-10^{-6}.

A collision at these energies gives a centre-of-mass energy ($\sqrt{s}$) of 10.58 GeV – this is at the centre of the $\Upsilon(4S)$ $b\bar{b}$ resonance, which is the lightest meson that can decay to $B\overline{B}$ (the branching fraction for $\Upsilon(4S) \rightarrow B\overline{B}$ is >96%). The $e^+e^- \rightarrow \Upsilon(4S)$ cross-section is 1.09nb, to $q\overline{q}$ (where $q = u$, d, s or c) the cross-section is 3.2nb and to $\tau^+\tau^-$ it is 0.9nb.

As the beams have asymmetric energies the $\Upsilon(4S)$ meson is produced with a boost in the laboratory frame of $\beta\gamma = 0.56$, allowing the lifetimes of the $B\overline{B}$ to be measured from their decay lengths. Knowledge of the lifetimes is needed for the measurements of any (*CP*) time-dependence in their decay rates. Also important to the measurement of time-dependent *CP* violation is the fact that the B mesons produced by the decay of the $\Upsilon(4S)$ are coherent, i.e. determining ('tagging') the flavour of one meson means that the flavour of the other is known at the time the tagged meson decayed.

About 1/12th of the time the experiment runs at about 40MeV below the $\Upsilon(4S)$ resonance. This *off-peak* running is so that non-$B\bar{B}$ backgrounds can be studied, as there is no B pair production below the resonance.

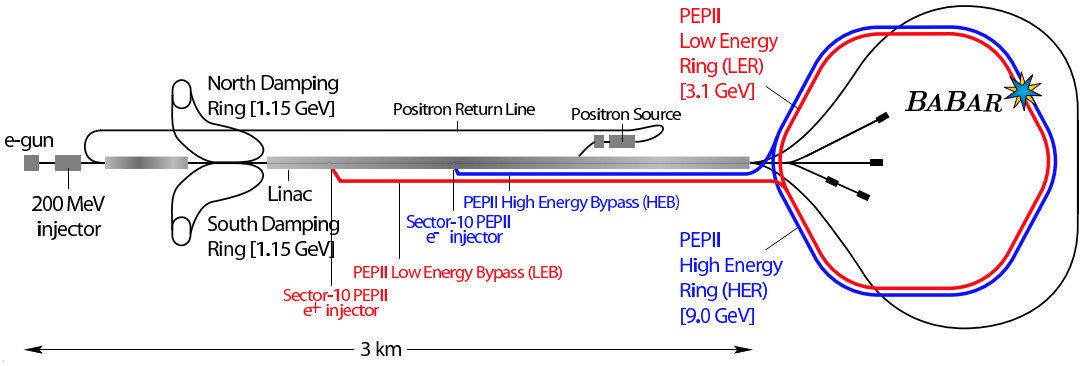

Figure 2.1: *Overview of the SLAC linac and the PEP-II rings*

2.2 The Asymmetric B Factory — PEP-II

A complete description of PEP-II can be found at [37]. The need for asymmetric beams means that the electrons and positrons must be kept in separate storage rings. Studies made [38] found that a ratio 3:1 between the high (HER) and low energy rings (LER) was optimal. Table 2.1 shows values for many of the most important parameters for PEP-II.

2.2.1 The Interaction Point

To achieve the needed high luminosities the beams are divided up into ∼1500 low charge bunches, minimising beam-beam interference. The bunches must be brought into focus at the interaction point (IP), but separated immediately afterward so as to avoid secondary collisions. Operating at design parameters secondary collisions would happen 62cm away from the interaction point if the beams were not separated.

Figure 2.2 shows the layout of the interaction region. QD4 and QF5 are quadrupoles used for focusing the HER, whereas QF2 focuses the LER. Each of these magnets lie outside the *BABAR* detector. QD1 are the final focusing magnets for both beams

Table 2.1: *Parameters of the PEP-II machine. Numbers correct as of October 2005 [39].*

Parameters	Design	Present in collision
Energy HER (GeV)	9.0	9.0
Energy LER (GeV)	3.1	3.1
Current HER (mA)	750	1615
Current LER (mA)	2140	2650
Number of bunches	1658	1732
Bunch length (mm)	15	11-12
Luminosity (10^{33} $\mathrm{cm}^{-2}\mathrm{s}^{-1}$)	3.0	9.0
Luminosity (pb^{-1}/day)	130	662

and lies mostly within the detector. The B1 separation dipoles lie completely within the detector volume and as such affect the detector acceptance.

The IP has a size of about 130 μm in the x direction, 5.6 μm in y and 9mm in z. See Figure 2.4 for an illustration of how the different axes relate to the *BABAR* detector.

2.2.2 Backgrounds

Machine backgrounds cause deadtime within the detector, leading to the loss of interesting physics events, and can also result in radiation damage to the detector subsystems. There are a number of different machine backgrounds and each one is exacerbated by the high luminosities needed at *BABAR*.

Synchrotron radiation is more of a problem at *BABAR* than most e^+e^- machines due to the complicated optics near the IP. To minimise its effect the geometry of the

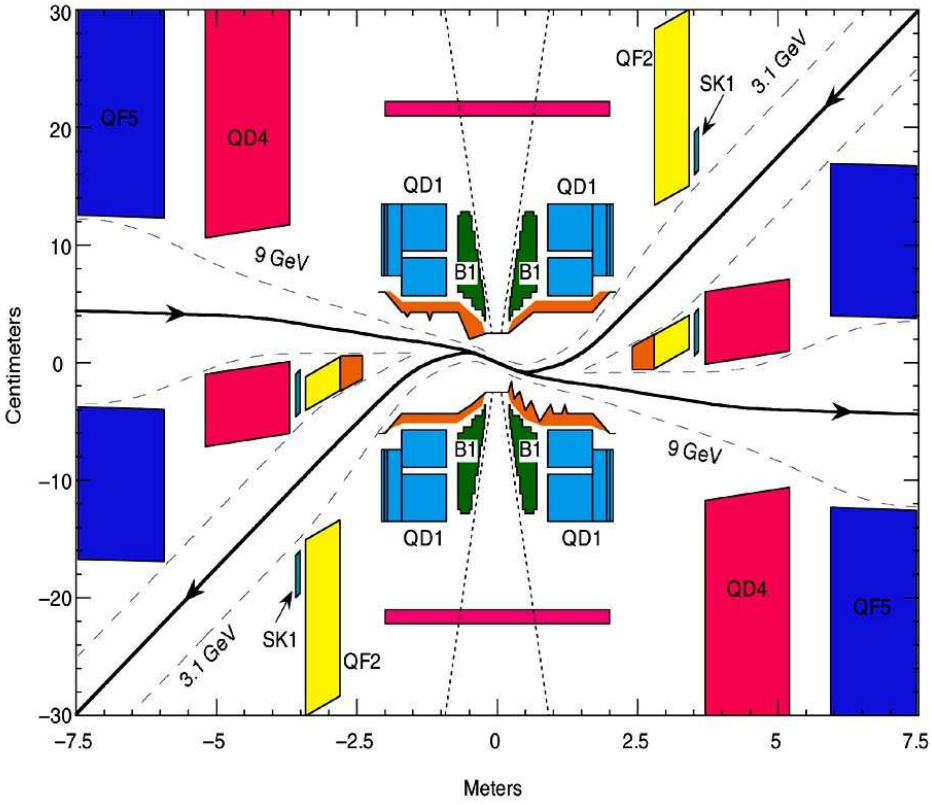

Figure 2.2: *Plan view of the PEP-II interaction region (vertical scale is exaggerated). Focusing quadrupoles are labelled Qx1-5 and separation dipoles B1.*

interaction region was designed so that most of the radiation would pass through the detector without interactions. Also copper masks are used to reduce interactions with the beam pipe.

A second form of background is from 'lost' beam particle interaction with the beam pipe wall, causing electromagnetic showers. A particle may become lost through interaction with gas molecules in the beam pipe or bremsstrahlung radiative losses. This form of background is minimised by having an excellent vacuum in the region

near the IP.

2.2.3 Performance

PEP-II has performed excellently since turning on in May 1999. It achieved its design goals within the first few years and now surpasses them by a large margin. In the last year one of the main boosts to luminosity came from the introduction of trickle injection from December 2003 in the LER and March 2004 in the HER. Instead of turning the detector off while the beams are topped up, the beams are continuously topped up by a very low rate 'trickle', thus removing a large inefficiency from machine running. The effect of this and other ongoing improvements to PEP-II can be seen in Figure 2.3.

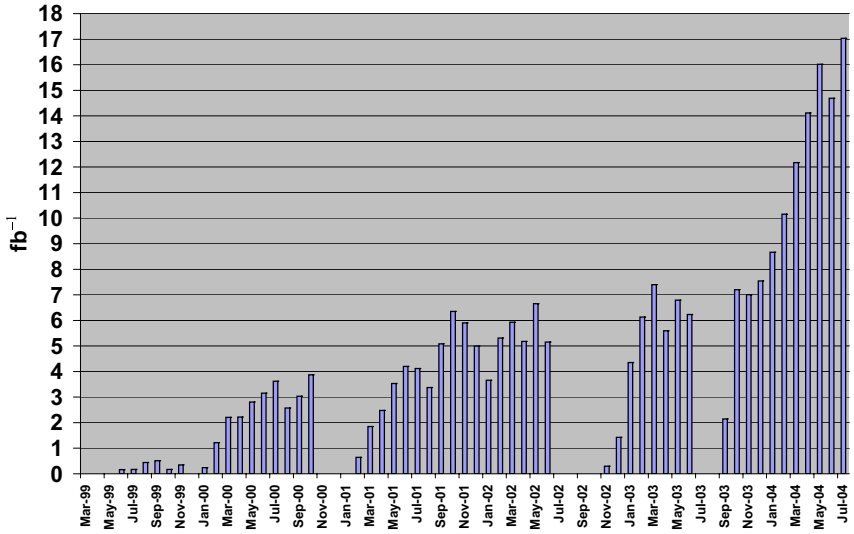

Figure 2.3: *PEP-II integrated luminosity per month [40].*

The total luminosity delivered up to the end of July 2004 was 256 fb^{-1} which includes all the data used in the following analysis.

2.3 The *BABAR* Detector

A full description of the *BABAR* detector can be found in [41]. Unless otherwise stated all numbers quoted in this chapter are taken from there.

BABAR is a general purpose detector designed to make precision measurements of the angles of the Unitary Triangle through studying time-dependent *CP* violation in neutral B decays. It is also used for precision measurements of B, tau and charm physics. Figure 2.4 shows side and end views of the *BABAR* detector and illustrates the *BABAR* coordinate system.

The main design aims of the detector were for:

- ◇ High reconstruction efficiency for both charged and neutral particles.
- ◇ Good momentum and position resolution for charged particles over the range 60 MeV-4 GeV.
- ◇ Good energy and angular resolution for neutral particles over the range 20 MeV-4 GeV.
- ◇ Excellent vertex resolution in all three dimensions, but especially in z (see Figure 2.4) for the measurement of B decay vertices needed for time-dependent *CP* measurements.
- ◇ Excellent particle identification to distinguish between e, μ, $\pi^{\pm}$, $K^{\pm}$ and p over a broad kinematic range. This is particularly important for distinguishing between important, but similar, final state decays such as $B^0 \to \pi^+\pi^-$ and $B^0 \to K^+\pi^-$.
- ◇ The greatest possible angular acceptance in the centre-of-mass frame.
- ◇ The ability to operate in high background conditions.

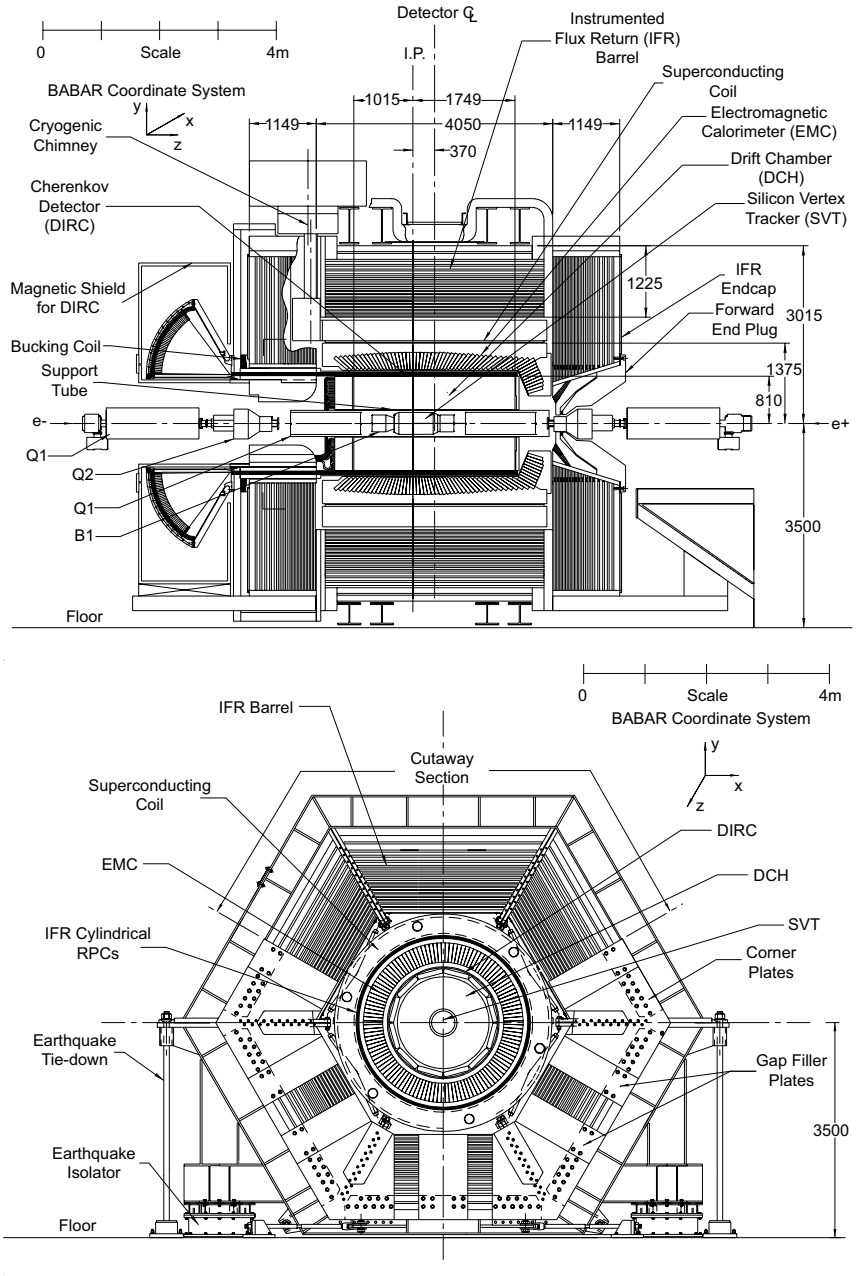

Figure 2.4: *The BABAR Detector. The BABAR co-ordinate system is shown. z is in the direction of the HER beam. y is vertically upward while x points horizontally away from the centre of the PEP-II rings and θ and ϕ are defined as in the standard polar co-ordinate system*

BABAR has several main components, each of which plays a part in achieving the above goals. They are the Silicon Vertex Tracker (SVT), the Drift Chamber (DCH), the Detector of Internally Reflected Cherenkov radiation (DIRC), the ElectroMagnetic Calorimeter (EMC) and the Instrumented Flux Return (IFR).

For good momentum resolution a strong magnetic field is needed over the SVT and DCH. This is provided by a 1.5T superconducting solenoid placed between the EMC and IFR so as not to block particle trajectories before measurement in the DIRC and EMC. The coil has an inner radius of 1.4m. The coil and cryostat combined are between 0.25 and 0.4 radiation lengths thick — thin enough to allow hadrons to pass reasonably well to the IFR.

2.4 The Silicon Vertex Tracker (SVT)

2.4.1 SVT Physics Requirements

The primary goal of the SVT is to provide precise position measurements of the B meson decay vertices that are essential for time-dependent CP studies. Monte Carlo studies [42] showed that a z resolution of $\approx 80\mu$m is needed.

The SVT is the only subsystem capable of measuring charged particles with transverse momenta (p_T) less than $120\,\mathrm{MeV}/c$ as they will not reach the DCH due to magnetic-field-induced curvature. Therefore high tracking efficiencies at these low energies is required. Such particles include slow pions from the decays of D^* mesons which are very common B-decay products.

The SVT finally is used in particle identification, measuring the rate of energy loss ($\mathrm{d}E/\mathrm{d}x$) for particles with momenta less than $700\,\mathrm{MeV}/c$.

2.4.2 SVT Design

The SVT is made up of five concentric layers of double-sided silicon strip sensors. The strips on either side are arranged orthogonally to each other so as to measure both ϕ and z. The arrangement of the layers is detailed in Figures 2.5 and 2.6. The arched design of the outer two layers minimises the amount of material that a particle must traverse down to $\sim$4% of a radiation length (to minimise bremsstrahlung and multiple scattering) whilst also maximising the angular coverage (90% of the solid angle in the centre-of-mass frame).

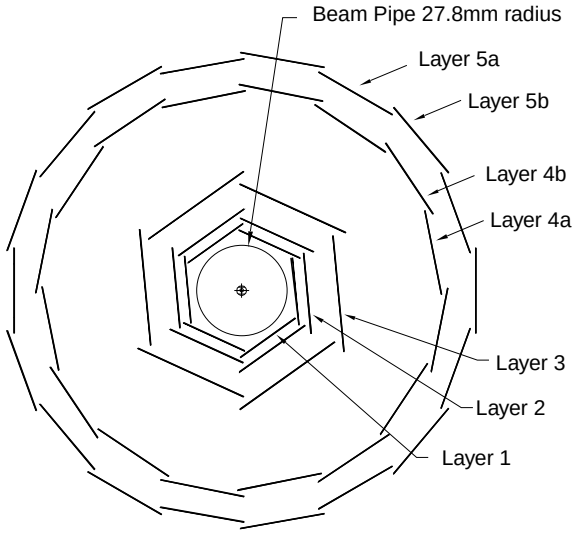

Figure 2.5: *End view of the SVT showing the layered structure. The radii of the layers are 1 = 32 mm, 2 = 40 mm, 3 = 54 mm, 4a = 124, 4b = 127 mm, 5a = 140 mm and 5b = 144 mm.*

The inner three layers each contain 6 modules and are positioned very close to the beam pipe at radii of 3-5cm from the IP. The primary role of these layers is to acquire precision measurements for the calculation of the vertex. The outer two layers contain 16 and 18 modules respectively and are mainly used for alignment with the DCH. Because of the geometry of these outer layers they cannot be tilted to overlap like the inner layers. As such they are arranged into sub-layers 4a/4b and

5a/5b as seen in Figure 2.5.

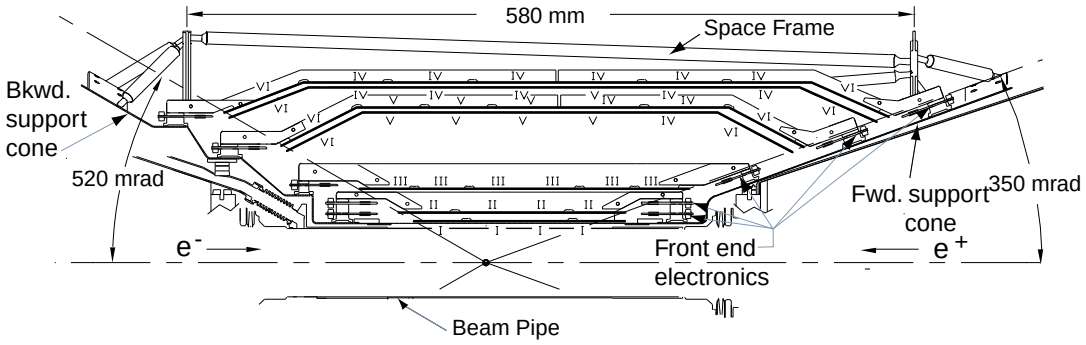

Figure 2.6: *Side on view of the SVT showing the arched design of the outer layers*

Each module as well as being double-sided is further divided into forward and backward halves, all of which are read out by electronics placed outside the detector acceptance. When an ionized particle passes through a module an electric pulse is generated. The signal is amplified and shaped and then compared to a predetermined threshold. The length of 'time over threshold' measurement is approximately logarithmically related to the deposited charge, allowing a large dynamic range to be covered.

Finally the SVT has been designed to withstand an integrated radiation of 2MRad over its lifetime, or an instantaneous dose of 1Rad/ms.

2.4.3 SVT Performance

Good alignment of the SVT is essential for getting the best position and momentum measurements. Local alignment determines the positions of modules with relation to one another and global alignment determines the position of the SVT with respect to the other subdetector systems. Two-pronged di-muon events and also some cosmic

ray events are used for calibration. For the global alignment there must be strong tracks left in both the SVT and DCH.

The resolution is found to be better than 40μm for both z and ϕ in each of the inner three layers, giving a three dimensional vertex resolution of better than 70μm. The efficiency of the detector, measured using data, is 97% (excluding defective sections).

The dE/dx resolution is found to be 14%. This gives a 2σ separation of pions and kaons up to 600 MeV/c and between kaons and protons to 1 GeV/c.

Defective sections currently account for fewer than 5% of the total 208. Replacement modules for the SVT are under construction and are will be installed in the next major shutdown, currently scheduled to be August 2006.

2.5 The Drift Chamber (DCH)

2.5.1 DCH Physics Requirements

The DCH is the main charged particle detector in *BABAR*. It has primary responsibility for position and momentum measurements for particles with p_T in the range 0.1-5.0 GeV/c. It is also needed for particle identification (PID) using dE/dx measurements – this is especially important at energies below 700 MeV/c where the DIRC is not effective. For good PID a minimum dE/dx resolution of 7% is needed.

The DCH is also needed to provide tracking and timing information to the trigger, and must be able to perform in high background conditions.

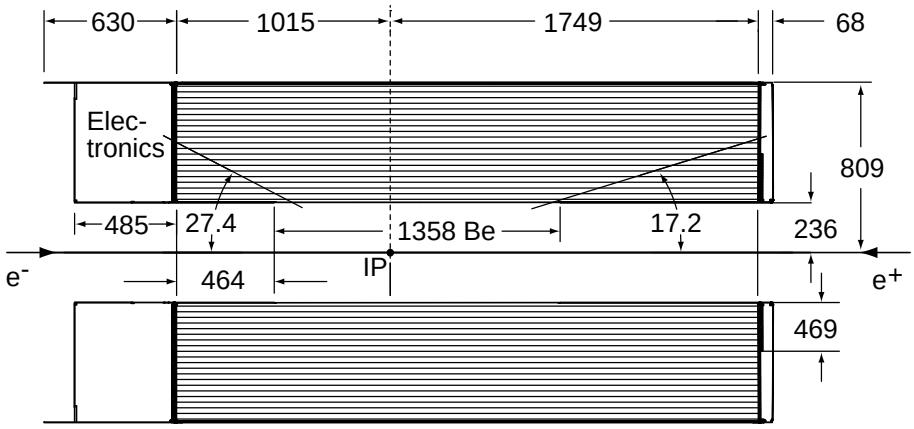

Figure 2.7: *Side-on view of the DCH. All distances are in mm.*

2.5.2 DCH Design

The DCH consists of drift cells in a concentric arrangement around the SVT. The resulting 2.8m long cylinder is placed asymmetrically (see Figure 2.7) with respect to the interaction point so as to increase acceptance in the forward direction, i.e. the direction of the 9 GeV/c^2 e^- beam.

There are 40 layers of drift cells. These are grouped into 10 super-layers of 4 layers each, overall providing up to 40 measurements of space co-ordinates per track. The design of the innermost four super layers is shown in Figure 2.8. Each cell is typically $1.2 \times 1.8\,\mathrm{cm}^2$ and consists of one sense wire ($20\,\mu\mathrm{m}^2$ diameter gold plated aluminium) surrounded by six field wires ($120\,\mu\mathrm{m}^2$ diameter gold plated aluminium). Multiple scattering is minimised by using low mass wires and by filling the cells with a helium-based mixture (helium and isobutane in a 4:1 ratio). Overall the gas and wires constitute 0.28% of a radiation length for a particle travelling through the detector.

There are 4 axial (A) super-layers, for measuring z, and 6 stereo (U, V) super-layers, for measuring ϕ, and they are arranged in the pattern AUVAUVAUVA. The stereo

angle varies from 45mr in the innermost super-layer to 76mr in the outermost.

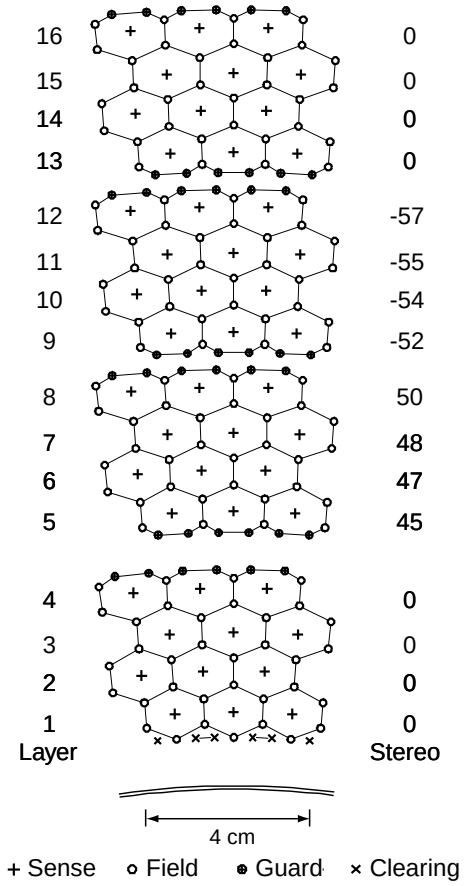

Figure 2.8: *Cell layout for the four DCH super-layers*

As a charged particle passes through the gas it ionises molecules along its path. These ions drift toward the sense wire, generating an avalanche of charge which serves to amplify the signal. The drift time is measured using the leading edge of the signal, which is digitised with a 1ns resolution. The total charge in the pulse is summed for the $\mathrm{d}E/\mathrm{d}x$ measurement.

The drift chamber was designed to withstand an integrated radiation dose of 20 kRad.

2.5.3 DCH Performance

The DCH dominates *BABAR* tracking efficiency and p_T resolution. The track efficiency is measured by comparing the number of reconstructed tracks to the number of tracks detected by the SVT that should fall within DCH acceptance.

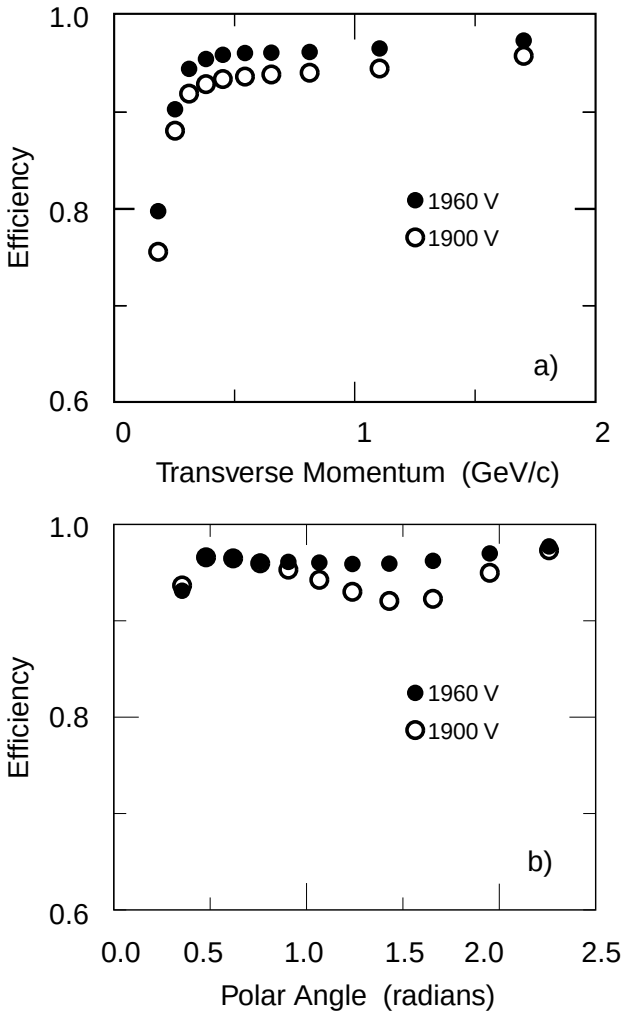

Figure 2.9: *Tracking efficiency of the DCH, shown as a function of p_T (top) and polar angle (bottom).*

Figure 2.9 shows the efficiency as a function of momentum and polar angle for the voltages 1900V and 1960V. The lower voltage was used during the early running of

BABAR due to a mistake while commissioning the DCH. Throughout this period the average tracking efficiency was only about 93% as opposed to the design value of $(96 \pm 1)\%$ (at 1960V). It was decided that 1900V gave too poor an efficiency, but using 1960V would reduce the lifetime of the detector too much, and so from 2001 onward the DCH has operated at a compromise voltage of 1930V. However, with improved track finding code the DCH has been able to operate at design efficiency.

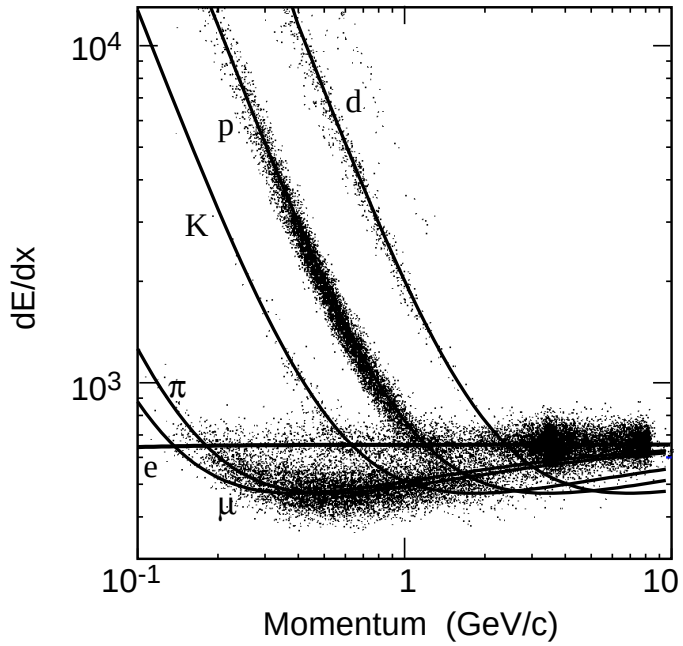

Figure 2.10: *dE/dx measurements for various particles in the DCH as a function of momentum. The expected Bethe-Bloch curves are overlaid.*

The DCH is calibrated using bhabha and di-muon events. The calibration is performed for each cell. The drift distance is estimated using the best fit to the track in question (the cell being calibrated is excluded from the fit). $\mathrm{d}E/\mathrm{d}x$ measurements also need to be calibrated to take account of potential biases from changing gas temperature and pressure. There is good pion/kaon separation up to around $0.7\,\mathrm{GeV}/c$ as seen in Figure 2.10.

The $\mathrm{d}E/\mathrm{d}x$ resolution is typically 7.5% which is close to the design value of 7.0%.

The single cell resolution is $125\,\mu\mathrm{m}^2$ and the drift time is about 1ns. The momentum resolution is given by

$$\sigma p_T/p_T = (0.13 \pm 0.01)\% \cdot p_T + (0.45 \pm 0.03)\% \tag{2.1}$$

where p_T is the transverse momentum in GeV/c.

2.6 The Detector of Internally Reflected Cherenkov Radiation (DIRC)

2.6.1 DIRC Physics Requirements

The DIRC is the main charged hadron particle identification system at *BABAR*. Differentiating between pions and kaons is essential for effective B flavour tagging, needed for CP studies. It is also crucial for identification of rare B decay states involving pions and kaons such as the analysis described in this document. As the useful particle identification abilities of the SVT and DCH extend no further than 700 MeV/c there is a need for another system to extend *BABAR*'s range to 4.2 GeV/c – the DIRC.

The DIRC must also be sufficiently thin (at least in terms of radiation lengths) to not effect the energy measurements of the calorimeter.

2.6.2 DIRC Design

The DIRC is made up of 144 synthetic quartz bars arranged into a twelve-sided polygon around the DCH. The refractive index (n) of quartz is 1.472. When a charged particle traverses the quartz at a velocity of greater than c/n it will emit a

Cherenkov light cone at an angle $\cos\theta_c = 1/n\beta$ to its direction of travel. A portion of this light is trapped within the quartz by total internal reflection ($\theta_c = 42.8°$) and then travels to the water-filled standoff box at the backward end of the detector (a mirror is positioned at the forward end). Figure 2.11 shows the overall DIRC geometry and Figure 2.12 shows a more detailed schematic of the standoff box and a quartz bar.

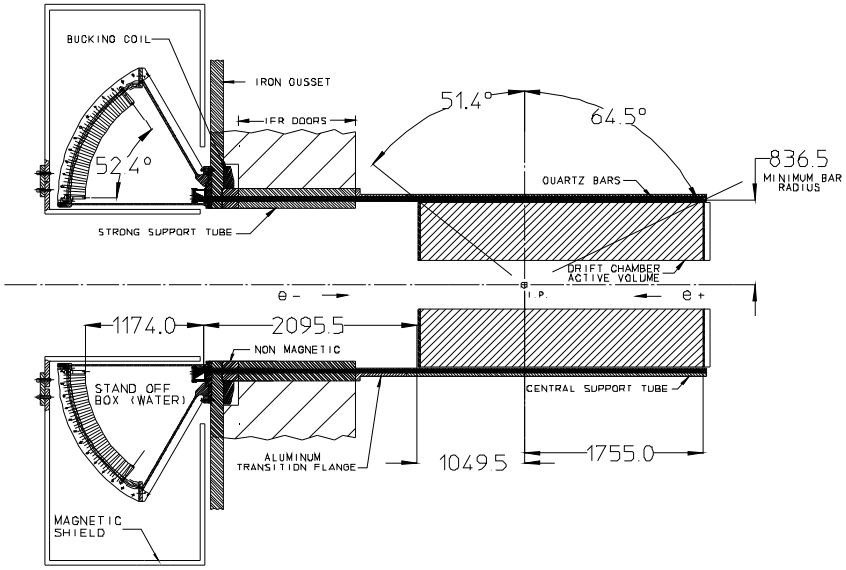

Figure 2.11: *Elevation view of the DIRC. Distances are in mm.*

The standoff box is instrumented by 10,752 photomultiplier tubes (PMTs) and contains 6000 litres of purified water. Each PMT has a diameter of 28.2mm and is surrounded by a light catcher to increase its acceptance. Magnetic shielding surrounds the standoff box to prevent the *BABAR* solenoid from interfering with the PMTs. The signal detected by the PMTs is a conic section, with opening angle being the Cherenkov angle (given adjustments for the quartz/water boundary).

The DIRC acceptance covers 94% in the azimuth and 83% in the polar angle. The quartz bars have a radial thickness of 8cm, which is approximately 17% of a radiation length.

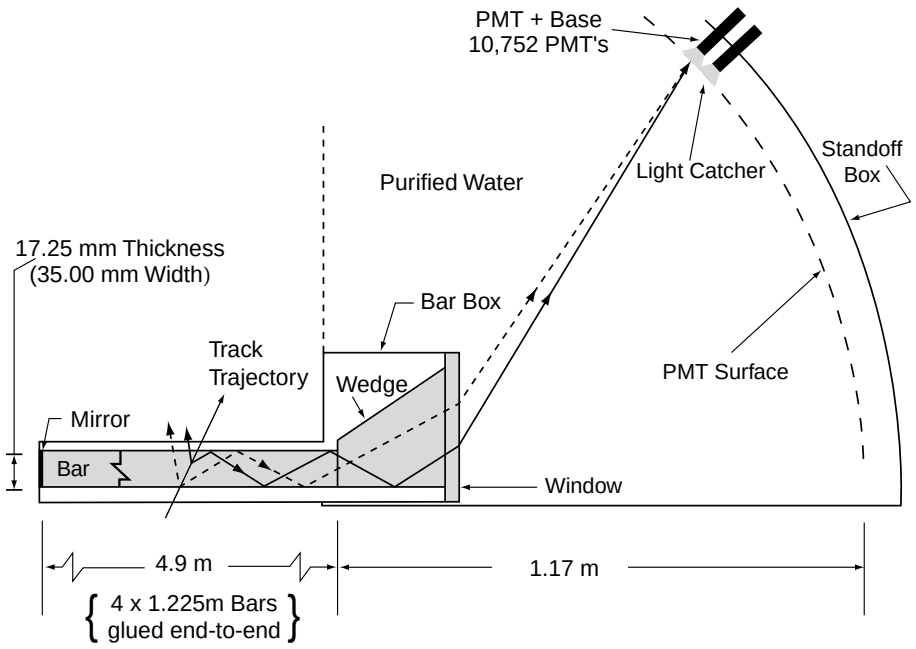

Figure 2.12: *Schematic diagram of a DIRC radiator bar and water-filled standoff box, showing a typical photon's path.*

2.6.3 DIRC Performance

Figure 2.13 shows the pion/kaon separation provided by the DIRC versus track momentum. A separation of 4σ is achieved at $3\,\mathrm{GeV}/c$. The $K^{\pm}$ identification efficiency is 85-97%, while the proportion of pions misidentified as kaons is $\sim$3%.

Figure 2.14 shows the $\pi^{\pm}K^{\mp}$ mass spectra around the D^0 mass with and without the use of the DIRC for particle identification.

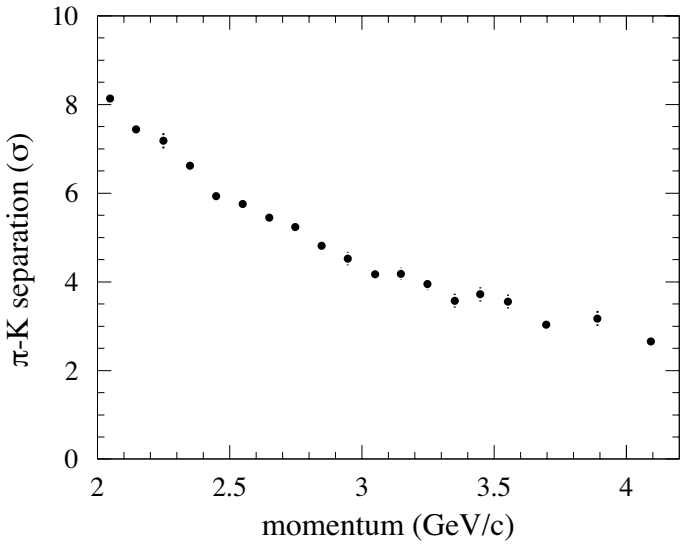

Figure 2.13: *DIRC pion/kaon separation as a function of track momentum.*

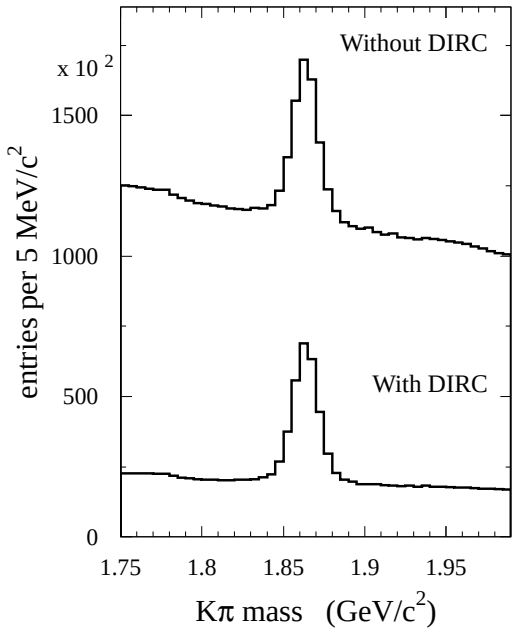

Figure 2.14: *A comparison of the invariant $\pi^{\pm}K^{\mp}$ mass spectrum with and without using the DIRC for particle identification.*

2.7 The ElectroMagnetic Calorimeter (EMC)

2.7.1 EMC Physics Requirements

The EMC is a positional calorimeter. It is the only subsystem able to detect photons and as such needs to have precise energy and angular resolution. It is important to reconstruct the photons well so as to have good reconstruction efficiency for π^0 and η, which are decay products in many important B-decays. 50% of the photons from π^0 decay have energies less than 200 MeV, so it is essential to have good low energy measurement. Photons from processes such as $e^+e^- \to e^+e^-\gamma$ and $e^+e^- \to \gamma\gamma$ can have energies up to 9 GeV. These decays are important for calibration and so overall the EMC must cover an energy range from 20 MeV to 9 GeV. The EMC also provides particle identification for electrons and neutral hadrons.

2.7.2 EMC Design

The calorimeter is made from 6580 thallium-doped caesium iodide crystals. The barrel section comprises 48 rings of 120 crystals and there is also a forward endcap containing 8 rings with a total of 820 crystals. There is no backward endcap to keep costs down. Figure 2.15 is a cross-section of the EMC showing the layout of the rings and how they are directed toward the interaction point. The acceptance covers 90% of the solid angle in the centre-of-mass frame.

CsI was chosen for its high light yield, small Molière radius (radius of spread of electromagnetic showers) and short radiation length. CsI also emits at a wavelength detectable by silicon photodiodes. Pure CsI is however a very soft and pliable material making it extremely difficult to polish, thus compromising performance. With the addition of thallium CsI becomes fully solid and therefore a more useful

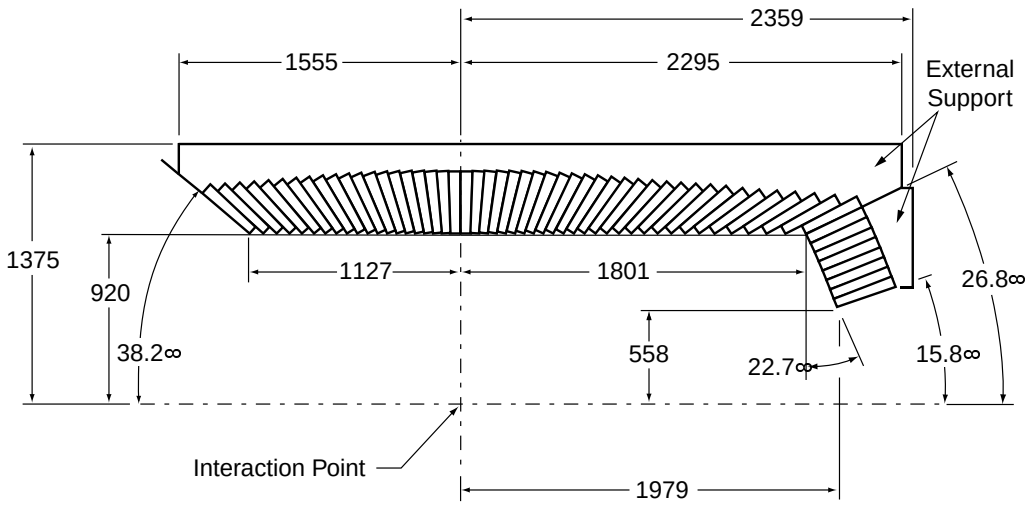

Figure 2.15: *Cross-sectional side-on view of the top half of the EMC, all dimensions are in mm.*

scintillator.

The CsI crystals vary in length from 29.6cm (16.1 radiation lengths) in the backward end of the EMC to 32.4cm (17.6 radiation lengths) at the forward end. The endcap crystals are also 32.4cm long. All crystals have a front face area of $\sim 5\,\mathrm{cm}^2$, comparable with the size of the Molière radius. This is designed to cause electromagnetic showers to fall into surrounding crystals, making a cluster.

The scintillation light is detected by a pair of silicon photodiodes glued to the rear end of each crystal.

2.7.3 EMC Performance

There are a number of ways in which the EMC must be calibrated. Light yields vary across the different crystals as well as being non-uniform with respect to energy deposited. The yields also change with time due to radiation damage.

Low energy calibration is performed using a 6.13 MeV radioactive source. Electrons from bhabha events are used for calibration over the range 50 MeV–7.5 GeV and photons from π^0 decay are also used up to 5 GeV.

2.8 The Instrumented Flux Return (IFR)

2.8.1 IFR Physics Requirements

The IFR acts as a muon detector, a neutral hadron calorimeter and also serves as a flux return for *BABAR*'s superconducting magnet. Good muon and K_L^0 identification is essential for many important time-dependent *CP* analyses (e.g. $B \to J/\psi\, K_L^0$, $J/\psi \to \mu^+\mu^-$).

It is required to resolve muon energies down to 1GeV/c, and position to ∼3.5cm along each axis.

2.8.2 IFR Design

The IFR is the outermost subsystem of the *BABAR* detector and is the main support for the other subsystem structures. The steel flux return is instrumented with resistive plate chambers (RPCs). It is made from 19 layers of RPCs in the barrel, each split into 3 modules in the z direction. The endcaps have 18 layers each split horizontally into 6 modules as seen in Figure 2.16. There are an additional two cylindrical layers placed between the EMC and the magnet cryostat to help link EMC clusters to IFR tracks.

The RPCs detect streamers from capacitive readout strips. Each RPC consists of a

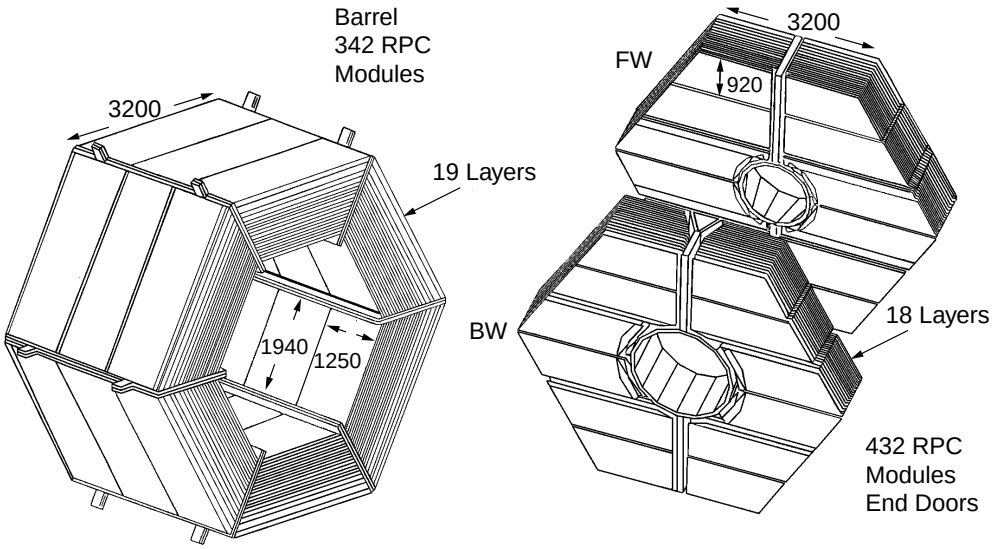

Figure 2.16: *Diagram showing IFR barrel and endcap geometry, all dimensions are in mm.*

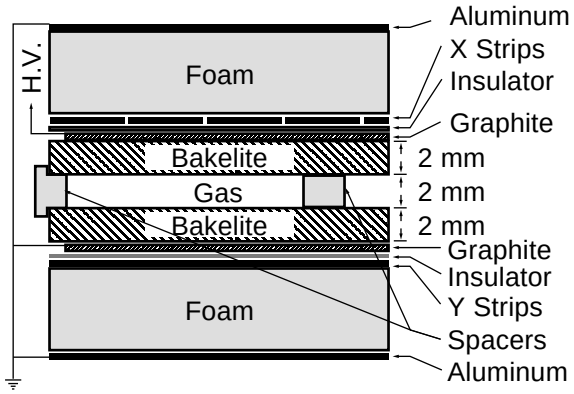

Figure 2.17: *Cross-section of a RPC*

pair of 2mm bakelite layers sandwiching a gas mixture of 57% argon, 39% freon and 4% isobutane (see Figure 2.17). The outer face of each bakelite sheet is coated with graphite, then an insulation layer. Outside that is a layer of aluminium readout strips (labelled X and Y strips on Figure 2.17), one side having strips in the z direction and the other side having strips to measure ϕ. The strips have a pitch of

between 2.17-3.85cm.

2.8.3 IFR Performance

BABAR has had ongoing problems with the IFR system. In summer 1999 it gave a mean muon efficiency of 90% over a momentum range of 1.5-3.0 GeV/c, but over time this quickly deteriorated. By the end of spring 2002 the efficiency had fallen to ∼65%. 'Dead' RPCs have been removed and examined, but no definitive conclusion could be drawn as to why they failed.

The endcap RPCs were replaced in summer 2002 by more efficient double-gap chambers, but five layers have been replaced with brass to increase absorbency. Six layers in the barrel have also been replaced with brass, with the remaining active layers being replaced by Limited Streamer Tubes (LSTs) which are described in [43]. Two sides of the hexagonal barrel were installed in summer 2004, with the remaining four due to be installed in summer 2006.

The endcap upgrade has restored its average efficiency to 90% and the installed LSTs also show 90% efficiency.

2.9 The Trigger

The trigger system is used to filter interesting physics events from a substantial background noise, thus reducing the data flow to a manageable rate for storage and off-line processing. Interesting physics events include $B\overline{B}$, $q\overline{q}$ and $\tau^+\tau^-$. The backgrounds come from Bhabha events, radiative Bhabha events, beam backgrounds (described in Section 2.2.2) and two photon events.

The *BABAR* trigger system comprises the Level 1 (L1) hardware based trigger, which then passes events to the Level 3 (L3) software trigger. Any events that pass the L3 trigger are then stored by the data acquisition system.

2.9.1 The Level 1 Trigger

The PEP-II bunch crossing rate is about 238MHz. The L1 trigger is required to reduce the event rate to less than 2kHz. It has two main subsystems, a drift chamber trigger (DCT) and an electromagnetic calorimeter trigger (EMT). There is also an instrumented flux return trigger (IFT) which is mainly used for diagnostic purposes.

The DCT looks for short tracks, long tracks and high p_T tracks, while the EMT analyses the summed energy of groups of calorimeter crystals. This information is then passed to the global trigger (GLT) and if the correct criteria are met the event is passed to the L3 trigger.

$B\overline{B}$ events are accepted with 99.9% efficiency. The L1 trigger typically passes events at a rate of 1kHz.

2.9.2 The Level 3 Trigger

The L3 trigger has access to the complete event information. It is required to further reduce the rate to 100Hz, which is the rate that the On-line Prompt Reconstruction system (OPR) can accept data. A detailed reconstruction of the event is made and selection is based on simple track-cluster topologies.

To keep control of high cross-section processes, like Bhabha scattering, pre-scaling factors are applied. The main physics output from the L3 trigger ($B\overline{B}$, $q\overline{q}$, $\tau^+\tau^-$, $\mu^+\mu^-$) is around 13% of the total event rate. QED and two-photon events constitute

11% and calibration samples a further 40%. The rest of the output is comprised of unidentified Bhabha and beam backgrounds, diagnostic information, random triggers and cosmic rays.

2.10 The Data Acquisition System (DAQ)

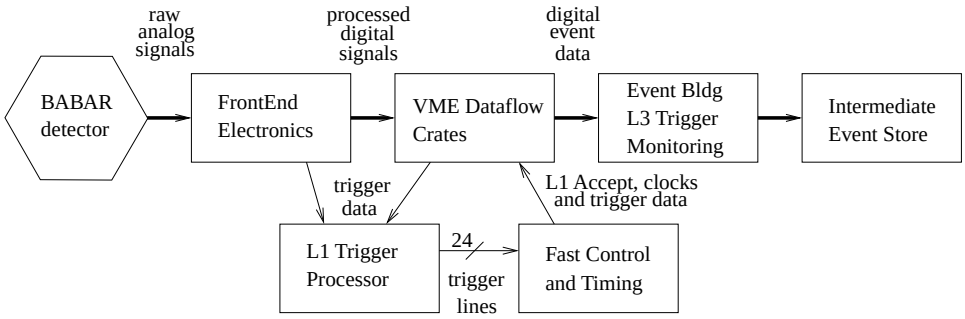

Figure 2.18: *A schematic of the data acquisition process at BABAR.*

The goal of the DAQ system is to transport event data with the minimum of dead time. The front-end electronics take data from each of the detector subsystems and perform some amplification and signal shaping before feeding the data to the VME crates (VME is a computer bus standard, Versa Module Eurocard). These in turn perform some initial high level feature extraction for the L1 trigger. After a L1 "accept" the data are passed through to the L3 trigger. If the L3 criteria are also met the data are sent to be stored on disk.

3

Data Reconstruction & Event Selection

3.1 Introduction

For any analysis it is important to maximise the signal while minimising the background. This chapter focuses on the data sample that is used for the subsequent analysis, how the events are reconstructed and the methods of background suppression.

3.2 Data Sample

The dataset used in this analysis is the aggregate of all data taken at *BABAR* up until the end of running in July 2004. This corresponds to 210.6 fb^{-1} taken at the $\Upsilon(4S)$ resonance, which contains approximately 231.8 million $B\overline{B}$ pairs. There is an additional 21.6 fb^{-1} taken "off-resonance" (40 MeV below $\Upsilon(4S)$) that is used for background studies.

3.2.1 B Counting

Determining the number of $B\overline{B}$ pairs ($N_{B\overline{B}}$) contained within the data sample is essential for making accurate branching fraction measurements. The B counting method looks at the difference between data taken at the $\Upsilon(4S)$ resonance and the off-resonance data. Figure 3.1 shows the increase in multi-hadronic events between off and onresonance. Once any energy dependency of the continuum is taken into account this increase is entirely due to $\Upsilon(4S)$ production. For simplicity (and because it is within errors) it is assumed that the branching fraction for $\Upsilon(4S) \to B\overline{B}$ is 100%.

The total number of B events is given by:

$$N_{B\overline{B}} = N_{\Upsilon(4S)} = \frac{1}{\epsilon_{\Upsilon(4S)}} \left(N_{\text{MH}}(\text{on}) - N_{\text{MH}}(\text{off}) \kappa \frac{N_{\mu\mu}(\text{on})}{N_{\mu\mu}(\text{off})} \right), \tag{3.1}$$

where N_{MH} is the number of multihadron events, $N_{\mu\mu}$ is the number of $\mu^+\mu^-$ events, $\epsilon_{\Upsilon(4S)}$ is the selection efficiency for $\Upsilon(4S)$ from the multihadron cuts, and κ is a constant that takes into account the energy dependence of background events passing the multihadron selection. As selection successfully rejects most background $\kappa \sim 1$.

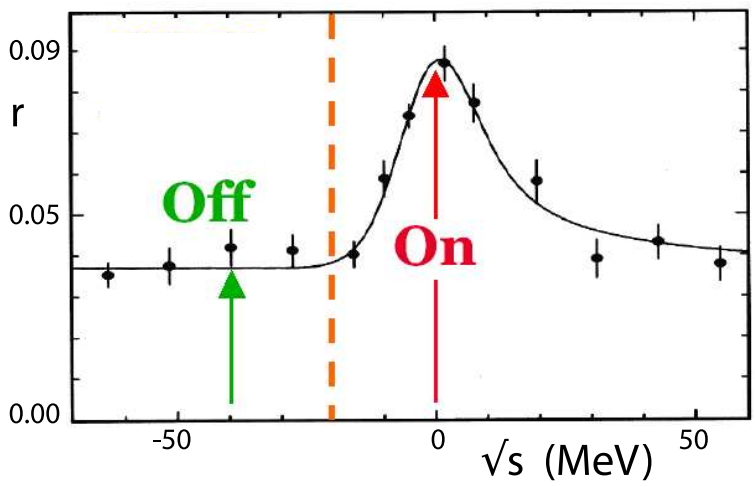

Figure 3.1: *The ratio of multi-hadronic to Bhabha events (r) versus the centre-of-mass energy ($\sqrt{s}$). The energy scale is offset to put the $\Upsilon(4S)$ mass (10580 MeV) at zero. The dashed line shows the $B\overline{B}$ production threshold.*

Using this method the total number of $B\overline{B}$ events in the July 2004 dataset is calculated to be:

$$N_{B\overline{B}} = (231.8 \pm 2.6) \times 10^6 \tag{3.2}$$

3.2.2 Monte Carlo Simulation

Simulated data are used in this analysis for background studies and efficiency calculations.

The first step in simulation is event generation. An overall framework interface program controls the various event generator modules, the most important of which is `EvtGen` [44] which generates $B\overline{B}$ events and hadronic continuum ($q\overline{q}$ where $q = u$, d, s or c) events by calling `JETSET` [45]. Many other generators exist, e.g. a 2-photon generator, a Bhabha generator, but none of these are directly used in this analysis.

As part of the event generation process the beam energies and the x-y co-ordinates of the collision point are smeared with a Gaussian function over ranges of 160 μm and 6 μm respectively. The z distribution covers a much larger range of 1 cm and is taken to be flat.

The generated four-vectors are fed into a detector simulation package. The *BABAR* detector is modelled by a custom interface to the CERN package `Geant4` [46] which simulates the passage of particles through matter. The output from these packages is a series of detector hits, which are then passed on to `SimApp` which simulates the actual detector response and gives output that mimics the real electronic output of the *BABAR* detector, including a full simulation of the trigger. Detector conditions such as dead channels are continually recorded during machine running and then this conditions database is used by `SimApp` to make the final MC as realistic as possible.

At this stage real background events are sometimes overlaid onto the simulated events to model the effect of beam backgrounds. During detector running random triggers are stored for this purpose - their randomness meaning that it is unlikely for them to be signal events.

The final stage in MC production is to run the simulated raw data through the same reconstruction process as is used for real data. The only difference being that MC truth information is also processed.

3.3 Event Reconstruction

Data taking at *BABAR* is split up into *runs* of $\sim$30 minutes. When each run is completed the stored data are sent to be processed by the On-line Prompt Reconstruction (OPR) system. OPR consists of two procedures, firstly Prompt Calibration

(PC) and later Event Reconstruction (ER).

The PC step performs a *rolling* calibration of the detector conditions. It is "rolling" such that conditions from one run are used for the calibration of the subsequent run. This means that if a calibration error is found all data recorded after the fault must be reprocessed in order.

The ER step carries out a full reconstruction of each event using the calibrations from the PC step. If a processing error is found in the ER step only the affected run will need reprocessing.

Both the PC and ER operations produce data quality output in the form of subsystem specific histograms, which are checked both by automated procedures and a more detailed manual approach if problems are found.

3.3.1 Track Finding

Track finding at the OPR level examines initially the tracks found by the L3 trigger in the DCH. The hits associated with these tracks are then fed into a Kalman fit [47] - essentially a least squares fit which takes into account the material and variations in the magnetic field. If any additional DCH hits are found to be consistent with the track they are added in. Further fits are performed looking for tracks that do not originate from the interaction point and for tracks that do not penetrate the entire DCH.

Each track is then extrapolated back to the SVT and any consistent hits are added in. A final search is performed on the SVT data to look for low momentum tracks that didn't reach the DCH.

This analysis uses tracks from *BABAR*'s `GoodTracksLoose` list which contains tracks

that satisfy the following criteria:

- ◇ A minimum transverse momentum of 0.1 GeV/c
- ◇ A maximum momentum of 10.0 GeV/c
- ◇ At least 12 drift chamber hits associated to the track
- ◇ $d_0 < 1.5$ cm
- ◇ $z_0 < 10$ cm

where d_0 is defined as the distance in the x-y plane to the z-axis and z_0 is the distance in the z direction to the origin. Both d_0 and z_0 are defined at the point of closest approach of the track to the z-axis.

3.3.2 Calorimeter Cluster Finding

The first step in looking for calorimeter clusters is to do a scan for crystals with energy deposits of greater than 10 MeV. Any neighbouring crystals with energy greater than 1 MeV are then also added, and similarly the crystals surrounding the cluster are then also examined and added if their energy is high enough. This is repeated until no further adjoining crystals can be found.

To try and discern whether a cluster contains more than one incident particle a "bump" finding algorithm is run. This checks whether the cluster contains more than one peak in the energy distribution. Finally the bumps are matched with any nearby tracks. If the separation distance is within a threshold then the bump and track are considered as the same particle for further reconstruction purposes.

3.3.3 Particle Identification (PID)

Particle identification is the next step in reconstruction. This analysis is concerned with kaon identification and eliminating the possibility of the track coming from a different charged particle.

3.3.3.1 Kaon identification

For kaon identification this analysis uses the *BABAR* SMS kaon selector [48]. It uses data from the Silicon Vertex detector (SVT), Drift Chamber (DCH) and the Cherenkov light detector (DIRC) to determine the probability that each track originated from a kaon. There are five different output modes ranging in efficiency and purity; *very loose*, *loose*, *not a pion*, *tight* and *very tight*. For this analysis the *tight* mode is used. The tight cuts are optimised to keep the misidentifcation level below 5% up to momenta of 4 GeV/c.

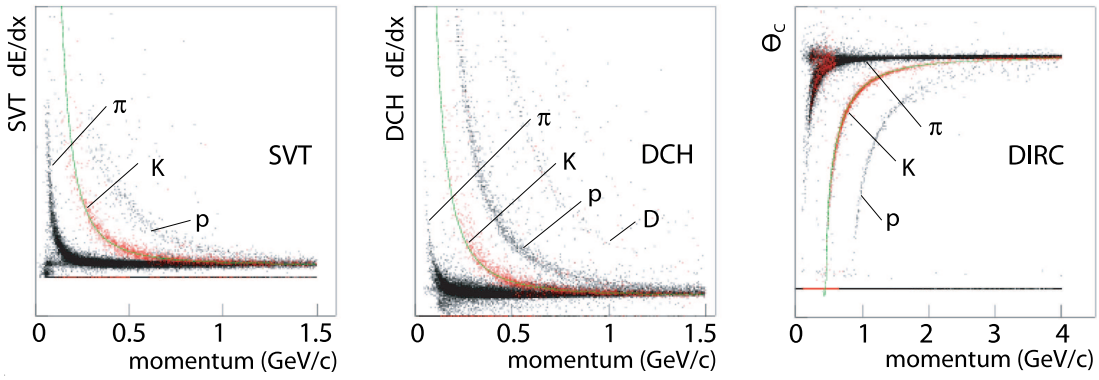

Figure 3.2: *Particle momentum distribution versus dE/dx for the SVT (left) and DCH (middle), and versus Cherenkov angle (θ_C) for the DIRC (right) [48].*

The Bethe-Bloch formula [49] approximates the ionization-energy loss (dE/dx) of particles travelling through matter. Figure 3.2 shows the dE/dx distributions for various particles in the SVT and DCH. Data control samples (e.g. $\phi \to K^+K^-$) are

used to calibrate a Gaussian probability density function (PDF) for each particle type in both the SVT and DCH systems. $\mathrm{d}E/\mathrm{d}x$ measurements give a better than 2σ separation between kaons and pions up to $\sim$0.6 GeV/c in the SVT and up to $\sim$0.7 GeV/c in the DCH. The DCH also gives 2σ separation above 1.5 GeV/c due to the relativistic rise (see Figure 2.10).

The DIRC provides PID for most of the momentum range ($> 0.6\,\mathrm{GeV}/c$). It gives at least 2σ separation up to 4 GeV/c (see Figure 2.13). The distribution of the Cherenkov angle, θ_C, for different particles can be seen in Figure 3.2. θ_C is given by:

$$\theta_C = E/pn, \tag{3.3}$$

where E is the particle energy, p is its momentum and $n = 1.473$ is the refractive index of the DIRC silica bars. The measured angle is compared to expected angles for different particles at the measured momenta.

Low momentum tracks emit few Cherenkov photons making the angle hard to measure. In these cases a likelihood is calculated from the number of photons. The distribution for the number of photons produced by a specific particle path through the DIRC is Poissonian and depends upon the particle mass, charge, momentum and the position of the track in the detector. Gaussian and Poissonian PDFs are calibrated using data control samples.

The identification of charged kaons is complicated by kaon decay (about 20% decay before reaching the DIRC) and interactions with detector material. Figure 3.3 shows DIRC measurements of Monte Carlo kaon tracks. Low momentum kaons show up in the pion band with a large spread. These decayed or interacted before reaching the DIRC. Region D in the diagram shows kaons that have interacted, setting free real protons, before reaching the DIRC.

As an example of how the selector works lets look at the Cherenkov angle distribution

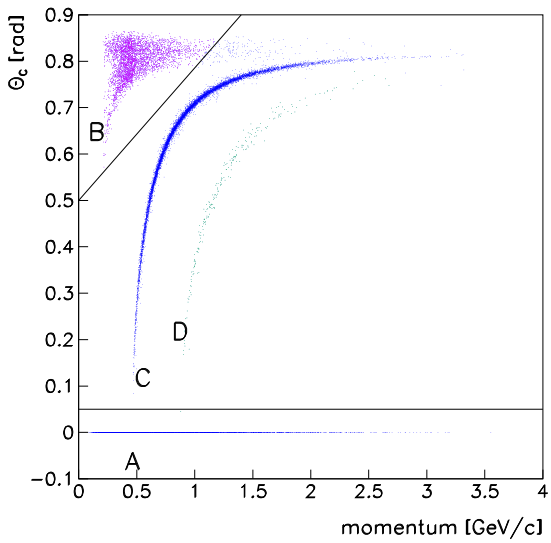

Figure 3.3: *The distribution of Cherenkov angle against momenta for Monte Carlo kaon tracks. Tracks in the triangle B are excluded by the tight selector. Region A shows tracks for which there is no angle information (8% due to solid angle coverage of the DIRC and some due to small numbers of photons or a bad fit) [48].*

for kaons and pions. Assuming that the distributions follow a Gaussian function centred on θ_K or θ_π the pulls are defined:

$$\Delta_i = \frac{\theta_C - \theta_i}{\sigma_{\theta_C}}, \tag{3.4}$$

where $i = K, \pi$. Figure 3.4 shows Δ_K centred at zero and Δ_π shifted to a higher central value, corresponding to the separation between the mean values of θ_K and θ_π. The overlap between the two distributions shows how some kaons will be lost and a fraction of the pions will be misidentified. The likelihood calculation combines the Gaussian distributions from the SVT and DCH with Gaussian and Poissonian distributions from the DIRC. The details of the DIRC likelihood fit can be found in [48].

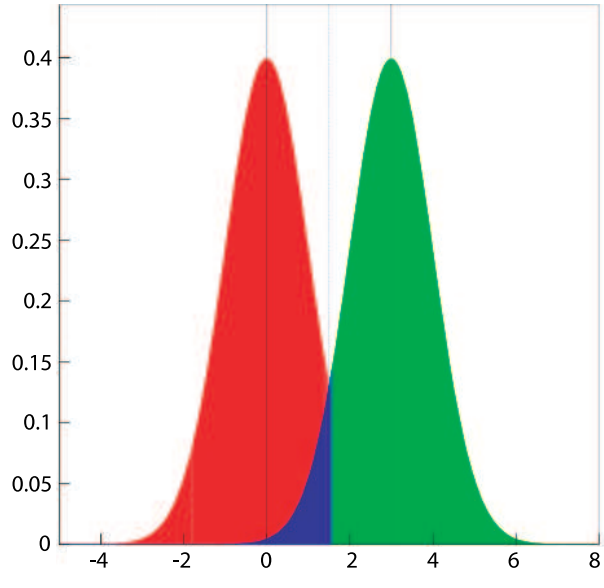

Figure 3.4: *A plot of Δ_K with a cut at $r_\pi = 1$. The kaon distribution is shown in red and the pion distribution is shown in green.*

Table 3.1 shows the minimum requirements for the SMS kaon selector. The tight cuts then add the following requirements:

- ◇ Triangle B, shown in Figure 3.3 is excluded
- ◇ likelihood cut: $l_K > r_\pi l_\pi$ and $l_K > r_p l_p$
- ◇ $r_p = 1$
- ◇ $p < 2.7$ GeV/c: $r_\pi = 1$
- ◇ $p > 2.7$ GeV/c: $r_\pi = 80$
- ◇ $0.5 < p < 0.7$ GeV/c: $r_\pi = 15$

where r_i is the ratio N_K/N_i, and so $r_\pi = 15$ is a tighter cut than $r_\pi = 1$. The performance of the tight SMS kaon selector is shown in Figures 3.5 and 3.6.

Table 3.1: *Kaon selection requirements [48].*

Detector		Momentum range	Requirements
SVT	$\mathrm{d}E/\mathrm{d}x$	$0.025 < p < 0.7$ GeV/c $p > 1.5$ GeV/c	> 3 $\mathrm{d}E/\mathrm{d}x$ sample hits
DCH	$\mathrm{d}E/\mathrm{d}x$	$0.090 < p < 0.7$ GeV/c $p > 1.5$ GeV/c	> 10 $\mathrm{d}E/\mathrm{d}x$ sample hits
DIRC	N(photons) θ_C	$0.6 < p < 10$ GeV/c	expected number of photons for $e^- > 0$

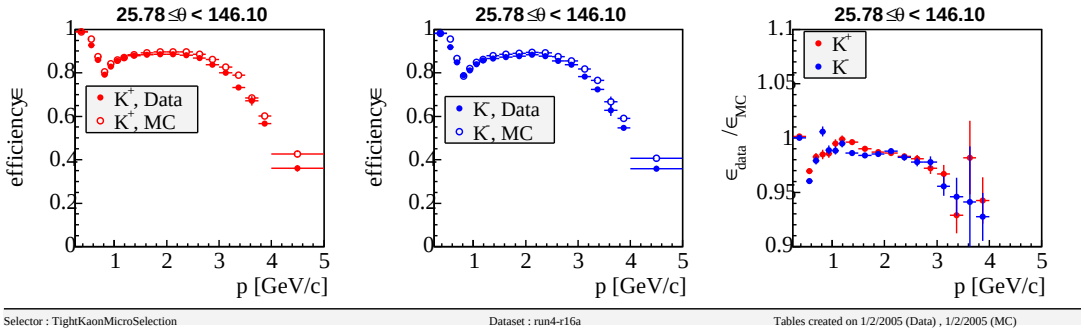

Figure 3.5: *Kaon selection efficiency versus momentum for data and Monte Carlo using the tight kaon selector [50].*

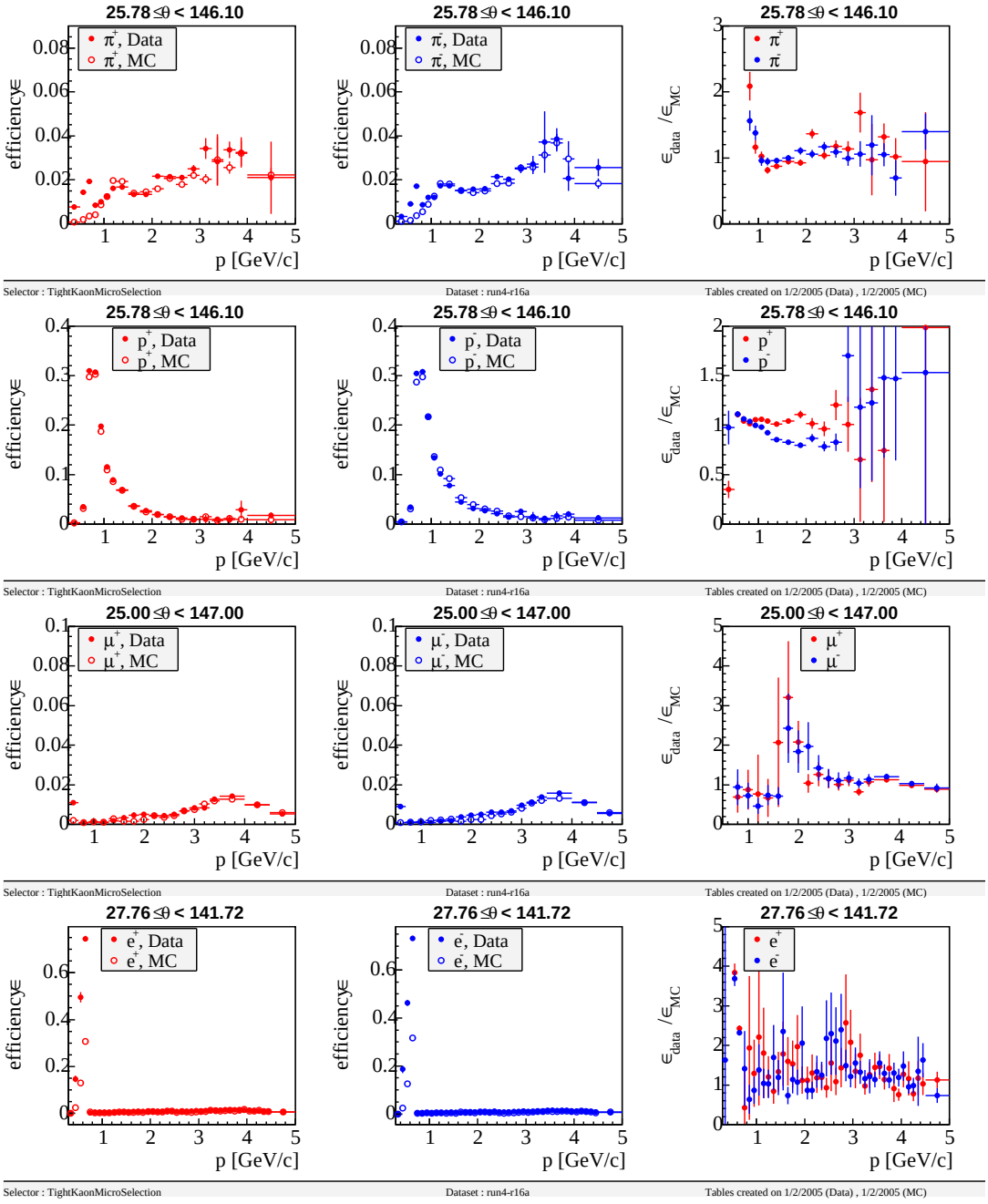

Figure 3.6: *Particle mis-ID selection efficiency versus momentum for data and Monte Carlo using the tight kaon selector. Top row: pion selection, second row: proton selection, third row: muon selection, bottom row: electron selection [50].*

3.3.3.2 Electron Identification

Information from the EMC, DCH and DIRC is used when reconstructing electrons. The EMC measures the energy and shape of the electromagnetic shower. The DCH provides $\mathrm{d}E/\mathrm{d}x$ information and the DIRC gives Cerenkov angle measurements, although they are only used below $1.5\,\mathrm{GeV}/c$.

3.4 Discriminating Variables

3.4.1 The ΔE and m_{ES} variables

Operating at the $\Upsilon(4S)$ resonance and requiring that it decays to $B\overline{B}$ gives certain constraints that can be exploited to eliminate background events. ΔE is defined:

$$\Delta E = E_B^* - E_{beam}^* \tag{3.5}$$

where $E_{beam}^* = \sqrt{s}/2$ and s is the square of the centre of mass energy in and E_B^* is the reconstructed energy of the B candidate, again measured in the CM frame. m_{ES} is defined:

$$m_{\mathrm{ES}} = \sqrt{E_{beam}^{*2} - \vec{p}_B^{*2}} \tag{3.6}$$

where $\vec{p}_B^*$ is the momentum of the B candidate in the CM frame.

An advantage of using these two variables is that they are almost uncorrelated. Also they are less affected by detector resolution than comparable variables such as the

reconstructed mass of the B candidate. The advantages are discussed at length in [51].

For correctly reconstructed B mesons $m_{\rm ES}$ forms a peak at the B mass (5.279 GeV) and ΔE forms a peak about zero. In both cases the large background from hadronic continuum events should be non-peaking. Any background that originates from $B\overline{B}$ events may form well reconstructed B's and so will peak in $m_{\rm ES}$ – this is a small effect.

3.4.2 $\cos\theta_{Thr}$

Thrust is a topological variable. The thrust axis is the line along which the longitudinal momenta of a collection of particles is maximised [52]. $B\overline{B}$ events are generally isotropic across the detector, whereas $q\overline{q}$ events tend to form two back-to-back jets. θ_{Thr} is defined as the angle between the thrust axis of the reconstructed B candidate and the thrust axis of the rest of the event (ROE). Taking the cosine of this gives a variable that is flat for data and peaking at ±1 for $q\overline{q}$ background, see Figure 3.7.

3.4.3 Fisher Discriminant ($\mathcal{F}$)

A Fisher discriminant [53] combines many different variables, that on their own do not have much discriminating power, to form one variable with much greater distinguishing power. Another method to achieve this would be to use a neural net but it had no greater distinguishing power in this analysis. The Fisher discriminant can be defined as:

$$\mathcal{F} = \sum_i a_i x_i = \vec{a}^T \vec{x}, \tag{3.7}$$

where x_i are some discriminating variables and a_i are coefficients chosen to maximise

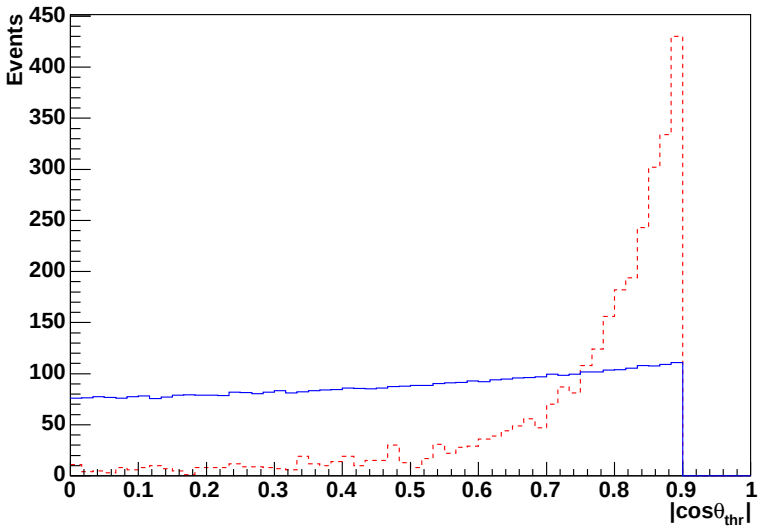

Figure 3.7: *The $|\cos\theta_{Thr}|$ distribution for $B^{\pm} \to K^{\pm}K^{\mp}K^{\pm}$ nonresonant MC (blue/solid line) and off-peak data (red/dashed line). The samples have been normalised to the same number of events. A pre-selection cut at 0.9 is applied to both sets of data.*

the separation between signal and background events. In this case the variables used are:

- L_0 and L_2, two variables based on Legendre polynomials. They are defined as:

$$L_0 = \sum_i^{\text{ROE}} p_i \tag{3.8}$$

$$L_2 = \sum_i^{\text{ROE}} p_i \times \frac{1}{2}(3\cos^2(\theta_i) - 1) \tag{3.9}$$

  where p_i is the momentum and θ_i is the polar angle of the track or cluster measured relative to the thrust axis of the B candidate in the CM frame.

- $\cos\theta_{Bmom}$, where θ_{Bmom} is the angle between the sum of the B candidate momentum and the beam in the CM frame.

- ◇ $\cos\theta_{Bthr}$, where θ_{Bthr} is the angle between the B candidate thrust axis and the beam in the CM frame.

- ◇ `TFlv` is the output of the B tagging algorithm [54]. By studying particles from the ROE, which is assumed to be a second B event, the `TFlv` variable estimates the flavour of the B candidate. A value towards 1 indicates a high probability of correct flavour tagging, whereas a value near 0 indicates that no decision could be made. When looking at non-B decays it gives noticeably different results in these two areas.

For distributions of all the variables and the Fisher discriminant see Figure 3.8.

3.5 Event Selection

The full dataset goes through three stages of filtering before the reduced final dataset is established. Using three stages reduces repetition of work by different analyses, for example a $B^{\pm} \to \pi^{\pm}\pi^{\mp}\pi^{\pm}$ analysis can use the same data after two stages as $B^{\pm} \to K^{\pm}K^{\mp}K^{\pm}$ analyses.

The selection for the first stage, *skimming*, is determined by the *BABAR* 3-Body Charmless working group. It is designed to be generic to many 3-body decays. The skims are run centrally by the collaboration.

The second stage uses `NonCharm3BodyUser` [55], a package built upon the *BABAR* framework, to further filter the skims into `Root` [56] ntuples. This stage is generic to $B^{\pm} \to h^{\pm}h^{\mp}h^{\pm}$ analyses (where $h = \pi$ or K) and is run in batch jobs by members of the 3-Body Charmless group.

The final stage uses bespoke code based on the `CharmlessFitter` package to single

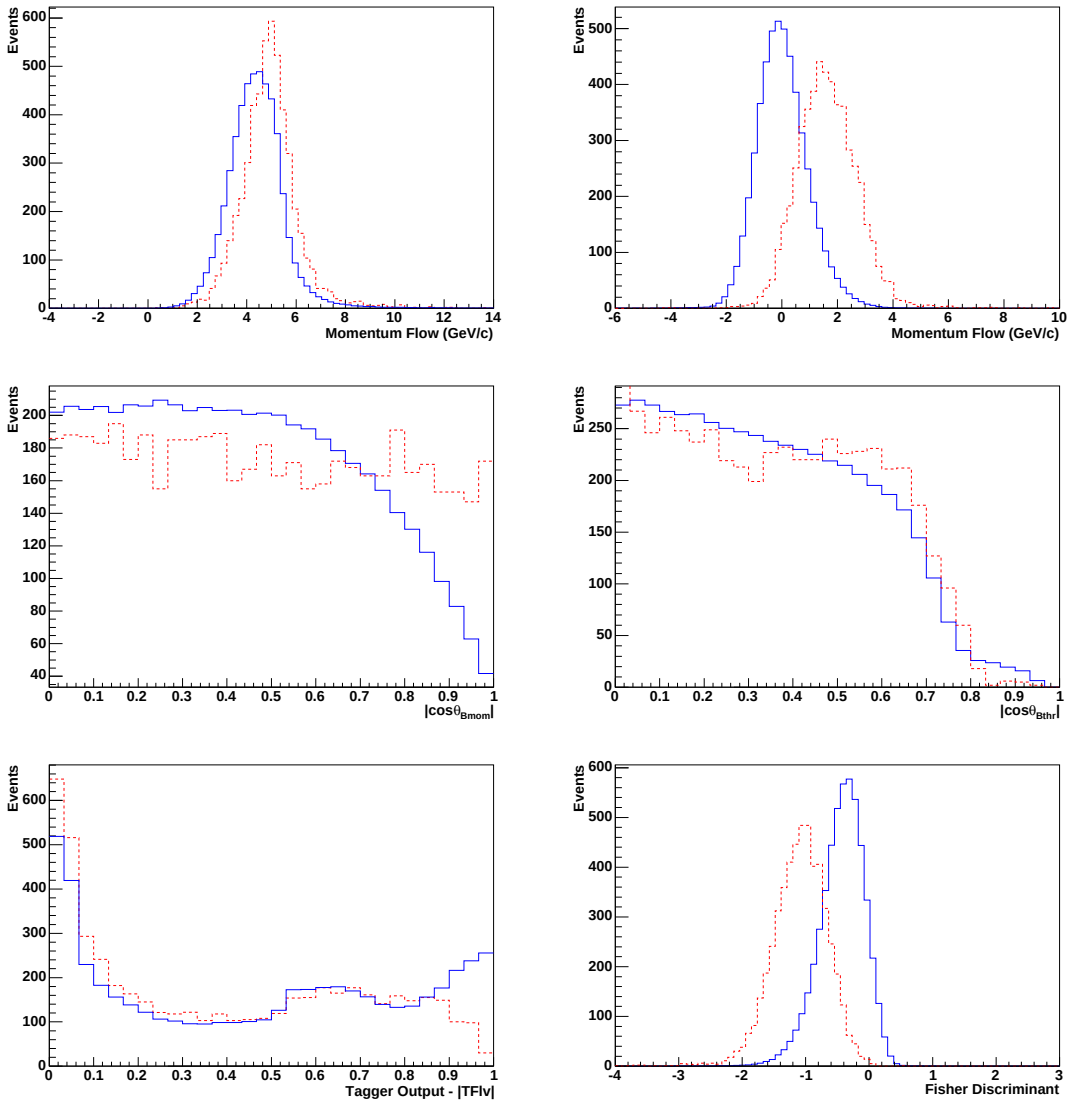

Figure 3.8: *The distributions of the Fisher discriminant and its component parts. Top left: L0. Top right: L2. Middle left:* $\cos\theta_{Bmom}$*. Middle right:* $\cos\theta_{Bthr}$*. Bottom left:* `TFlv`*. Bottom right: the Fisher discriminant. The blue/solid line shows* $B^{\pm} \to K^{\pm}K^{\mp}K^{\pm}$ *MC and the red/dashed line shows off-peak data. The samples have been normalised to the same number of events.*

out $B^{\pm} \to K^{\pm}K^{\mp}K^{\pm}$ candidates and produce reduced `Root` ntuples.

3.5.1 Skimming

The first level of analysis skims the full dataset looking for B candidates formed from three charged tracks. The tracks are taken from the `GoodTracksLoose` list as described in section 3.3.1. The full list of criteria that must be met by the B candidate is:

- ◇ The total charge of the B candidate is required to be ± 1.
- ◇ The total number of tracks in the event is required to be ≥ 4. This ensures that there is at least one track from the other B in the event.
- ◇ The total energy of the event is required to be $< 20\,\text{GeV}$. This is a basic sanity check (the centre-of-mass energy is only $10.58\,\text{GeV}$), and removes less than 1% of events.
- ◇ m_{ES} is required to be within $0.1\,\text{GeV}/c^2$ of the beam energy ($5.29\,\text{GeV}/c^2$).
- ◇ ΔE is required to have an absolute value less than $0.45\,\text{GeV}$.

Skims are defined by each of the different working groups in *BABAR* to be run centrally. This reduces the repetition of similar jobs for each different analysis, e.g. a $B^{\pm} \to \pi^{\pm}\pi^{\mp}\pi^{\pm}$ analysis uses the same skim as this $B^{\pm} \to K^{\pm}K^{\mp}K^{\pm}$ analysis. To this end ΔE is actually calculated for all possible final state combinations ($\pi^{\pm}\pi^{\mp}\pi^{\pm}$, $K^{\pm}\pi^{\mp}\pi^{\pm}$, $K^{\pm}K^{\mp}\pi^{\pm}$, $K^{\pm}K^{\mp}K^{\pm}$ etc.) and the event passed if any combination passes the above ΔE cut. The 3-Body Charmless working group defined the above skim.

3.5.2 NonCharm3BodyUser ntuple production

`NonCharm3BodyUser` performs the following tasks:

- ◇ Vertexing of the B candidates after which ΔE and $m_{\rm ES}$ are recalculated.
- ◇ Vertexing then re-done with a B mass constraint applied – the tracks are varied within their errors and the event is retained if a B-mass constrained vertex is found.
- ◇ Particle ID selectors are run.
- ◇ Calculation of $\cos\theta_{Thr}$, L_0, L_2, $\cos\theta_{Bmom}$, $\cos\theta_{Bthr}$ and `TFlv`.
- ◇ Calculation of Dalitz plot quantities such as the invariant mass of the different particle combinations.
- ◇ $|\Delta E|$ is required to be less than 0.35 GeV.
- ◇ $|\cos\theta_{Thr}|$ is required to be less than 0.95.

This stage is again used by multiple analyses and so the same care is taken with the ΔE cut as is described in Section 3.5.1.

3.5.3 Final Selection

The selection criteria for the final reduced ntuples are:

- ◇ Each candidate must have a valid kinematic fit for a $K^{\pm}K^{\mp}K^{\pm}$ final state.
- ◇ Each kaon candidate track must pass the SMSKaonSelector in tight mode.

- ◇ All tracks must fail the standard *BABAR* electron selector.
- ◇ $|\cos\theta_{Thr}|$ is required to be below 0.9.
- ◇ The value of the Fisher discriminant must be above -0.71.
- ◇ $m_{\rm ES}$ is required to be below the beam energy ($5.29\,{\rm GeV}/c^2$).
- ◇ The value of ΔE must be between -0.0683 and 0.0517 GeV. This is chosen by imposing a 3σ (0.06 GeV) cut on the distribution. However a study of the ΔE distribution in the control channel, $B^+ \to \overline{D}^0\pi^+$, showed a shift of $-8.3\,{\rm MeV}$ between data and MC. Therefore the selection window must be shifted by this amount.
- ◇ The requirement of a single candidate per event is then imposed. If multiple candidates exist, then one is chosen randomly so as not to bias the $m_{\rm ES}$ and Dalitz plot distributions.
- ◇ The $B\overline{B}$ background channel, $B^+ \to \overline{D}^0K^+$, $\overline{D}^0 \to K^+K^-$, is also vetoed at this stage, i.e. data in the region $1.80 < m_{K^+K^-} < 1.90\,{\rm GeV}/c^2$ is discarded.

3.5.3.1 Definition of Fitting Regions

The ΔE-$m_{\rm ES}$ Signal Strip defined above is further broken down into a Signal Box and a Sideband which is used to characterise the background. The entire window is used to determine the fractions of $q\overline{q}$ and $B\overline{B}$ background within the Signal Box. The $m_{\rm ES}$ cuts for each region are:

- ◇ Signal Strip: $5.20 < m_{\rm ES} < 5.29\,{\rm GeV}/c^2$.
- ◇ Signal Box: $5.271 < m_{\rm ES} < 5.287\,{\rm GeV}/c^2$.
- ◇ Sideband: $5.20 < m_{\rm ES} < 5.26\,{\rm GeV}/c^2$.

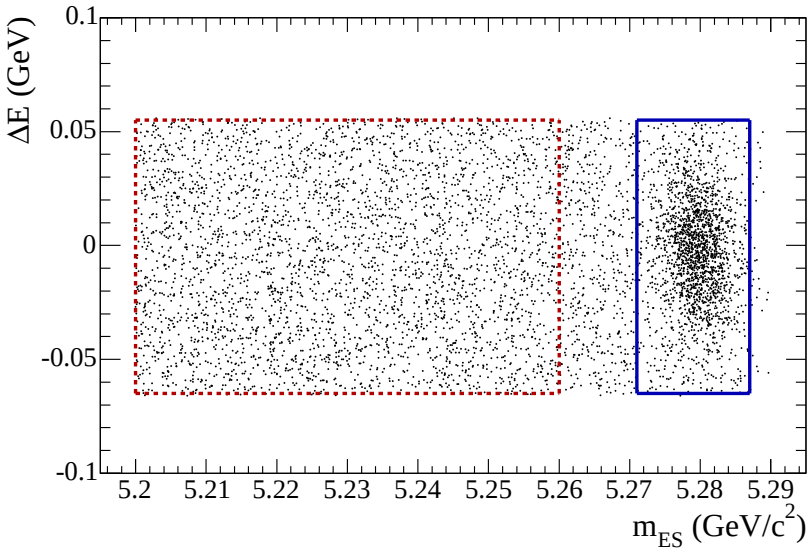

Figure 3.9: *ΔE-$m_{\rm ES}$ plane, showing Signal Strip (all events), Signal Box (solid blue line) and the Sideband (dashed red line).*

This can be seen in Figure 3.9.

3.5.3.2 Selection Optimisation

The final selection for this analysis is broadly based upon the earlier $B^{\pm} \to h^{\pm}h^{\mp}h^{\pm}$ branching fraction analysis [17]. A different Fisher discriminant definition is used, however, meaning that the cuts had to be re-optimised. $\cos\theta_{Thr}$ and the Fisher discriminant are highly correlated and so cuts on them must be optimised together.

$\cos\theta_{Thr}$ is varied, and for each value the Fisher co-efficients are recalculated. The signal significance $S/\sqrt{S+B}$ is then calculated for a range of Fisher values, see Figure 3.10. The dataset used in this study was a sample of $B^{\pm} \to K^{\pm}K^{\mp}K^{\pm}$ nonresonant MC, normalised using the world average [9] for the inclusive branching fraction. The background used included both the off-peak dataset and on-peak data from an upper sideband defined as:

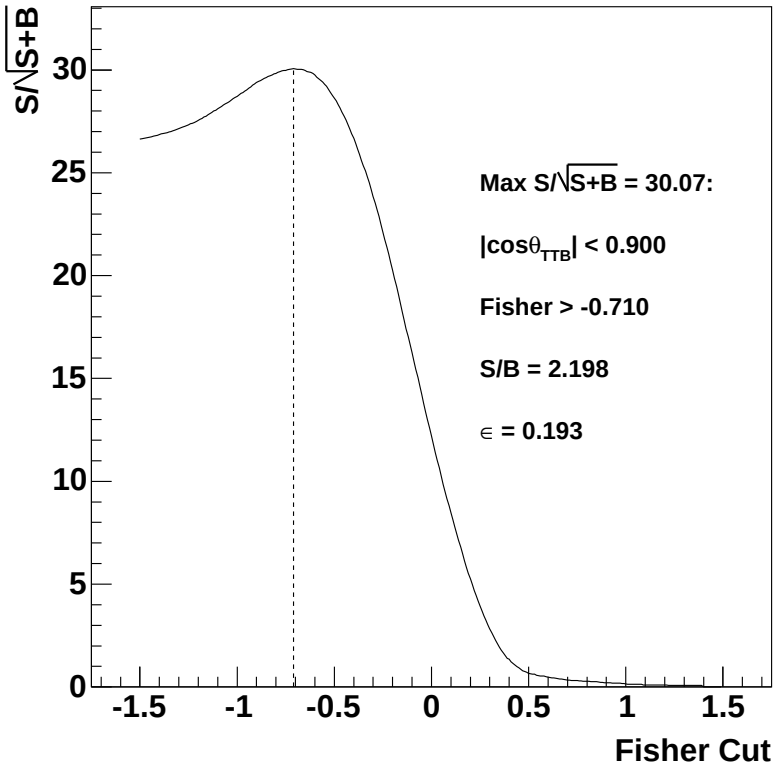

Figure 3.10: *Signal significance as a function of Fisher selection value [57].*

- $5.20 < m_{\rm ES} < 5.26\,{\rm GeV}/c^2$.
- $0.1 < \Delta E < 0.3\,{\rm GeV}$,

but otherwise using the same criteria as laid out in Section 3.5.3.

3.5.3.3 Final Efficiencies

A summary of the selection requirements and their efficiencies for $B^\pm \to K^\pm K^\mp K^\pm$ nonresonant MC are shown in Table 3.2.

Cut	**Signal MC Selection Efficiency**
Reconstruction and preselection	0.640
Valid $K^{\pm}K^{\mp}K^{\pm}$ vertex fit hypothesis	0.993
Kaon PID requirements	0.424
Electron PID veto	0.996
$\lvert\cos\theta_{Thr}\rvert < 0.9$	0.866
$\mathcal{F} > -0.71$	0.895
$5.20 < m_{\rm ES} < 5.29\,{\rm GeV}/c^2$	0.994
$-0.0683 < \Delta E < 0.0517\,{\rm GeV}$	0.912
$\overline{D}^0$ veto, $1.80 < m_{K^+K^-} < 1.90\,{\rm GeV}/c^2$	0.951
Signal Strip: $5.20 < m_{\rm ES} < 5.29\,{\rm GeV}/c^2$	0.195 $\pm 3.41 \times 10^{-4}$
Signal Box: $5.271 < m_{\rm ES} < 5.287\,{\rm GeV}/c^2$	0.191 $\pm 3.39 \times 10^{-4}$
Sideband: $5.20 < m_{\rm ES} < 5.26\,{\rm GeV}/c^2$	2.31×10^{-3} $\pm 4.27 \times 10^{-5}$

Table 3.2: *Summary of average selection efficiencies. The Monte Carlo study used 1.263 million $B^{\pm} \to K^{\pm}K^{\mp}K^{\pm}$ signal events. The total efficiencies are the total number of events passing the selection criteria divided by the total number of input/generated events*

4

Analysis Method

4.1 Introduction

This chapter details how the dataset, as described in the previous chapter, is analysed. Topics covered include the specifics of the Dalitz fit, efficiency modelling, background suppression techniques and details of the determination of the signal model.

4.2 The Dalitz Plot Fit

For Dalitz plot theory see Section 1.4.

A `Root`-based package named `Laura++` [58], [59] was developed for the analysis of charmless $B^{\pm} \to h^{\pm}h^{\mp}h^{\pm}$ Dalitz plots (where $h = \pi$ or K). `Laura++` takes input models for the signal, background and efficiency and then attempts to maximise a likelihood function by floating the magnitudes and phases of the signal probability density function in a fit. In reality the *negative* natural logarithm of the likelihood function is *minimised* by two `Minuit` [60] fits, the first finding a quick estimate and the second to produce a more precise fit. A third `Minuit` routine is then used to calculate any possible asymmetric errors. The function to be minimised is:

$$-\ln \mathcal{L}_{Tot} = -\sum_{n=1}^{N_{Tot}} \ln \mathcal{L}_n. \tag{4.1}$$

where $\mathcal{L}_{Tot}$ is the total likelihood, N_{Tot} is the total number of events and $\mathcal{L}_n$ is the per event likelihood. The unbinned per event likelihood function has the form:

$$\begin{aligned} \mathcal{L}(x,y) &= (1 - f_{q\bar{q}} - f_{B\bar{B}}) \frac{|\sum_{j=1}^{N} c_j e^{i\theta_j} F_j(x,y)|^2 \epsilon(x,y)}{\int\int_{DP} |\sum_{j=1}^{N} c_j e^{i\theta_j} F_j(x,y)|^2 \epsilon(x,y)\, dxdy} \\ &+ f_{q\bar{q}} \frac{Q(x,y)}{\int\int_{DP} Q(x,y)\, dxdy} \\ &+ f_{B\bar{B}} \frac{B(x,y)}{\int\int_{DP} B(x,y)\, dxdy} \end{aligned} \tag{4.2}$$

where

- $x = m^2_{13}(K^+K^-)$ and $y = m^2_{23}(K^+K^-)$ are the invariant mass-squared pairs of the two possible charge-zero combinations of the three kaons.
- N is the number of resonant and nonresonant signal components in the plot.
- F_j is the dynamical part of the amplitude (the lineshape) of the component j.
- c_j and θ_j are the magnitude and phase of the component j.

- ◇ $\epsilon(x, y)$ is the reconstruction efficiency across the Dalitz plot.
- ◇ $Q(x, y)$ is the distribution of $q\overline{q}$ continuum background across the Dalitz plot.
- ◇ $B(x, y)$ is the distribution of $B\overline{B}$ background across the Dalitz plot.
- ◇ $f_{q\overline{q}}$ and $f_{B\overline{B}}$ are the fractions of $q\overline{q}$ and $B\overline{B}$ background events.

As there are two identical kaons in the final state the dynamical amplitudes, signal efficiency and background distributions are symmetrised between x and y. Figure 4.1 shows the difference between a symmetrised and a randomly unsymmetrised Dalitz plot.

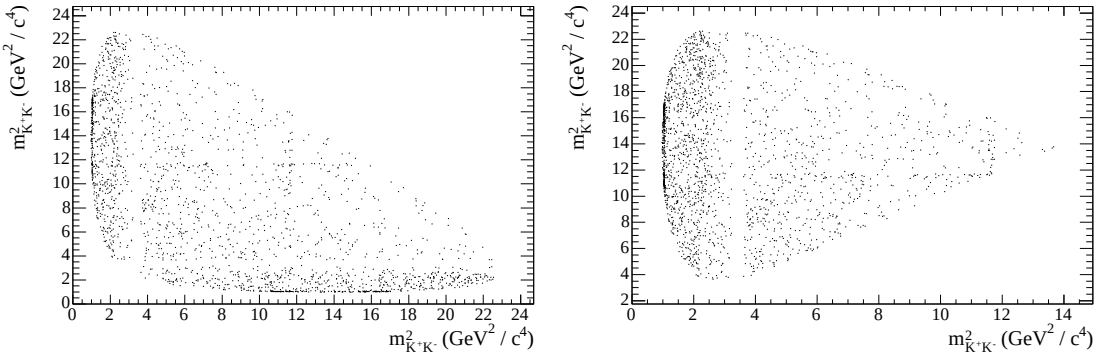

Figure 4.1: *The Dalitz plot for the combined B^+ and B^- data sample. As the axes are identical the Dalitz plot should be folded about $x = y$, as seen in the right-hand plot. This also increases the statistics in the resonance bands.*

Floating parameters in the fit are limited to the magnitudes and phases, c_j and θ_j. The fit is only sensitive to the relative magnitudes and phases between the components, and so, to allow all of our fit results to be easily comparable with each other, the coefficients of the nonresonant component are fixed in the fit to be $c_j = 1.0$ and $\theta_j = 0.0$.

All background related parameters are held static in the fit using numbers and models from detailed background studies, see Section 4.5. The efficiency model is

also pre-determined from MC studies, see Section 4.3.

The lineshapes are normalised over the Dalitz plot such that

$$\int\int_{DP} F_j(x,y)dxdy = 1. \tag{4.3}$$

For the resonant contributions F_j is given by the product of the invariant mass and angular distribution probabilities,

$$F_j = R_j(m) \times T_j(\cos\theta), \tag{4.4}$$

where R_j is the resonance mass term (e.g. Breit-Wigner) and T_j is the angular probability distribution. The Zemach tensor formalism [61], [62] is used for the angular distributions,

- ◇ Spin 0 particle: $T_j(\cos\theta_H) = 1$
- ◇ Spin 1 particle: $T_j(\cos\theta_H) = -2\vec{p}\cdot\vec{q}$
- ◇ Spin 2 particle: $T_j(\cos\theta_H) = \frac{4}{3}\left[3(\vec{p}\cdot\vec{q})^2 - (|\vec{p}||\vec{q}|)^2\right]$

where $\vec{p}$ is the momentum of the resonance and $\vec{q}$ is the momentum of the daughter kaon with the same charge as the resonance. Both are measured in the rest frame of the resonance.

4.2.1 Fit Fractions

It is useful to quote the results as "fit fractions" rather than magnitudes and phases because separate analyses may use different amplitude, phase and normalisation conventions. A fit fraction quantifies how much of the Dalitz plot is made up by a component. These fractions do not necessarily sum to unity however, due to interference between components. The fit fraction of a component j is given by:

$$(\text{Fit Fraction})_j = \frac{\int |c_j e^{i\theta_j} F_j(x,y)|^2 dxdy}{\int |\sum_j c_j e^{i\theta_j} F_j(x,y)|^2 dxdy}. \tag{4.5}$$

4.2.2 *CP* Asymmetry

The *CP* asymmetry of the total rate is found by measuring the number of signal events in the B^+ and B^- samples. This is done by fitting to the $m_{\rm ES}$ distribution of each sample while taking into account knowledge of the signal and background $m_{\rm ES}$ distributions (see Section 4.5.3). The asymmetry is then given by:

$$A = \frac{N^-_{sig} - N^+_{sig}}{N^-_{sig} + N^+_{sig}}, \tag{4.6}$$

where N^-_{sig} and N^+_{sig} are the the number of signal events in the B^- and B^+ samples respectively.

To measure the *CP* asymmetry for each resonance the B^+ and B^- Dalitz plots are fitted separately. The fit fractions from the two fits are then combined with the total numbers of signal events such that:

$$A^{FF}_j = \frac{FF^-_j N^-_{sig} - FF^+_j N^+_{sig}}{FF^-_j N^-_{sig} + FF^+_j N^+_{sig}}, \tag{4.7}$$

where FF^-_j and FF^+_j are the fit fractions for a resonance j in the B^- and B^+ datasets respectively.

4.3 Efficiency Modelling

The signal reconstruction efficiency is the fraction of signal events that pass the data reconstruction and event selection as detailed in Chapter 3. The average reconstruction efficiency for $B^\pm \to K^\pm K^\mp K^\pm$ events as given by Monte Carlo (MC) is shown

in Table 3.2. However the efficiency distribution across the Dalitz plot need not be flat.

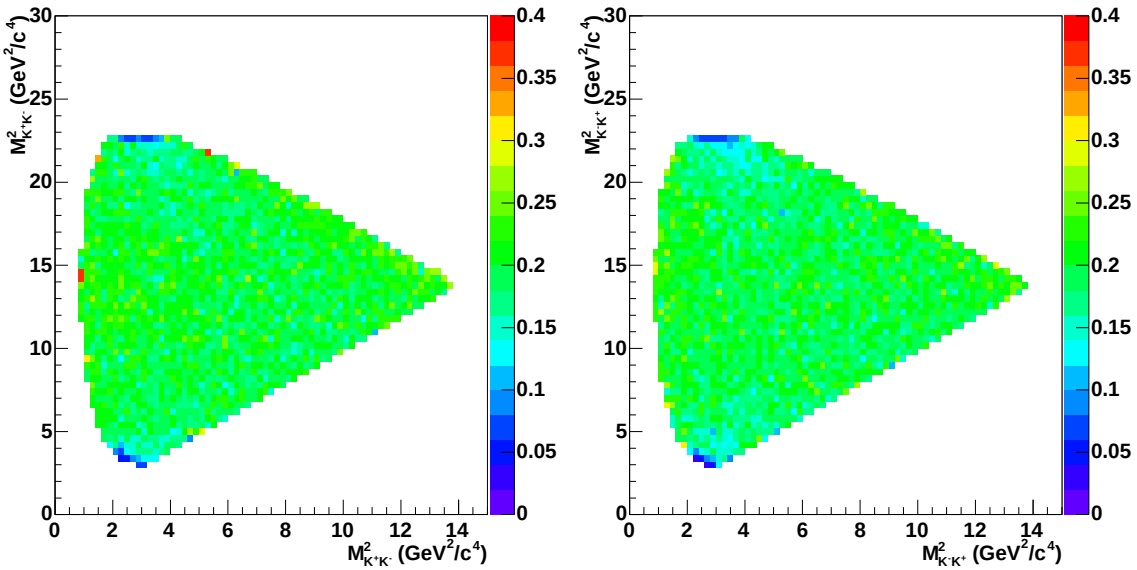

Figure 4.2: *Efficiency distribution across the Dalitz plot. The left hand plot shows B^+ events, the right hand plot shows B^- events [57].*

The variation of the efficiency across the Dalitz plot is studied using a sample of 1.314 million $B^\pm \to K^\pm K^\mp K^\pm$ MC events which are generated to have a flat distribution across phase space. These events are passed through the reconstruction software and then must pass the analysis selection criteria. The D^0 veto is not applied however, to ensure that the whole Dalitz plot is populated. 260,191 events are selected in the Signal Box region.

A further constraint is then applied where each event must be "truth matched". A truth matched event is a real, correctly reconstructed $B^\pm \to K^\pm K^\mp K^\pm$ event, i.e. the three kaons must originate from the same B meson and they must be the only daughters of the decay. This reduces the dataset to 258,572 events.

These events are then used to populate a numerator Dalitz plot histogram. At this stage efficiency corrections taking into account the reconstruction differences between MC and real data are applied. MC truth information from the complete dataset of 1.314 million events is used to plot a denominator histogram and the quotient then gives the efficiency distribution to be used in the Dalitz fit. A comparison of the B^+ and B^- distributions can be seen in Figure 4.2.

As both distributions are consistent the histograms are merged to give greater statistical accuracy. Some bins around the edge of the plot have large errors caused by low bin content. This effect is avoided by merging the lowly populated bin with a neighbouring bin in both the numerator and denominator histograms and then recalculating the efficiency for the larger sized bin. The final efficiency histogram can be seen in Figure 4.3.

To correct for any further statistical fluctuations in the plot linear interpolation is performed by `Laura++`.

The distribution is essentially flat, but with a drop off toward the corners. These regions contain events with one low energy kaon, making them more challenging to reconstruct.

4.3.1 Self Cross-feed

Self Cross-feed (SCF) is when one or more of the signal kaons is interchanged during reconstruction with particles from the decay of the other B meson in the event. This corresponds to the non-truth matched events from the efficiency study, see Section 4.3, which is a dataset of 6,255 events. In the Signal Box this is further reduced to 1,619 or 0.6% of all reconstructed $B^\pm \to K^\pm K^\mp K^\pm$ decays.

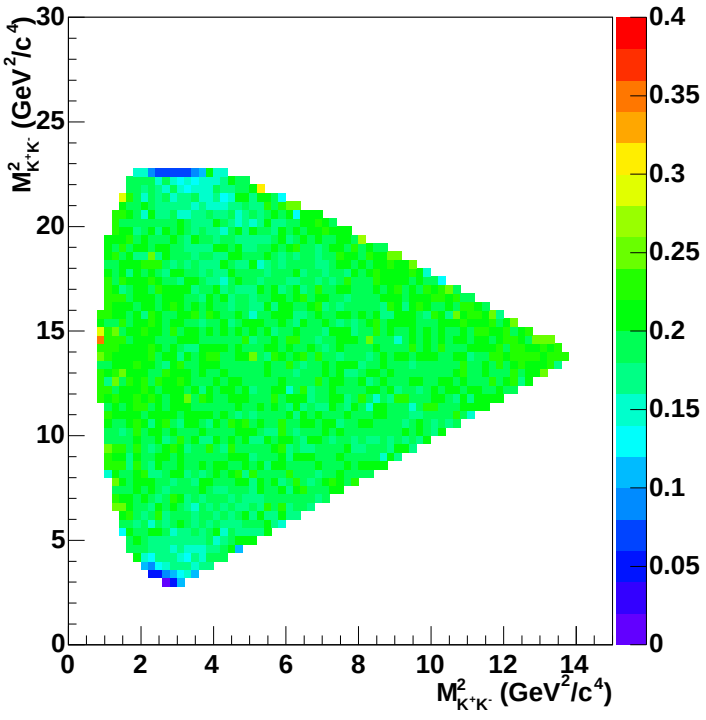

Figure 4.3: *Efficiency distribution, corrected for low statistics bins [57].*

Figure 4.4 shows the Dalitz plot distribution of SCF events for B^+ and B^- to be the same. As the fraction is very small and concentrated in the extreme corners of the Dalitz plot the effect of SCF is neglected in the fit.

4.4 Event Migration Effects

Migration is the movement of an event from its true position to its reconstructed position in the Dalitz plot. If migration moves the events far it could blur resonance shapes and limit the accuracy of the fit.

A sample of 1.314 million $B^\pm \to K^\pm K^\mp K^\pm$ flat nonresonant MC events is used to

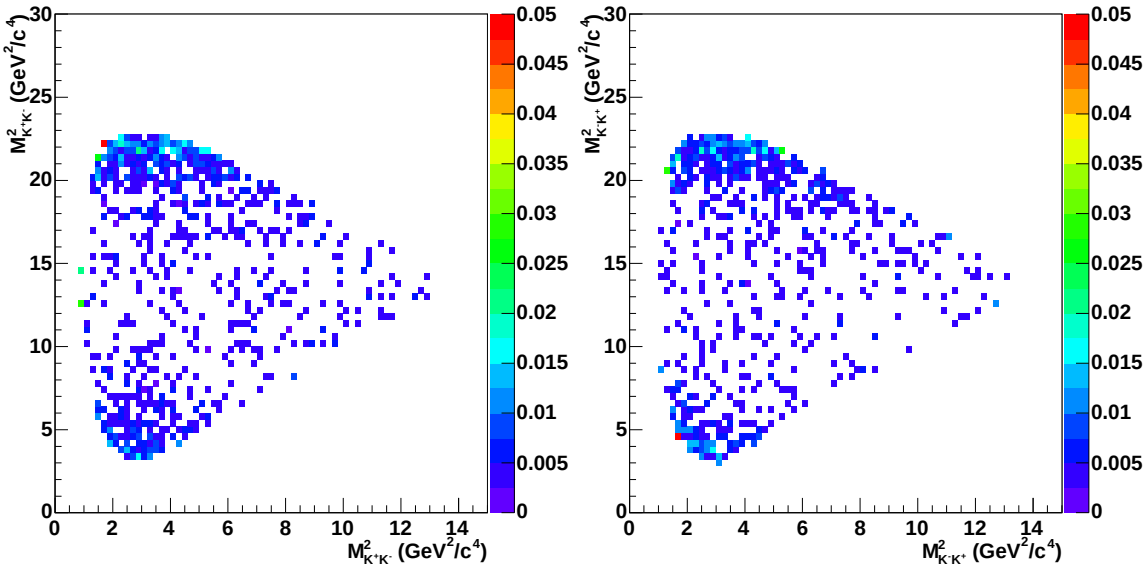

Figure 4.4: *Dalitz distribution of SCF events. The left hand plot shows B^+ events and the right hand plot shows B^- events [57]. The colour scale shows the number of SCF events per bin as a fraction of the total events in each bin.*

study migration effects. The difference between the MC truth and reconstructed positions gives the magnitude of the migration, as defined:

$$d_{migration} = \sqrt{(m_{13}^{truth} - m_{13}^{reco})^2 + (m_{23}^{truth} - m_{23}^{reco})^2} \tag{4.8}$$

The migration distance is then plotted in two histograms, an "outflow" histogram plots events at their MC truth positions to show from where events move, and an "inflow" histogram plots the events at their reconstructed positions, showing where events move to.

Figure 4.5 shows both inflow and outflow histograms to be uniform in nature, with the average migration being very small in magnitude. As such migration effects are neglected in the amplitude fit.

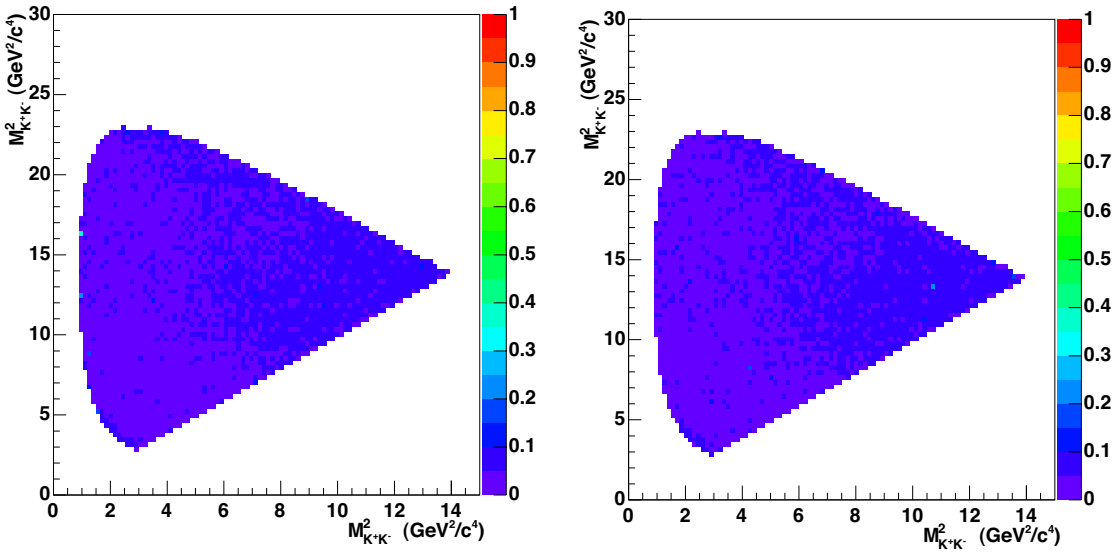

Figure 4.5: *Migration of events within the Dalitz plot; the left hand plot shows inflow, the right hand plot shows outflow. The colour scale shows* $\bar{d}_{migration}$ *in units of* GeV^2/c^4 *[57].*

4.5 Background Estimation

There are two distinct types of background to be modelled, light quark $q\overline{q}$ background and $B\overline{B}$ background. This section discusses both types in detail and also the determination of the signal to background ratio.

4.5.1 $q\overline{q}$ Background

Almost three times more $q\overline{q}$ events are produced at *BABAR* than $B\overline{B}$ events. These events can produce three kaons (or particles merely identified as kaons), which can then be misreconstructed as signal $B^{\pm} \to K^{\pm}K^{\mp}K^{\pm}$ events. Continuum $q\overline{q}$ events provide the greatest source of background for this analysis.

$B\overline{B}$ events are isotropic in shape, whereas $q\overline{q}$ have a collimated back-to-back structure. Exploiting this topology difference and also using constraints given by operating at the $\Upsilon(4S)$ resonance (cuts on ΔE and $m_{\rm ES}$) removes most of this background, see Sections 3.5 and 3.4. The distribution of the remaining $q\overline{q}$ events can be seen in

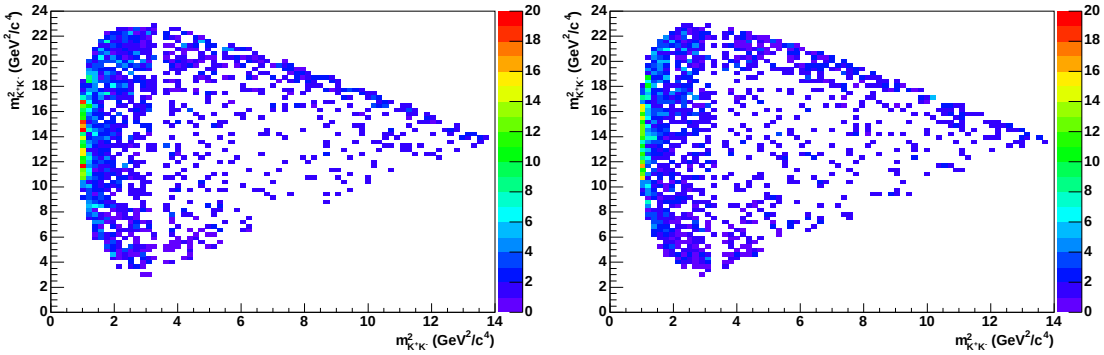

Figure 4.6: *Dalitz plot distributions for continuum ($q\overline{q}$) background events. The left plot is the B^+ distribution and the right is B^-. The colour scale shows the number of events expected per bin in the data sample.*

Figure 4.6. The histograms are generated using Sideband data combined with off-resonance data to increase statistics. The correct fraction of $B\overline{B}$ background is then subtracted using numbers from Section 4.5.3 and the $B\overline{B}$ distribution histograms from Section 4.5.2.

Along the edges of the $q\overline{q}$ Dalitz plot is a $\phi(1020)$ resonance. As the ϕ is so thin ($\sim$4 MeV) a very finely binned histogram is needed to correctly model it. After many unsuccessful tests with various bin sizes it was decided to move the plot to a different co-ordinate system to inflate the region around the ϕ. The new co-ordinates m' and θ' are defined as

$$\begin{aligned} m' &= \frac{1}{\pi}\cos^{-1}\left(\frac{2(m_{++}-m_{++(min)})}{m_{++(max)}-m_{++(min)}}-1\right) \\ \theta' &= \frac{1}{\pi}\theta_{++}, \end{aligned} \tag{4.9}$$

where m_{++} is the invariant mass of the like-sign kaon pair, $m_{++(max)} = m_B - m_K$,

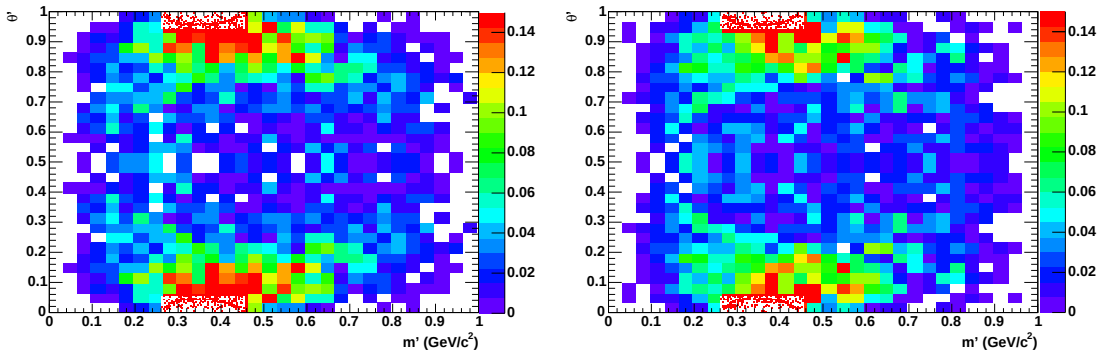

Figure 4.7: *Square Dalitz plot distributions for $q\overline{q}$ background events. 250×250 binning is used over the $\phi(1020)$ region and 30×30 binning elsewhere. The left plot is the B^+ distribution and the right is B^-. The colour scale shows the number of events expected per bin in the data sample.*

$m_{++(min)} = 2m_K$ and θ_{++} is the helicity angle between either of the like-sign kaons and the B momentum in the like-sign kaon rest frame. Both of the new co-ordinates vary from 0 to 1 giving a square plot. Figure 4.7 shows the distributions in the square co-ordinates. The histogram is binned in a 250×250 grid to give good detail in the $\phi(1020)$ region. The bulk of the plot is sparsely populated and so bins are merged and averaged to give pseudo 30×30 binning.

4.5.2 $B\overline{B}$ Background

The $B^\pm \to K^\pm K^\mp K^\pm$ decay mode suffers from relatively little $B\overline{B}$ background due to the tight PID constraints given by three kaons. What B background there is comes mainly from the misidentification of pions as kaons in high branching fraction D decays. However there are also some background modes that give a $K^\pm K^\mp K^\pm$ final state such as $B^+ \to J/\psi K^+$ $(J/\psi \to K^+K^-)$ and $B^+ \to \overline{D}^0 K^+$ $(\overline{D}^0 \to K^+K^-)$. Some $B^0\overline{B}^0$ events get misreconstructed to $K^\pm K^\mp K^\pm$, usually involving both misidentification of one or more particles and a particle being lost,

e.g. $B^0 \to K^+K^-K^0_S$ where $K^0_S \to \pi^+\pi^-$.

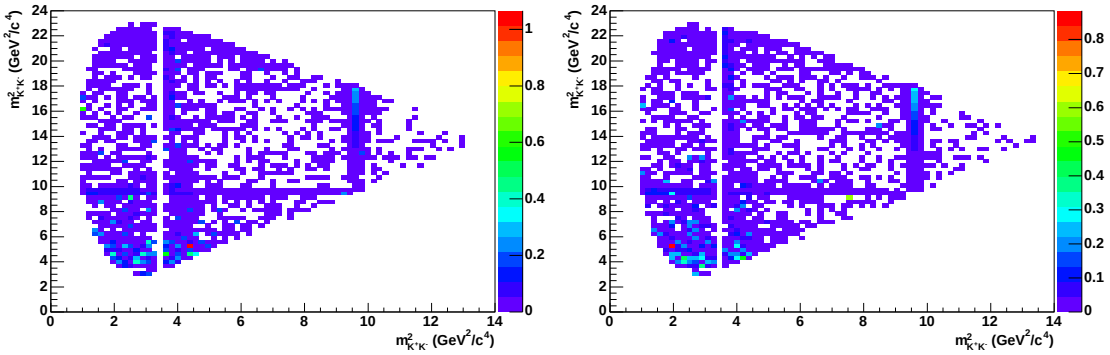

Figure 4.8: *Dalitz plot distributions for $B\overline{B}$ background events. The left plot is the B^+ distribution and the right is B^-. The colour scale shows the number of events expected per bin in the data sample.*

To determine the B decay modes that contribute significantly to backgrounds in the Signal Box large samples of generic $B\overline{B}$ MC were studied. 174 million B^+B^- events and 148 million $B^0\overline{B}^0$ events were processed and the MC truth information studied to determine the contributing decay modes. A set of exclusive MC was then generated for each individual background mode. After reconstruction and event selection the efficiencies were determined and using known branching fractions the expected number of events were calculated. Branching fractions were taken from either the Heavy Flavor Averaging Group tables or the Particle Data Group [9].

The sets of MC for each individual background mode were then summed together into one histogram giving the the overall $B\overline{B}$ background distribution. Figure 4.8 shows the normal Dalitz plot distribution and Figure 4.9 shows the distribution in the square co-ordinates. Tables 4.1-4.3 show the branching fractions, efficiencies and expected numbers of events for each B background mode.

Table 4.1: *B^+B^- background modes, with branching fractions, efficiencies and number of expected events. Continued in Table 4.2*

Mode	BF	Efficiency (%)		Number of Expected Events	
	(10^{-6})	Signal Strip	Signal Box	Signal Strip	Signal Box
$B^+ \to K^+K^-\pi^+$	< 6.3	0.4280 ± 0.0057	0.2384 ± 0.0043	6.3 ± 6.3	3.5 ± 3.5
$B^+ \to K^+\pi^-\pi^+$	4.9 ± 1.5	0.0134 ± 0.0010	0.00285 ± 0.00047	0.152 ± 0.048	0.032 ± 0.011
$B^+ \to \pi^+\pi^-\pi^+$	10.9 ± 3.7	0.00095 ± 0.00021	0.00072 ± 0.00018	0.0239 ± 0.0097	0.0182 ± 0.0077
$B^+ \to K_0^{*0}(1430)\pi^+$; $K_0^{*0}(1430) \to K^+\pi^-$	32.3 ± 3.1	0.0124 ± 0.0026	0.0051 ± 0.0017	0.93 ± 0.22	0.38 ± 0.13
$B^+ \to J/\psi K^+$; $J/\psi \to K^+K^-$	0.24 ± 0.03	19.987 ± 0.074	19.797 ± 0.074	11.0 ± 1.5	10.9 ± 1.5
$B^+ \to K_S^0K^+$; $K_S^0 \to \pi^+\pi^-$	< 0.41	0.0154 ± 0.0029	0.0044 ± 0.0016	0.015 ± 0.015	0.0042 ± 0.0042
$B^+ \to \overline{D}^0K^+$; $\overline{D}^0 \to K^+K^-$	1.4 ± 0.2	0.581 ± 0.015	0.1776 ± 0.0084	1.94 ± 0.33	0.59 ± 0.10
$B^+ \to \overline{D}^0K^+$; $\overline{D}^0 \to K^+\pi^-$	14.1 ± 2.3	0.448 ± 0.011	0.1669 ± 0.0068	14.6 ± 4.2	5.4 ± 1.6
$B^+ \to \overline{D}^0K^+$; $\overline{D}^0 \to K^+\pi^-\pi^0$	48.1 ± 8.3	0.2063 ± 0.0090	0.0433 ± 0.0041	23.0 ± 4.1	4.82 ± 0.96
$B^+ \to \overline{D}^0\pi^+$; $\overline{D}^0 \to K^+K^-$	20.5 ± 1.4	0.0150 ± 0.0087	0.0 ± 0.0	0.67 ± 0.39	0.0 ± 0.0
$B^+ \to \overline{D}^0\pi^+$; $\overline{D}^0 \to K^+\pi^-$	189.2 ± 11.9	0.0139 ± 0.0025	0.0028 ± 0.0011	6.1 ± 1.2	1.22 ± 0.50
$B^+ \to \overline{D}^0\pi^+$; $\overline{D}^0 \to K^+\pi^-\pi^0$	647.4 ± 54.8	0.0068 ± 0.0017	0.00161 ± 0.00080	10.2 ± 2.6	2.4 ± 1.2
Total B^+B^- backgrounds				116 ± 10	40.0 ± 4.7
Total B backgrounds				229 ± 21	65.4 ± 6.5

Table 4.2: *B^+B^- background modes continued from Table 4.1.*

Mode	BF	Efficiency (%)		Number of Expected Events	
	(10^{-6})	Signal Strip	Signal Box	Signal Strip	Signal Box
$B^+ \to \overline{D}^{*0}K^+$; $\overline{D}^{*0} \to \overline{D}^0\pi^0$; $\overline{D}^0 \to K^+K^-$	0.87 ± 0.25	0.657 ± 0.047	0.103 ± 0.019	1.32 ± 0.39	0.208 ± 0.070
$B^+ \to \overline{D}^{*0}K^+$; $\overline{D}^{*0} \to \overline{D}^0\pi^0$; $\overline{D}^0 \to K^+\pi^-$	8.5 ± 3.1	0.435 ± 0.012	0.1361 ± 0.0069	8.5 ± 3.2	2.67 ± 0.99
$B^+ \to \overline{D}^{*0}K^+$; $\overline{D}^{*0} \to \overline{D}^0\pi^0$; $\overline{D}^0 \to K^+\pi^-\pi^0$	29.0 ± 8.4	0.1142 ± 0.0097	0.0142 ± 0.0034	7.7 ± 2.3	0.95 ± 0.36
$B^+ \to \overline{D}^{*0}K^+$; $\overline{D}^{*0} \to \overline{D}^0\gamma$; $\overline{D}^0 \to K^+K^-$	0.53 ± 0.16	0.626 ± 0.016	0.1328 ± 0.0071	0.81 ± 0.24	0.164 ± 0.049
$B^+ \to \overline{D}^{*0}K^+$; $\overline{D}^{*0} \to \overline{D}^0\gamma$; $\overline{D}^0 \to K^+\pi^-$	5.2 ± 1.9	0.462 ± 0.013	0.1430 ± 0.0074	5.6 ± 2.1	1.73 ± 0.65
$B^+ \to \overline{D}^{*0}K^+$; $\overline{D}^{*0} \to \overline{D}^0\gamma$; $\overline{D}^0 \to K^+\pi^-\pi^0$	17.8 ± 5.3	0.076 ± 0.014	0.0048 ± 0.0018	3.1 ± 1.1	0.39 ± 0.23
$B^+ \to \overline{D}^{*0}\pi^+$; $\overline{D}^{*0} \to \overline{D}^0\pi^0$; $\overline{D}^0 \to K^+K^-$	11.1 ± 1.2	0.0306 ± 0.0046	0.0034 ± 0.0012	0.79 ± 0.14	0.122 ± 0.048
$B^+ \to \overline{D}^{*0}\pi^+$; $\overline{D}^{*0} \to \overline{D}^0\pi^0$; $\overline{D}^0 \to K^+\pi^-$	108.2 ± 11.0	0.0159 ± 0.0026	0.00200 ± 0.00076	4.00 ± 0.77	0.86 ± 0.32
$B^+ \to \overline{D}^{*0}\pi^+$; $\overline{D}^{*0} \to \overline{D}^0\pi^0$; $\overline{D}^0 \to K^+\pi^-\pi^0$	370.2 ± 43.1	0.0051 ± 0.0012	0.0034 ± 0.0015	4.4 ± 1.2	1.72 ± 0.68
$B^+ \to \overline{D}^{*0}\pi^+$; $\overline{D}^{*0} \to \overline{D}^0\gamma$; $\overline{D}^0 \to K^+K^-$	6.82 ± 0.82	0.0224 ± 0.0039	0.0062 ± 0.0018	0.355 ± 0.075	0.054 ± 0.025
$B^+ \to \overline{D}^{*0}\pi^+$; $\overline{D}^{*0} \to \overline{D}^0\gamma$; $\overline{D}^0 \to K^+\pi^-$	66.6 ± 7.9	0.0182 ± 0.0031	0.00167 ± 0.00084	2.81 ± 0.58	0.96 ± 0.30
$B^+ \to \overline{D}^{*0}\pi^+$; $\overline{D}^{*0} \to \overline{D}^0\gamma$; $\overline{D}^0 \to K^+\pi^-\pi^0$	227.8 ± 29.8	0.0050 ± 0.0014	0.0017 ± 0.0017	2.65 ± 0.84	0.88 ± 0.46
Total B^+B^- backgrounds				116 ±10	40.0 ± 4.7
Total B backgrounds				229 ± 21	65.4 ± 6.5

Table 4.3: *$B^0\overline{B}^0$ background modes, with branching fractions, efficiencies and number of expected events.*

Mode	BF	Efficiency (%)		Number of Expected Events	
	(10^{-6})	Signal Strip	Signal Box	Signal Strip	Signal Box
$B^0 \to D^- K^+$	200 ± 60	0.0915 ± 0.0061	0.0199 ± 0.0028	42 ± 13	9.2 ± 3.0
$B^0 \to D^{*-} K^+$	200 ± 50	0.0992 ± 0.0063	0.0247 ± 0.0032	46 ± 12	11.4 ± 3.2
$B^0 \to D^{*-}\pi^+$; $D^{*-} \to \overline{D}^0\pi^-$; $\overline{D}^0 \to X$	1868 ± 142	0.00154 ± 0.00019	0.000379 ± 0.000095	6.66 ± 0.97	1.63 ± 0.43
$B^0 \to D^{*-}\rho^+$; $D^{*-} \to \overline{D}^0\pi^-$; $\overline{D}^0 \to X$	4942 ± 102	0.00019 ± 0.00013	0.0 ± 0.0	2.0 ± 1.5	0.0 ± 0.0
$B^0 \to K^+ K^- K^0_S$	12.4 ± 1.2	0.2136 ± 0.0098	0.0541 ± 0.0050	6.2 ± 1.3	1.57 ± 0.37
$B^0 \to K^+ K^- \pi^0$	19.0 ± 9.5	0.194 ± 0.012	0.0333 ± 0.0051	8.5 ± 4.3	1.47 ± 0.77
$B^0 \to K^+ \pi^- \pi^0$	36.6 ± 5.2	0.00707 ± 0.00055	0.00035 ± 0.00012	0.599 ± 0.098	0.029 ± 0.011
$B^0 \to K^+ \pi^-$	18.2 ± 0.8	0.00043 ± 0.00015	0.000053 ± 0.000053	0.0180 ± 0.0064	0.0023 ± 0.0023
Total $B^0\overline{B}^0$ backgrounds				112 ± 18	25.4 ± 4.5
Total B backgrounds				229 ± 21	65.4 ± 6.5

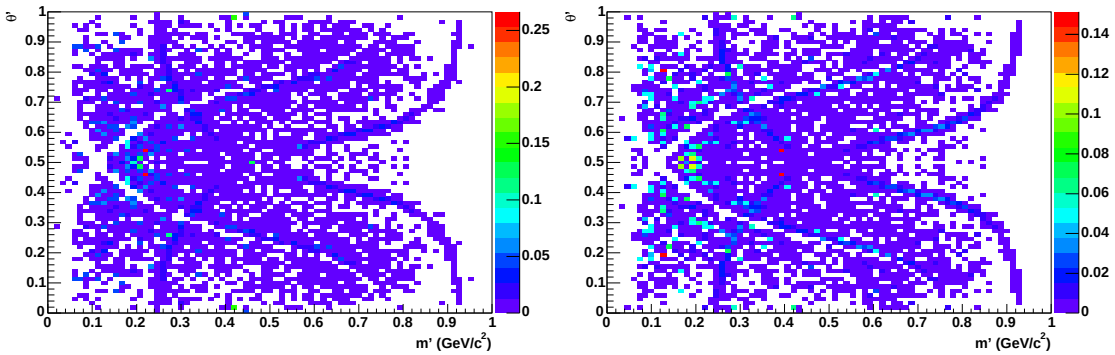

Figure 4.9: *Square Dalitz plot distributions for $B\overline{B}$ background events. The left plot is the B^+ distribution and the right is B^-. The clearly visible unpopulated bands correspond to the D^0 veto. The colour scale shows the number of events expected per bin in the data sample.*

4.5.3 Determination of the Signal to Background ratio

The fractions of $q\overline{q}$ and $B\overline{B}$ background within the Signal Box are determined by a fit to the $m_{\rm ES}$ distribution in the Signal Strip. In this fit the signal is modelled by a double Gaussian function, the parameters of which are given by a fit to truth-matched $B^{\pm} \to K^{\pm}K^{\mp}K^{\pm}$ nonresonant MC, see Figure 4.10. The $q\overline{q}$ background is modelled with an Argus function [63]. The end-point of the Argus function is set to the B mass and the shape parameter is floated in the fit. An example Argus fit is shown in Figure 4.11. $B\overline{B}$ background has both peaking and non-peaking components and as such is modelled by a combination Argus + Gaussian functions, see Figure 4.12. The parameters are fixed using $B\overline{B}$ background MC.

The numbers of signal and $q\overline{q}$ events are floated in the fit, but the number of $B\overline{B}$ background events is fixed from earlier studies. The results of the full $m_{\rm ES}$ fit can be found in Section 5.6.

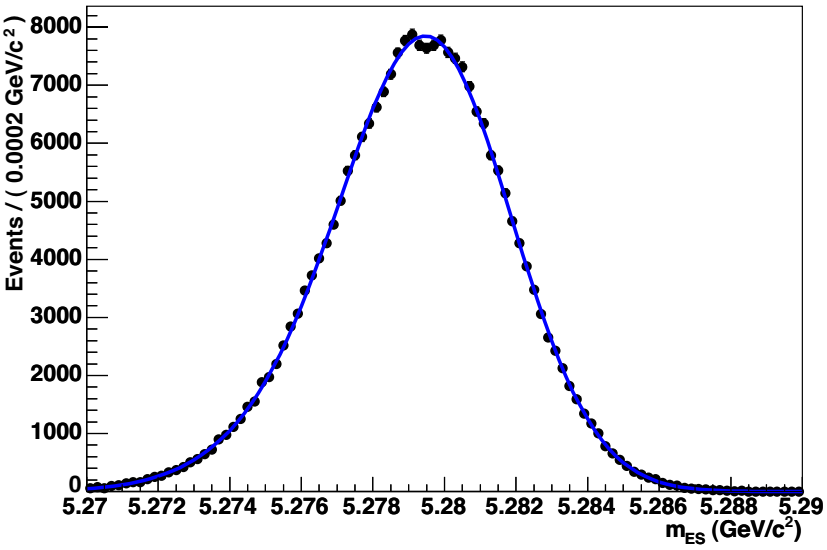

Figure 4.10: *The $m_{\rm ES}$ distribution of $B^{\pm} \to K^{\pm}K^{\mp}K^{\pm}$ nonresonant MC events. The blue line shows the double Gaussian fit.*

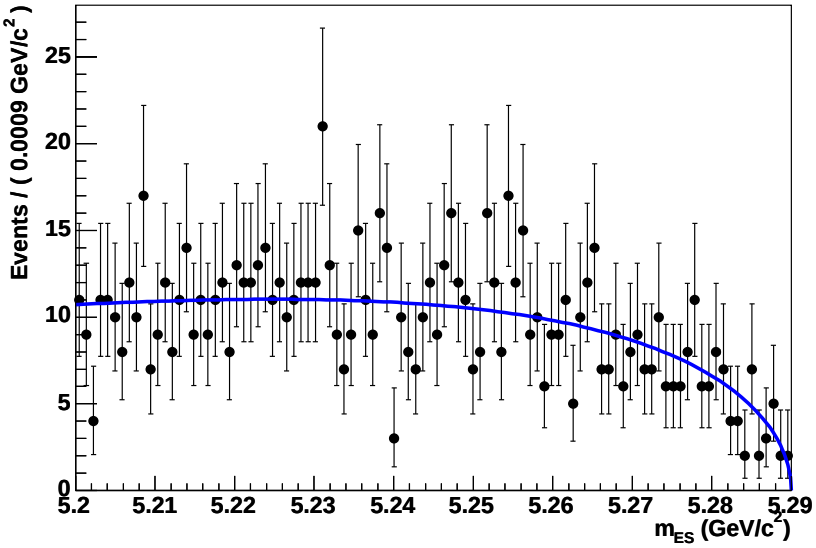

Figure 4.11: *The $m_{\rm ES}$ distribution for off-resonance data, fitted with an Argus function.*

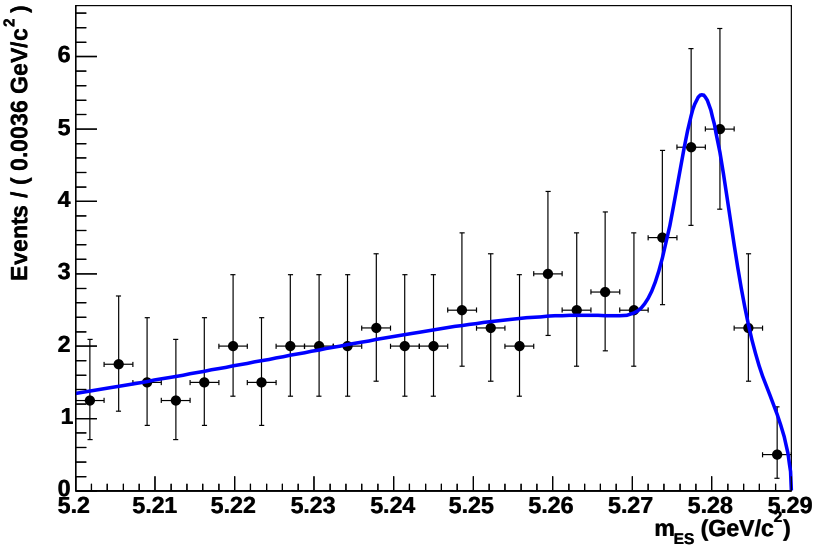

Figure 4.12: *The $m_{\rm ES}$ distribution of the $B\overline{B}$ background. The line shows the Argus + Gaussian fit.*

4.6 The Signal Model

To determine the makeup of the signal model the resonant structure of the data had to be examined. Figure 4.1 shows the Dalitz plot and Figure 4.13 shows mass projections of the selected Signal Box events. As both B^+ and B^- datasets are very similar the combined dataset is used in all signal model studies to increase the statistical accuracy. Figure 4.14 shows projection plots of the combined dataset.

A clear $\phi(1020)$ signal can be seen near 1 GeV/c. The χ_{c0} is seen just below 3.5 GeV/c (in both mass projections) and the non-χ_{c0} structure visible in the heavy-pair mass projection is mostly the reflection of the $\phi(1020)$.

The nature of the wide resonance located around 1.5 GeV/c is unknown. No matching particle is found in the Particle Data Group tables [9]. It is discussed in detail in Section 4.6.1.

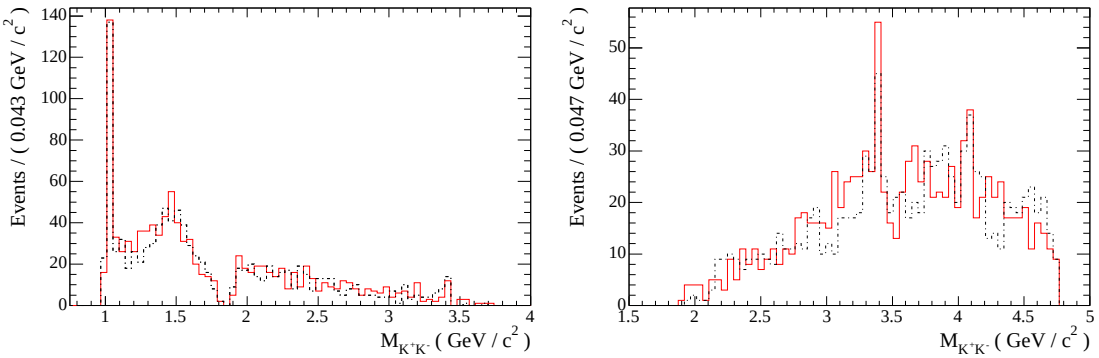

Figure 4.13: *Comparison mass projection plots for opposite-sign kaon pairs in the B^+ and B^- data samples. The solid red line shows B^+ events and the dashed black line shows B^- events. The left-hand plot shows the light mass pairs and the right-hand plot shows the heavier mass pairs from the folded Dalitz plot.*

Other than these three obvious resonances a non-peaking $f_0(980)$ contribution is expected as well as $B^\pm \to K^\pm K^\mp K^\pm$ nonresonant events. The $\phi(1680)$ resonance is also included in the final signal model as it was found to help stabilise the fit.

The signal model therefore has has six components:

- $\diamond$ $B^\pm \to K^\pm K^\mp K^\pm$ (nonresonant)
- $\diamond$ $B^\pm \to f_0(980) K^\pm$
- $\diamond$ $B^\pm \to \phi(1020) K^\pm$
- $\diamond$ $B^\pm \to (KK)^0_0 K^\pm$, where $(KK)^0_0$ is a scalar resonance with a mass $\sim$1.5 GeV/c.
- $\diamond$ $B^\pm \to \phi(1680) K^\pm$
- $\diamond$ $B^\pm \to \chi_{c0} K^\pm$

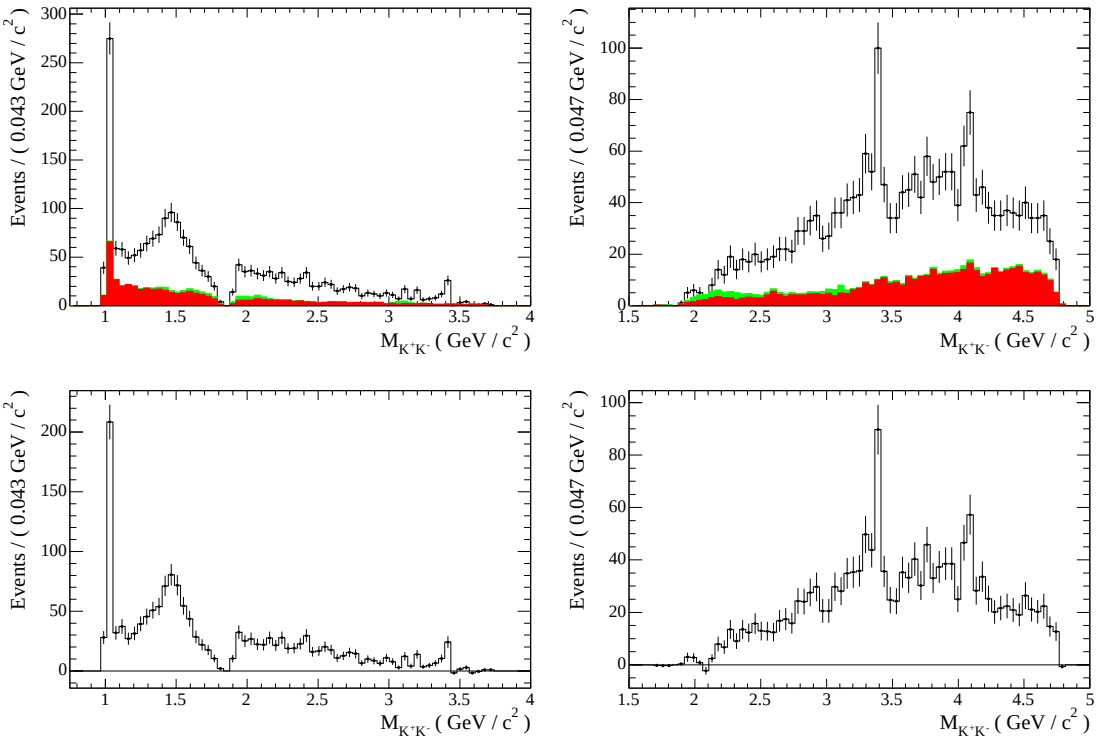

Figure 4.14: *Mass pair projection plots for the complete dataset. The top row shows the data and background model, and the bottom row shows the events left after subtracting the background from the data. The left-hand plots show the light $K\overline{K}$ pair and the right-hand plots show the heavier pair. The data are represented by the black points and black line. The solid red histogram shows the $q\overline{q}$ background model and the solid green histogram shows the $B\overline{B}$ background model.*

All resonances except for the $f_0(980)$ are modelled using relativistic Breit-Wigner lineshapes. The $f_0(980)$ is modelled using the Flatté model [27] (a coupled Breit-Wigner) and the nonresonant contribution is described by an empirical model. These models are described in Sections 4.6.2, 4.6.3 and 4.6.4.

Other resonances that were considered include the $f_2(1270)$, $f_0(1370)$, $f_0(1500)$ and $f_2'(1525)$.

4.6.1 The $(KK)_0^0$

The component named $(KK)_0^0$ was included as a way of modelling a prominent resonant structure around $1.5\,\mathrm{GeV}/c^2$. It is taken to be a scalar for the following reasons:

- ◇ The helicity distribution for this region is flat except for an enhancement towards $\cos\theta_H = 1$, see Figure 4.15. Looking at Figure 4.15 one might think that a scalar combined with a vector would give the best fit, but it doesn't. The best fit comes with using a single scalar. Neither a vector nor tensor give a good fit.
- ◇ A partial-wave analysis of this region has been performed [64], which indicates a large s-wave contribution.

A likelihood scanning approach was used to determine its mass and width, see Section 4.7.

The most obvious scalar resonance in this region that has an appreciable decay rate to K^+K^- is the $f_0(1500)$. This resonance was tried initially, but it was too thin to give a good fit to the data. Additionally the $f_0(1500)$ has a branching

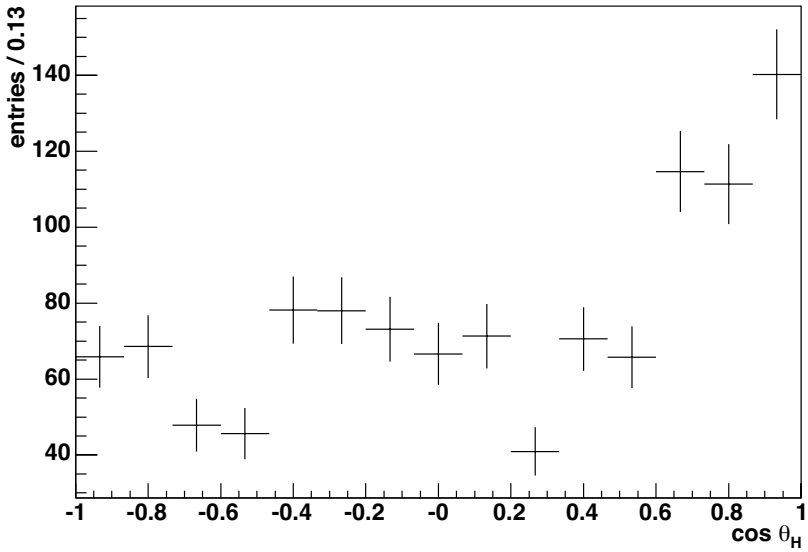

Figure 4.15: *Background subtracted, efficiency corrected* $\cos\theta_H$ *plot of the region* m_{KK} *1.35-1.62* GeV/c^2.

ratio of $(8.6 \pm 1.0)\%$ to K^+K^-, compared to $(34.9 \pm 2.3\%)$ to $\pi^+\pi^-$ [9]. It would therefore be expected to occur significantly in the decay $B^\pm \to K^\pm\pi^\mp\pi^\pm$ if it occurs in $B^\pm \to K^\pm K^\mp K^\pm$, but there is no $f_0(1500)$ signal seen in previous Dalitz plot analyses of $B^\pm \to K^\pm\pi^\mp\pi^\pm$ [32], [34]. This suggests that the resonance has a high $s\bar{s}$ content, such that it decays strongly to K^+K^-, but not to $\pi\pi$.

The BELLE collaboration have also seen a comparable unknown resonance in their Dalitz analysis of $B^\pm \to K^\pm K^\mp K^\pm$ [34] and dealt with it similarly.

4.6.2 Relativistic Breit-Wigner

Most resonances can be modelled by a relativistic Breit-Wigner distribution,

$$R_j(m) = \frac{1}{(m_0^2 - m^2)^2 + m_0^2\Gamma^2(m)}, \tag{4.10}$$

where m is the reconstructed mass of the resonance, m_0 is the actual mass and $\Gamma(m)$ is the mass-dependent resonance decay width, given by [65]:

$$\Gamma(m) = \Gamma_0 \left(\frac{q}{q_0}\right)^{2k+1} \left(\frac{m_0}{m}\right) \frac{f_k^2(q)}{f_k^2(q_0)}, \tag{4.11}$$

where q is the momentum of either of the daughter particles in the rest frame, Γ_0 is the resonance width and q_0 is the value of q when $m = m_0$. Γ_0 and m_0 are obtained from standard tables [9]. k denotes the spin of the resonance and

$$f_0(q) = 1 \tag{4.12}$$

$$f_1(q) = \sqrt{1/(1 + r^2q^2)} \tag{4.13}$$

$$f_2(q) = \sqrt{1/(r^4q^4 + 3r^2q^2 + 9)} \tag{4.14}$$

where $r \approx 4.0\,\mathrm{GeV}/c$ is the "radius" of the interaction, first introduced by Blatt and Weisskopf [65].

4.6.3 Flatté

The $f_0(980)$ needs to be modelled slightly differently to the other resonances, to take into account the fact that it lies very close to the K^+K^- threshold. A coupled-channel Breit Wigner or Flatté is used. The mass-dependent width formula is now given by the sum of the widths in the $\pi\pi$ and KK systems [27],

$$\Gamma(m) = \Gamma_\pi(m) + \Gamma_K(m), \tag{4.15}$$

where

$$\Gamma_\pi(m) = g_\pi \sqrt{m^2 - 4m_\pi^2} \tag{4.16}$$

$$\Gamma_K(m) = g_K \sqrt{m^2 - 4m_K^2} \tag{4.17}$$

and m_π and m_K are the invariant masses of the pion and kaon, and g_π and g_K are experimentally determined coupling constants. There are three main sets of results for g_π and g_K:

- ◇ $g_\pi = 0.138 \pm 0.010$ and $g_K/g_\pi = 4.45 \pm 0.25$ – BES Collaboration [28]
- ◇ $g_\pi = 0.09 \pm 0.01 \pm 0.01$ and $g_K = 0.02 \pm 0.04 \pm 0.03$ – E791 Collaboration [29]
- ◇ $g_\pi = 0.28 \pm 0.04$ and $g_K = 0.56 \pm 0.18$, with $g_K/g_\pi = 2.0 \pm 0.9$ – WA76 Collaboration [30]

The E791 measurement comes from an analysis of $D_s^\pm \to \pi^\pm\pi^\mp\pi^\pm$, with no direct observation of $f_0(980) \to K^+K^-$. The WA76 analysis studies centrally produced $\pi\pi$ and $K\overline{K}$ pairs from proton-proton and pion-proton collisions. Their $f_0(980)$ measurements come from an observation in the $\pi\pi$ spectrum, but their $K\overline{K}$ spectrum results suffered from high background, resulting in no clear observation.

The BES result comes from a joint analysis of $J/\psi \to \phi\pi^+\pi^-$ and $J/\psi \to \phi K^+K^-$. As this is the only result to directly use K^+K^- events in the measurement, the BES results are considered to be superior, and as such this analysis uses the BES results as inputs for the Flatté model.

4.6.4 Choice of Nonresonant Model

Traditionally nonresonant decay is modelled as a uniform distribution across the allowed phase space, however this model did not fit the data. An attempt at fitting two other theoretical models [66], [67] has been made on the *BABAR* dataset [64], but neither could adequately describe the data.

In this analysis two ad hoc empirical models are tested. The first was proposed by the BELLE collaboration and is used in their Dalitz analysis of $B^\pm \to K^\pm K^\mp K^\pm$ [34]. It has the form:

$$F_j(x, y) = e^{\alpha x} + e^{\alpha y}, \tag{4.18}$$

where $x = m^2_{13}(K^+K^-)$ and $y = m^2_{23}(K^+K^-)$ are the invariant mass-squared pairs of the two possible charge-zero combinations of the three kaons, and α is a constant to be determined. This shall be referred to as the Exponential model.

A second empirical model:

$$F_j(x, y) = 1 + \alpha \frac{x + y}{m^2_B}, \tag{4.19}$$

was put forward by Dvoretskii [64]. Again x and y are the invariant mass-squared pairs and α is a constant to be determined. This shall be referred to as the Taylor (expansion) model.

Likelihood scanning (see Sections 4.7 and 5.2) was used to determine the optimal α values of the two models. Both models gave comparable likelihoods for the best fit, but the Taylor model showed less multiple solutions (see Section 5.3.1) and more reasonable fit fractions (the Exponential model best fit gave a total fit fraction of $\sim 180\%$), so the Taylor model was used for the final results of this analysis.

4.7 Using a Likelihood Scan to Fix Fit Components

The floating of any parameter which affects a component's shape is computationally very expensive in a Dalitz fit. This is because the integration of the lineshapes must be recalculated for each iteration. Also `Laura++` was not written with the floating of such parameters in mind, and would have required a major rewrite. Therefore a likelihood scanning technique is used to determine the nonresonant α parameter and the mass and width of the $(KK)^0_0$.

The likelihood scan consists of performing the fit a number of times, each time with a different value of one of the parameters, for example, fitting over ten different

masses in the range 1.4 to 1.6 GeV/c^2. The mass is then set to the best fit and the width is varied. Finally the mass and width are fixed at the optimal values and α is varied. As the three parameters are highly correlated it is necessary to work through this cycle a number of times until the fit stabilises. To maximise statistical accuracy the fits are performed on the combined dataset.

A plot of each parameter against the likelihood value is then produced and fitted. The minimum of the fit is then used as the best value for the required parameter. Errors on these parameters are calculated by finding the values of the parameter at which the likelihood is ± 0.5 units above the minimum.

5

Analysis Results

5.1 Introduction

This chapter presents the results of the Dalitz fit and also the total rate measurement. Details of the error analysis follow both sets of results.

Other topics that are covered include multiple solutions, goodness of fit tests and various cross-checks of the signal model.

5.2 Results of the Likelihood Scan

This section gives the results of using a likelihood scan to determine the $(KK)^0_0$ mass and width, and the value of the α parameter that is used in the models that describe the shape of the nonresonant component (Section 4.6.4 gives details of the nonresonant models). The likelihood scan consists of performing the Dalitz fit a number of times, each time with a different value of one of the parameters. A plot of each parameter against the likelihood value is then produced and fitted. The minimum of the fit is then used as the best value for the required parameter. For full details of the procedure see Section 4.7.

The Dalitz fit was found to converge upon different solutions given different starting conditions. These multiple solutions are discussed in more detail in Section 5.3.1. To overcome the problem each Dalitz fit was performed 100 times with randomised starting conditions each time, and the fit with the lowest likelihood was taken.

The best fit using the "Taylor" nonresonant model gives:

- ◇ The nonresonant α value to be $-0.799^{+0.038}_{-0.034}$. See Figure 5.1.
- ◇ The scalar mass as $(1.523^{+0.028}_{-0.020})\,\mathrm{GeV}/c^2$. See Figure 5.2.
- ◇ The scalar width to be $(175^{+32}_{-27})\,\mathrm{MeV}/c^2$. See Figure 5.3.

Using the "Exponential" nonresonant model gave the following results:

- ◇ The nonresonant α value to be 0.152 ± 0.012.
- ◇ The scalar mass as $(1.590^{+0.023}_{-0.022})\,\mathrm{GeV}/c^2$.
- ◇ The scalar width to be $(232^{+45}_{-39})\,\mathrm{MeV}/c^2$.

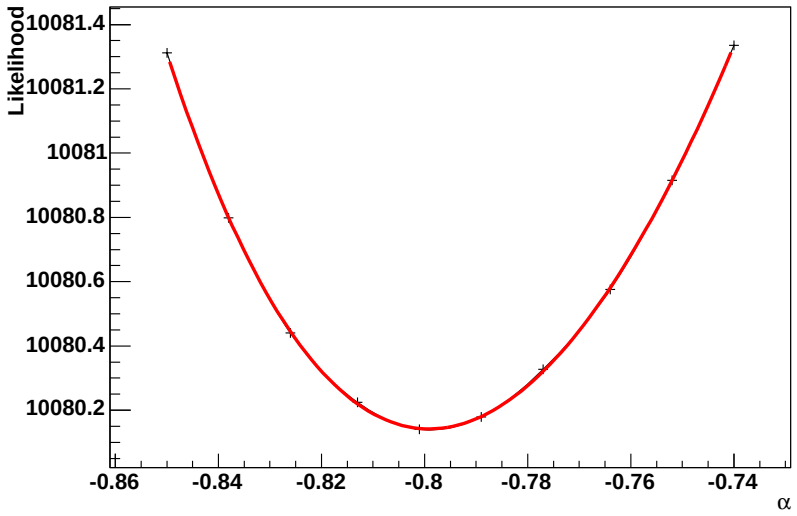

Figure 5.1: *Likelihood scan of nonresonant α. The red line is a quartic fit to the data.*

Both models give comparable likelihoods for the best fit, but the Taylor model shows less multiple solutions and more reasonable fit fractions (the best fit for the Exponential model gives a total fit fraction of $\sim 180\%$), and therefore the Taylor model results are used to fix the components for the final results of this analysis.

5.3 Dalitz Fit Results

The results of the Dalitz fit to the nominal signal model are shown in Table 5.1 and figure 5.4 shows a comparison between the fit and the data. The fit results around the main resonances show good agreement with the data.

The fit outputted a number of differing solutions, the best two of which could not be chosen between leading to two χ_{c0} solutions being quoted. Multiple solutions are discussed in more depth in Section 5.3.1 with Tables 5.3 and 5.4 showing the full

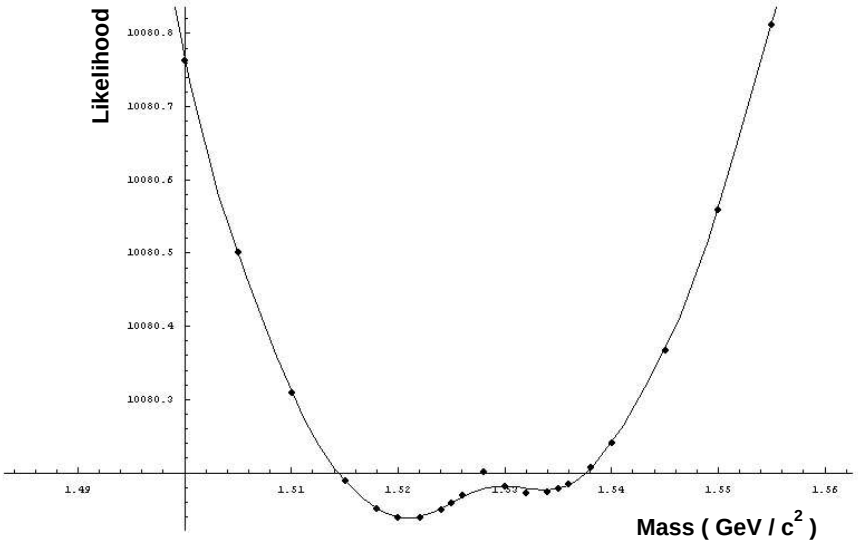

Figure 5.2: *Likelihood scan of the scalar mass. The peak in the centre made the distribution non-trivial to fit for, so Mathematica's InterpolatingPolynomial function was used to find the minima. The black line shows Mathematica's fit.*

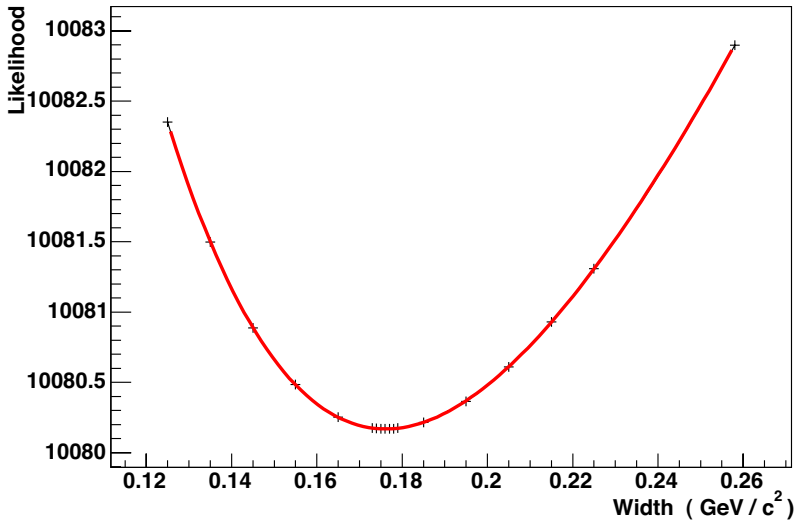

Figure 5.3: *Likelihood scan of the scalar width. The red line is a quartic fit to the data.*

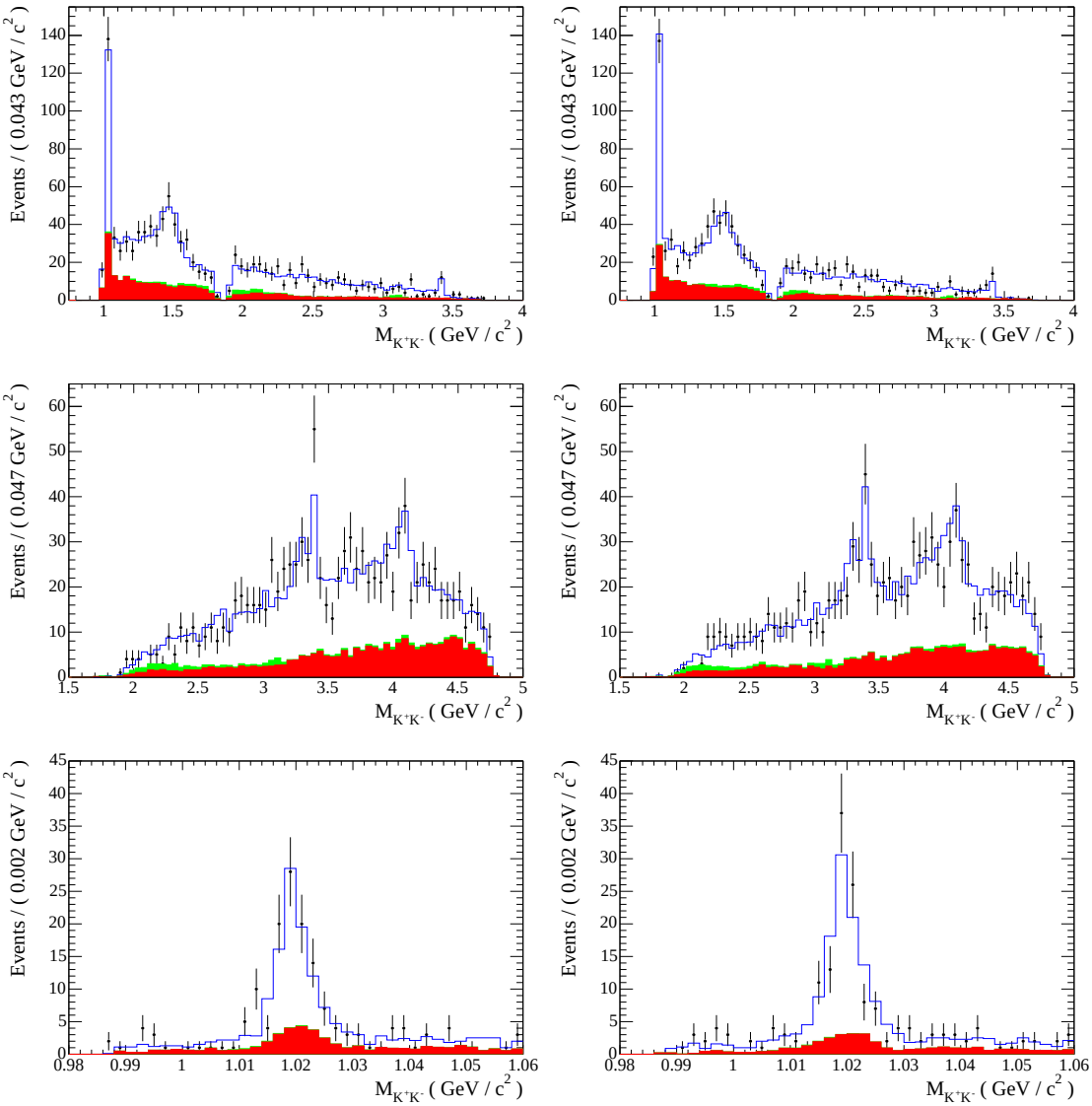

Figure 5.4: *Mass pair projection plots for the B^+ (left) and B^- (right) fits. The data are represented by the black points and the fit result by the solid blue line. The solid red histogram shows the $q\overline{q}$ background model and the solid green histogram shows the model for the $B\overline{B}$ background. The top row shows the light pair projection. The middle row shows the heavy pair projection and the bottom row gives a zoomed in view of the $\phi(1020)$ region of the light pair plot. The unpopulated region around 1.8 GeV/c in the light pair plot corresponds to the D^0 veto.*

details of all the leading fits.

	B^+	B^-
Average Efficiency (%)	$19.16 \pm 0.10 \pm 0.08$	$19.10 \pm 0.10 \pm 0.11$
Nonresonant Fraction (%)	$54.3 \pm 9.5 \pm 3.0$	$51.7 \pm 9.0 \pm 4.1$
Nonresonant Phase	0.0 FIXED	0.0 FIXED
$f_0(980)$ Fraction (%)	$23.3 \pm 8.7 \pm 3.8$	$26.5 \pm 7.7 \pm 3.8$
$f_0(980)$ Phase	$2.21 \pm 0.41 \pm 0.12$	$1.96 \pm 0.23 \pm 0.14$
$\phi(1020)$ Fraction (%)	$11.2 \pm 1.4 \pm 0.43$	$13.0 \pm 1.7 \pm 0.43$
$\phi(1020)$ Phase	$-2.99 \pm 0.46 \pm 0.11$	$2.97 \pm 0.25 \pm 0.13$
$(KK)_0^0$ Fraction (%)	$9.9 \pm 3.0 \pm 1.8$	$8.6 \pm 2.5 \pm 1.8$
$(KK)_0^0$ Phase	$-0.84 \pm 0.19 \pm 0.09$	$-1.38 \pm 0.23 \pm 0.20$
$\phi(1680)$ Fraction (%)	$0.74 \pm 0.83 \pm 2.1$	$2.4 \pm 1.2 \pm 0.34$
$\phi(1680)$ Phase	$-0.27 \pm 0.52 \pm 1.0$	$-1.16 \pm 0.30 \pm 0.23$
χ_{c0} Fraction A (%)	$3.1 \pm 0.92 \pm 0.55$	$3.4 \pm 0.77 \pm 0.14$
χ_{c0} Phase A	$-0.35 \pm 0.33 \pm 0.21$	$-0.56 \pm 0.26 \pm 0.04$
χ_{c0} Fraction B (%)	$5.9 \pm 1.2 \pm 0.64$	$6.7 \pm 1.3 \pm 0.34$
χ_{c0} Phase B	$0.58 \pm 0.21 \pm 0.21$	$0.65 \pm 0.22 \pm 0.06$
χ_{c0} Mean Fraction (%)	$4.5 \pm 1.2 \pm 0.64$	$5.0 \pm 1.3 \pm 0.34$

Table 5.1: *Dalitz plot fit results. The first error is statistical and the second is systematic. The mean of the two leading solutions is taken for all components other than the χ_{c0}, where both solutions are given.*

The statistical errors for the magnitudes and phases of each component are generated by `Minuit` during the fit. However when the statistical errors on the fit fractions are calculated, from the magnitudes and phases, it does not take into account the correlations between the different components and so is not accurate. Instead the statistical errors for the fit fractions in Table 5.1 are given by a toy Monte Carlo

study.

500 sets of 1058 and 1014 events are generated using amplitude and phase results from the B^+ and B^- fits. The Dalitz fit procedure is then applied to each set of toy MC with the initial amplitude and phase parameters being fixed to the generated values. This ensures that the fit will converge on the correct solution rather than an incorrect local minimum elsewhere in the phase space.

The fit fraction distribution of the 500 experiments is then plotted for each component and a Gaussian function is fitted to each distribution. The statistical error is then given by the width of the Gaussian. This method has been used in previous Dalitz plot analyses [32], [34] & [33].

Component	Fit Fraction Asymmetry (%)
Nonresonant	$-2 \pm 13 \pm 5$
$f_0(980)$	$6 \pm 21 \pm 11$
$\phi(1020)$	$7.4 \pm 8.0 \pm 2.5$
$(KK)^0_0$	$-7 \pm 25 \pm 14$
$\phi(1680)$	$53 \pm 26 \pm 36$
χ_{c0} A	$3.7 \pm 7.6 \pm 5.5$
χ_{c0} B	$7 \pm 22 \pm 9$
χ_{c0} Overall	$6 \pm 17 \pm 6$

Table 5.2: *Asymmetry results — the difference between the B^+ and B^- datasets. The first error is statistical and the second is systematic.*

All cross-checks detailed later in this chapter quote only the statistical errors generated by the fit as a significant amount of time and effort is required to produce fully accurate statistical and systematic errors.

Fit fraction asymmetry results are presented in Table 5.2. The asymmetry of each

component is consistent with zero.

5.3.1 Multiple Solutions

The fit is initialised using random magnitudes and phases as a starting point for the minimisation. It was noticed that different final solutions are obtained dependent upon the starting conditions, indicating the presence of several local minima in addition to the absolute minimum. To ensure the discovery of the global minima each fit was run 1000 times, each using a randomised set of initial parameters. The results of this can be seen in Tables 5.3 and 5.4 which show the lowest likelihood solutions for B^+ and B^- together with the closest few alternative solutions.

The best two solutions, in both the B^+ and B^- datasets, differ only in the fit for the χ_{c0} component. There are two distinct solutions which are given the arbitrary names 'A' and 'B':

- ◇ A) χ_{c0} has a fit fraction of ∼3% and a negative phase.
- ◇ B) χ_{c0} has a fit fraction of ∼6% and a positive phase.

Over the two datasets neither solution is favoured, and so for the calculation of branching fractions the mean of the two solutions is taken. Mean phases are quoted in the final result except in the case of the χ_{c0} where both phases are quoted.

The further solutions are often seen in pairs, where for instance the $(KK)^0_0$ can be seen with a fit fraction of around 9% or over 50%, giving rise to an overall fit fraction way above 100%. Different permutations of these pairs of results can lead to a spectrum of multiple solutions. However the vast majority of fits lead to either of the two lowest likelihood solutions. This and the strangeness of the

	B^+ Fit 1 (B)	B^+ Fit 2 (A)	B^+ Fit 3
$-\ln\mathcal{L}$	5193.8	5195.2	5200.6
# Fits	300/1000	186/1000	99/1000
Nonresonant Fraction (%)	56.63 ± 3.52	51.89 ± 5.58	62.11 ± 9.98
Nonresonant Phase	0.0 FIXED	0.0 FIXED	0.0 FIXED
$f_0(980)$ Fraction (%)	25.04 ± 4.88	21.64 ± 7.92	30.75 ± 8.04
$f_0(980)$ Phase	2.14 ± 0.23	2.28 ± 0.41	2.34 ± 0.24
$\phi(1020)$ Fraction (%)	11.08 ± 2.07	11.38 ± 2.76	11.04 ± 2.70
$\phi(1020)$ Phase	-3.02 ± 0.25	-2.96 ± 0.46	-2.82 ± 0.32
$(KK)_0^0$ Fraction (%)	10.73 ± 2.22	9.09 ± 2.19	77.22 ± 14.62
$(KK)_0^0$ Phase	-0.84 ± 0.19	-0.83 ± 0.26	0.65 ± 0.14
$\phi(1680)$ Fraction (%)	0.78 ± 0.66	0.69 ± 0.62	0.03 ± 0.19
$\phi(1680)$ Phase	-0.25 ± 0.52	-0.29 ± 0.50	-0.02 ± 3.49
χ_{c0} Fraction (%)	5.87 ± 1.37	3.11 ± 1.21	2.62 ± 1.22
χ_{c0} Phase	0.58 ± 0.21	-0.35 ± 0.33	-0.75 ± 0.31
Total Fraction (%)	110.1	97.8	183.8
Efficiency (%)	19.17 ± 0.10	19.15 ± 0.10	19.14 ± 0.10
Dalitz Plot $\chi^2/ndof$	62.0/53	67.1/54	68.7/53
Dalitz Plot p-value	0.19	0.11	0.07
$m_{K^+K^-}$(light) projection $\chi^2/ndof$	33.0/34	32.3/34	34.4/35
$m_{K^+K^-}$(light) projection p-value	0.52	0.55	0.50
$m_{K^+K^-}$(heavy) projection $\chi^2/ndof$	53.4/41	54.4/41	54.9/40
$m_{K^+K^-}$(heavy) projection p-value	0.09	0.08	0.06

Table 5.3: *Multiple solutions from the B^+ fit. (Errors on the fit fractions are from the* `Minuit` *fit.) The p-value is the probability of obtaining a result at least as extreme as that obtained given the χ^2 and the number of degrees of freedom.*

	B^- Fit 1 (A)	B^- Fit 2 (B)	B^- Fit 3	B^- Fit 4
$-\ln\mathcal{L}$	4910.7	4913.0	4914.3	4914.3
# Fits	311/1000	171/1000	21/1000	54/1000
Nonresonant Fraction (%)	52.52 ± 3.69	50.96 ± 3.35	86.78 ± 9.17	52.76 ± 9.12
Nonresonant Phase	0.0 FIXED	0.0 FIXED	0.0 FIXED	0.0 FIXED
$f_0(980)$ Fraction (%)	28.92 ± 4.95	24.01 ± 4.80	15.24 ± 4.92	24.19 ± 7.31
$f_0(980)$ Phase	1.88 ± 0.19	2.03 ± 0.23	0.12 ± 0.22	2.49 ± 0.29
$\phi(1020)$ Fraction (%)	12.95 ± 2.48	13.08 ± 2.52	12.45 ± 2.38	13.10 ± 3.28
$\phi(1020)$ Phase	2.88 ± 0.23	3.06 ± 0.25	-0.03 ± 0.29	-2.60 ± 0.33
$(KK)_0^0$ Fraction (%)	8.87 ± 1.88	8.41 ± 1.85	54.02 ± 7.04	76.17 ± 15.29
$(KK)_0^0$ Phase	-1.48 ± 0.23	-1.28 ± 0.23	1.54 ± 0.13	0.81 ± 0.16
$\phi(1680)$ Fraction (%)	2.28 ± 0.99	2.49 ± 1.05	1.11 ± 0.81	1.40 ± 1.12
$\phi(1680)$ Phase	-1.19 ± 0.30	-1.12 ± 0.29	2.93 ± 0.53	1.63 ± 0.51
χ_{c0} Fraction (%)	3.35 ± 1.06	6.72 ± 1.67	2.87 ± 0.92	6.25 ± 1.81
χ_{c0} Phase	-0.56 ± 0.26	0.65 ± 0.22	-1.00 ± 0.51	0.53 ± 0.20
Total Fraction (%)	108.9	105.7	172.5	173.9
Efficiency (%)	19.10 ± 0.10	19.10 ± 0.10	19.09 ± 0.10	19.09 ± 0.10
Dalitz Plot $\chi^2/ndof$	59.2/55	57.2/55	63.4/50	60.1/55
Dalitz Plot p-value	0.32	0.39	0.10	0.30
$m_{K^+K^-}$(light) projection $\chi^2/ndof$	48.7/34	49.8/34	52.6/33	50.0/34
$m_{K^+K^-}$(light) projection p-value	0.05	0.04	0.02	0.04
$m_{K^+K^-}$(heavy) projection $\chi^2/ndof$	49.7/39	49.2/39	49.7/39	56.0/39
$m_{K^+K^-}$(heavy) projection p-value	0.12	0.13	0.12	0.04

Table 5.4: *Multiple solutions from the B^- fit. (Errors on the fit fractions are from the* `Minuit` *fit.) The p-value is the probability of obtaining a result at least as extreme as that obtained given the χ^2 and the number of degrees of freedom.*

total fit fractions obtained from the less likely solutions suggest that results other than A and B can be safely ignored. It is worth noting that a previous analysis by the BELLE collaboration [34] also sees a multiple solution problem giving rise to solutions with large overall fit fractions. These solutions arise due to either large positive or negative interference between the nonresonant component, the $(KK)^0_0$ and to a lesser extent the $f_0(980)$.

The same multiple solutions are also seen in Monte Carlo tests, See Section 5.4.

5.3.2 Precision of the fit

To give an indication of the goodness of the fit and as an additional method for distinguishing between solutions (the other being likelihood values) χ^2 values are calculated. χ^2 is given by:

$$\chi^2 = \sum_{i=1}^{N_{Bins}} \frac{[y_i - f(x_i)]^2}{f(x_i)}, \tag{5.1}$$

where y_i is the number of data events found in bin i and $f(x_i)$ is the number of events in that bin as predicted by the fit results. The associated number of degrees of freedom ($ndof$) is calculated as $N_{Bins} - k - 1$, where k is the number of free parameters in the Dalitz-plot fit. A minimum of 10 entries in each bin is required; if this requirement is not met then neighbouring bins are combined. The binning of the Dalitz plot for this test can be seen in Figure 5.5.

The results in Tables 5.3 and 5.4 show the χ^2 values to be broadly in-line with the -ln(Likelihood) results. For this reason and due to problems such as obtaining an optimal binning structure for the χ^2 test priority is given to the -ln(Likelihood) numbers when deciding between results.

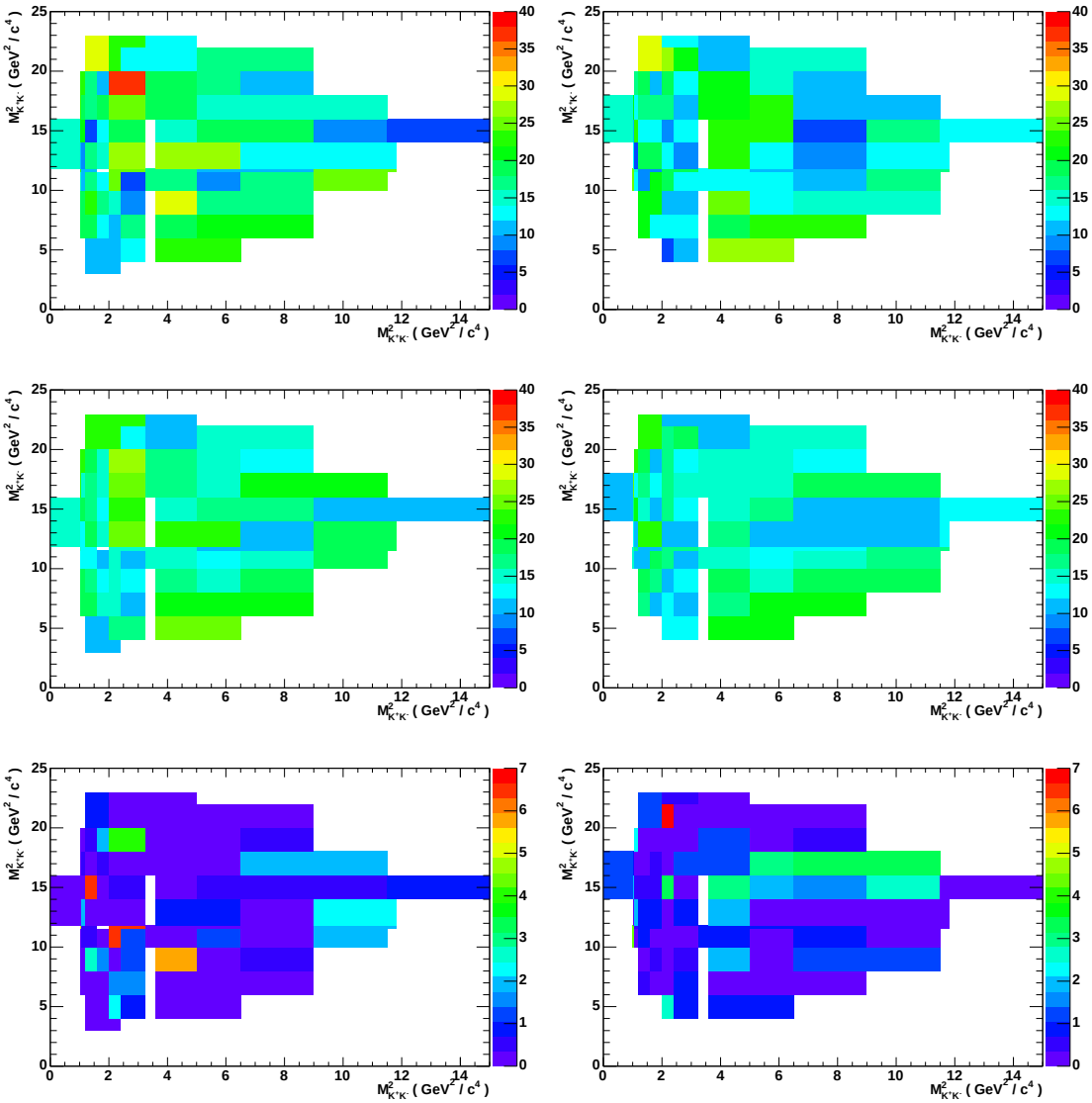

Figure 5.5: *This Figure attempts to illustrate the goodness of the fit across the Dalitz plot. The top row shows the distribution of the data for the two datasets. B^+ is shown in the left column and B^- in the right column. The centre row shows the toy MC generated from the fit. The bottom row shows the χ^2 distribution across the Dalitz plot, resulting from the differences between the top two rows.*

5.4 Cross-checks

The nominal model detailed in earlier sections was deemed the best model after various cross-checks against alternative models had been performed. Various Monte Carlo tests of the nominal model are also detailed in this section.

5.4.1 Removal of components from the signal model

To test the stability of the various components and also to show that the fit is better with each of them included a series of "omission tests" were carried out. This entails removing a single component from the fit and then fitting the data. When removing the nonresonant component the $\phi(1020)$ is instead set to be fixed. The results of this test on the B^+ and B^- datasets are show in Tables 5.5 and 5.6.

The $\phi(1020)$, $\phi(1680)$ and $(KK)^0_0$ give very stable results. The χ_{c0} is stable within the A and B multiple solutions. The $f_0(980)$ is unstable on removal of the nonresonant or $\phi(1020)$ component. This is understandable though as all three peak toward the edge of the Dalitz plot. The nonresonant component is the least stable, but is also the only component that fully overlaps every other component in the fit.

5.4.2 Inclusion of additional components in the signal model

To test whether any extra resonances contribute to the Dalitz plot some additional resonances are considered. Each extra resonance is added in turn to the nominal signal model and a fit to both B^+ and B^- datasets is made. The results of these "addition tests" are shown in Tables 5.7 and 5.8.

None of the higher f mesons are seen to contribute to the plot. The $f_0(1370)$ and

	Nominal	No Nonresonant	No χ_{c0}	No $\phi(1020)$	No $f_0(980)$	No $(KK)^0_0$	No $\phi(1680)$
$-\ln\mathcal{L} + \ln\mathcal{L}$(Nominal)	0	135.5	25.5	77.3	15.5	31.5	2.5
Nonresonant Fraction (%)	54.25 ± 5.70	—	69.79 ± 4.77	70.20 ± 7.75	80.86 ± 2.79	33.09 ± 6.40	52.49 ± 5.28
Nonresonant Magnitude	1.00 FIXED	—	1.00 FIXED	1.00 FIXED	1.00 FIXED	1.00 FIXED	1.00 FIXED
Nonresonant Phase	0.00 FIXED	—	0.00 FIXED	0.00 FIXED	0.00 FIXED	0.00 FIXED	0.00 FIXED
χ_{c0} Fraction (%)	4.49 ± 1.37	5.78 ± 1.46	—	4.37 ± 1.61	4.64 ± 1.08	4.46 ± 1.67	4.53 ± 1.37
χ_{c0} Magnitude	0.28 ± 0.05	0.36 ± 0.04	—	0.25 ± 0.04	0.24 ± 0.03	0.37 ± 0.06	0.29 ± 0.05
χ_{c0} Phase	$+0.12 \pm 0.33$	$+1.26 \pm 0.29$	—	-0.13 ± 0.58	$+0.45 \pm 0.67$	$+0.24 \pm 0.36$	$+0.14 \pm 0.32$
$\phi(1020)$ Fraction (%)	11.23 ± 2.82	9.86 ± 1.29	11.38 ± 2.12	—	13.48 ± 1.58	10.70 ± 2.61	11.46 ± 2.49
$\phi(1020)$ Magnitude	0.46 ± 0.06	0.46 FIXED	0.40 ± 0.04	—	0.41 ± 0.03	0.57 ± 0.05	0.47 ± 0.05
$\phi(1020)$ Phase	-2.99 ± 0.47	-2.99 FIXED	$+3.13 \pm 0.25$	—	-1.75 ± 0.14	-2.36 ± 0.33	-2.94 ± 0.39
$f_0(980)$ Fraction (%)	23.34 ± 8.09	49.85 ± 5.08	28.89 ± 5.63	64.75 ± 8.90	—	18.33 ± 5.05	21.52 ± 6.73
$f_0(980)$ Magnitude	0.66 ± 0.15	1.04 ± 0.09	0.64 ± 0.07	0.96 ± 0.06	—	0.75 ± 0.14	0.64 ± 0.14
$f_0(980)$ Phase	$+2.21 \pm 0.42$	$+1.32 \pm 0.16$	$+1.99 \pm 0.20$	$+1.62 \pm 0.15$	—	-3.02 ± 0.41	$+2.29 \pm 0.38$
$(KK)^0_0$ Fraction (%)	9.91 ± 2.21	13.93 ± 2.78	11.34 ± 2.39	11.53 ± 2.72	13.78 ± 2.24	—	9.35 ± 2.06
$(KK)^0_0$ Magnitude	0.43 ± 0.05	0.55 ± 0.06	0.40 ± 0.04	0.41 ± 0.05	0.42 ± 0.03	—	0.42 ± 0.05
$(KK)^0_0$ Phase	-0.84 ± 0.27	$+1.61 \pm 0.20$	-0.83 ± 0.18	-1.36 ± 0.22	-0.19 ± 0.13	—	-0.86 ± 0.23
$\phi(1680)$ Fraction (%)	0.74 ± 0.66	0.50 ± 0.57	0.67 ± 0.62	1.82 ± 1.06	0.60 ± 0.57	0.66 ± 0.59	—
$\phi(1680)$ Magnitude	0.12 ± 0.05	0.11 ± 0.06	0.10 ± 0.05	0.16 ± 0.05	0.09 ± 0.04	0.14 ± 0.06	—
$\phi(1680)$ Phase	-0.27 ± 0.52	0.55 ± 0.61	-0.30 ± 0.56	-1.16 ± 0.36	-0.04 ± 0.64	-0.76 ± 0.46	—

Table 5.5: *Omission test results for the B^+ fit. The mean of the A and B solutions is given in each case, except where the χ_{c0} is omitted. (All errors are statistical only and come from the* `Minuit` *fit)*

	Nominal	No Nonresonant	No χ_{c0}	No $\phi(1020)$	No $f_0(980)$	No $(KK)^0_0$	No $\phi(1680)$
$-\ln\mathcal{L} + \ln\mathcal{L}$(Nominal)	0	103.4	36.2	98.9	24.0	30.7	10.9
Nonresonant Fraction (%)	51.75 ± 3.69	—	64.79 ± 4.51	71.49 ± 9.26	70.75 ± 2.27	34.89 ± 4.12	46.28 ± 3.50
Nonresonant Magnitude	1.00 FIXED	—	1.00 FIXED	1.00 FIXED	1.00 FIXED	1.00 FIXED	1.00 FIXED
Nonresonant Phase	0.00 FIXED	—	0.00 FIXED	0.00 FIXED	0.00 FIXED	0.00 FIXED	0.00 FIXED
χ_{c0} Fraction (%)	5.04 ± 1.67	5.54 ± 1.38	—	4.89 ± 1.82	5.18 ± 1.26	5.06 ± 1.63	5.01 ± 1.71
χ_{c0} Magnitude	0.31 ± 0.05	0.36 ± 0.04	—	0.26 ± 0.04	0.27 ± 0.03	0.38 ± 0.05	0.33 ± 0.05
χ_{c0} Phase	$+0.05 \pm 0.27$	$+0.52 \pm 0.30$	—	-0.22 ± 0.27	$+0.48 \pm 0.30$	$+0.11 \pm 0.29$	$+0.03 \pm 0.27$
$\phi(1020)$ Fraction (%)	13.02 ± 2.52	11.49 ± 1.35	13.05 ± 2.34	—	15.80 ± 1.75	12.38 ± 2.35	13.83 ± 2.58
$\phi(1020)$ Magnitude	0.51 ± 0.05	0.51 FIXED	0.45 ± 0.04	—	0.48 ± 0.03	0.60 ± 0.05	0.55 ± 0.05
$\phi(1020)$ Phase	$+2.97 \pm 0.25$	+2.97 FIXED	$+2.85 \pm 0.22$	—	-2.01 ± 0.14	-2.88 ± 0.26	$+3.00 \pm 0.24$
$f_0(980)$ Fraction (%)	26.47 ± 4.96	43.79 ± 4.74	31.47 ± 5.22	72.61 ± 10.56	—	23.23 ± 4.12	24.53 ± 5.06
$f_0(980)$ Magnitude	0.72 ± 0.08	1.00 ± 0.08	0.70 ± 0.06	1.01 ± 0.06	—	0.82 ± 0.11	0.73 ± 0.10
$f_0(980)$ Phase	$+1.96 \pm 0.23$	-0.965 ± 0.17	$+1.80 \pm 0.17$	$+1.36 \pm 0.12$	—	$+2.74 \pm 0.28$	$+2.07 \pm 0.25$
$(KK)^0_0$ Fraction (%)	8.64 ± 1.88	17.48 ± 3.09	8.68 ± 1.87	10.13 ± 2.45	11.29 ± 1.92	—	8.57 ± 1.88
$(KK)^0_0$ Magnitude	0.41 ± 0.05	0.63 ± 0.06	0.37 ± 0.04	0.38 ± 0.05	0.40 ± 0.04	—	0.43 ± 0.05
$(KK)^0_0$ Phase	-1.38 ± 0.23	$+1.16 \pm 0.20$	-1.40 ± 0.22	-2.09 ± 0.27	-0.53 ± 0.15	—	-1.47 ± 0.26
$\phi(1680)$ Fraction (%)	2.39 ± 1.05	1.75 ± 1.04	2.26 ± 0.97	4.54 ± 1.63	2.22 ± 1.07	2.68 ± 1.13	—
$\phi(1680)$ Magnitude	0.22 ± 0.05	0.20 ± 0.05	0.19 ± 0.04	0.26 ± 0.04	0.18 ± 0.04	0.28 ± 0.06	—
$\phi(1680)$ Phase	-1.16 ± 0.30	-0.48 ± 0.40	-1.22 ± 0.30	-1.86 ± 0.23	-0.59 ± 0.32	-1.23 ± 0.28	—

Table 5.6: *Omission test results for the B^- fit. The mean of the A and B solutions is given in each case, except where the χ_{c0} is omitted. (All errors are statistical only and come from the* `Minuit` *fit)*

$\phi(1850)$ were also considered for this test, but the $f_0(1370)$'s mass and width were deemed to be too unknown (1.2-1.5 GeV and 200-500 MeV) to reliably test for, and also it isn't expected to be present in the fit (see Section 4.6.1). The $\phi(1850)$ falls exactly in the middle of the D^0 veto.

5.4.3 Toy Monte Carlo fit-bias study

To search for any biases in the fitting procedure large samples of toy MC were generated and fitted using `Laura++`. The fit results with the best likelihood were used to generate 500 sets of 1058 events for the B^+ model and 500 sets of 1014 events for B^-, including the appropriate numbers of background events. The initial parameters for the fits were set to be the generated values and a fit to each sample is performed. This ensured that the correct minimum is found, so avoiding the problems with multiple solutions.

The "pull" on a component is the difference between the generated value and the fitted value divided by the statistical error of the fit. If the fit shows no bias the pull distribution for a component should be a Gaussian of width 1σ which is centred on zero. If the width is less than 1σ it shows that the statistical error is too large, and similarly a large width shows that the error is underestimated. The pull distributions for the fit fractions show such non-unity widths for the reasons discussed in Section 5.3. The magnitude and phase pull distributions can be seen in Figures 5.6 and 5.7. The numbers for the pull means and widths are shown in Table 5.9.

Most fit components show a pull of between 0.1 and 0.25σ indicating multiple small biases. The root cause of the bias is unknown and the observation of problems for all components is unique to the $K^{\pm}K^{\mp}K^{\pm}$ Dalitz plot. Previous studies using `Laura++` indicated only small levels of bias effecting only the smaller components in the fits [32], [33].

	Nominal	Add $f_2(1270)$	Add $f_2'(1525)$	Add $f_0(1710)$
$-\ln\mathcal{L} + \ln\mathcal{L}$(Nominal)	0	-0.2	-1.1	-5.0
Nonresonant Fraction (%)	54.25 ± 5.70	52.98 ± 5.43	53.39 ± 5.63	53.76 ± 5.31
Nonresonant Magnitude	1.00 FIXED	1.00 FIXED	1.00 FIXED	1.00 FIXED
Nonresonant Phase	0.00 FIXED	0.00 FIXED	0.00 FIXED	0.00 FIXED
χ_{c0} Fraction (%)	4.49 ± 1.37	4.52 ± 1.40	4.54 ± 1.39	4.54 ± 1.47
χ_{c0} Magnitude	0.28 ± 0.05	0.29 ± 0.05	0.29 ± 0.05	0.29 ± 0.05
χ_{c0} Phase	$+0.12 \pm 0.33$	$+0.12 \pm 0.33$	$+0.14 \pm 0.33$	$+0.09 \pm 0.36$
$\phi(1020)$ Fraction (%)	11.23 ± 2.82	11.29 ± 2.65	11.34 ± 2.64	11.17 ± 2.64
$\phi(1020)$ Magnitude	0.46 ± 0.06	0.47 ± 0.05	0.47 ± 0.05	0.46 ± 0.05
$\phi(1020)$ Phase	-2.99 ± 0.47	-2.94 ± 0.44	-2.93 ± 0.44	-3.00 ± 0.36
$f_0(980)$ Fraction (%)	23.34 ± 8.09	22.24 ± 7.14	22.14 ± 7.32	24.53 ± 6.32
$f_0(980)$ Magnitude	0.66 ± 0.15	0.65 ± 0.14	0.64 ± 0.15	0.68 ± 0.12
$f_0(980)$ Phase	$+2.21 \pm 0.42$	$+2.26 \pm 0.41$	$+2.27 \pm 0.41$	$+2.30 \pm 0.34$
$(KK)_0^0$ Fraction (%)	9.91 ± 2.21	9.72 ± 2.22	9.70 ± 2.34	8.34 ± 2.89
$(KK)_0^0$ Magnitude	0.43 ± 0.05	0.43 ± 0.05	0.43 ± 0.05	0.39 ± 0.07
$(KK)_0^0$ Phase	-0.84 ± 0.27	-0.83 ± 0.25	-0.78 ± 0.26	-0.83 ± 0.31
$\phi(1680)$ Fraction (%)	0.74 ± 0.66	0.75 ± 0.68	0.82 ± 0.72	2.80 ± 1.38
$\phi(1680)$ Magnitude	0.12 ± 0.05	0.12 ± 0.05	0.13 ± 0.05	0.23 ± 0.06
$\phi(1680)$ Phase	-0.27 ± 0.52	-0.23 ± 0.54	-0.16 ± 0.55	$+0.77 \pm 0.32$
Additional Fraction (%)	—	0.05 ± 0.28	0.13 ± 0.27	4.81 ± 2.80
Additional Magnitude	—	0.03 ± 0.07	0.05 ± 0.05	0.30 ± 0.08
Additional Phase	—	-0.42 ± 3.71	$+0.95 \pm 0.99$	$+1.31 \pm 0.28$

Table 5.7: *Addition test results for the B^+ fit. The mean of the A and B solutions is given for each component. (All errors are statistical only and come from the* `Minuit` *fit)*

	Nominal	Add $f_2(1270)$	Add $f_2'(1525)$	Add $f_0(1710)$
$-\ln\mathcal{L} + \ln\mathcal{L}$(Nominal)	0	-2.7	-4.9	-1.5
Nonresonant Fraction (%)	51.75 ± 3.69	55.03 ± 4.10	48.82 ± 3.35	49.17 ± 5.17
Nonresonant Magnitude	1.00 FIXED	1.00 FIXED	1.00 FIXED	1.00 FIXED
Nonresonant Phase	0.00 FIXED	0.00 FIXED	0.00 FIXED	0.00 FIXED
χ_{c0} Fraction (%)	5.04 ± 1.67	5.03 ± 1.67	5.04 ± 1.71	5.08 ± 1.86
χ_{c0} Magnitude	0.31 ± 0.05	0.30 ± 0.04	0.32 ± 0.05	0.32 ± 0.05
χ_{c0} Phase	$+0.05 \pm 0.27$	$+0.05 \pm 0.27$	$+0.06 \pm 0.27$	$+0.04 \pm 0.27$
$\phi(1020)$ Fraction (%)	13.02 ± 2.52	12.90 ± 2.53	13.18 ± 2.56	13.03 ± 2.91
$\phi(1020)$ Magnitude	0.51 ± 0.05	0.49 ± 0.05	0.52 ± 0.05	0.52 ± 0.06
$\phi(1020)$ Phase	$+2.97 \pm 0.25$	$+2.91 \pm 0.25$	$+3.12 \pm 0.27$	$+3.04 \pm 0.24$
$f_0(980)$ Fraction (%)	26.47 ± 4.96	27.57 ± 5.08	23.34 ± 4.85	25.23 ± 5.35
$f_0(980)$ Magnitude	0.72 ± 0.08	0.71 ± 0.08	0.69 ± 0.09	0.72 ± 0.08
$f_0(980)$ Phase	$+1.96 \pm 0.23$	$+1.90 \pm 0.23$	$+2.07 \pm 0.27$	$+2.08 \pm 0.24$
$(KK)_0^0$ Fraction (%)	8.64 ± 1.88	9.03 ± 1.92	8.75 ± 1.91	7.08 ± 2.63
$(KK)_0^0$ Magnitude	0.41 ± 0.05	0.41 ± 0.05	0.42 ± 0.05	0.38 ± 0.08
$(KK)_0^0$ Phase	-1.38 ± 0.23	-1.37 ± 0.22	-1.23 ± 0.24	-1.56 ± 0.30
$\phi(1680)$ Fraction (%)	2.39 ± 1.05	2.32 ± 1.02	2.21 ± 1.04	2.45 ± 1.16
$\phi(1680)$ Magnitude	0.22 ± 0.05	0.21 ± 0.05	0.22 ± 0.05	0.22 ± 0.05
$\phi(1680)$ Phase	-1.16 ± 0.30	-1.19 ± 0.30	-0.93 ± 0.33	-1.12 ± 0.33
Additional Fraction (%)	—	0.34 ± 0.34	1.43 ± 1.01	1.10 ± 1.41
Additional Magnitude	—	0.08 ± 0.04	0.17 ± 0.06	0.15 ± 0.09
Additional Phase	—	-2.93 ± 1.18	-0.52 ± 0.29	$+0.98 \pm 0.53$

Table 5.8: *Addition test results for the B^- fit. The mean of the A and B solutions is given for each component. (All errors are statistical only and come from the* `Minuit` *fit)*

	B^+		B^-	
	Pull Mean	Pull Sigma	Pull Mean	Pull Sigma
$f_0(980)$ Magnitude	0.249 ± 0.053	1.069 ± 0.046	0.235 ± 0.047	0.926 ± 0.039
$f_0(980)$ Phase	-0.263 ± 0.059	1.134 ± 0.052	-0.299 ± 0.045	1.014 ± 0.032
$\phi(1020)$ Magnitude	-0.155 ± 0.050	1.007 ± 0.040	-0.147 ± 0.052	1.007 ± 0.045
$\phi(1020)$ Phase	-0.293 ± 0.047	1.061 ± 0.034	-0.178 ± 0.045	1.002 ± 0.031
$(KK)^0_0$ Magnitude	0.119 ± 0.044	0.974 ± 0.031	0.167 ± 0.043	0.956 ± 0.030
$(KK)^0_0$ Phase	-0.005 ± 0.051	1.015 ± 0.047	-0.022 ± 0.044	0.974 ± 0.031
$\phi(1680)$ Magnitude	0.262 ± 0.040	0.879 ± 0.028	0.091 ± 0.045	0.996 ± 0.032
$\phi(1680)$ Phase	-0.098 ± 0.051	1.034 ± 0.048	-0.110 ± 0.046	1.030 ± 0.030
χ_{c0} Magnitude	-0.225 ± 0.050	0.996 ± 0.049	0.043 ± 0.046	1.016 ± 0.032
χ_{c0} Phase	-0.096 ± 0.047	1.051 ± 0.033	-0.023 ± 0.046	1.010 ± 0.030

Table 5.9: *Magnitude and Phase pulls from toy MC generated from the best fit.*

Many tests were carried out, attempting to understand the problem. They included:

- ◇ Using 10,000 experiments rather than 500.
- ◇ Setting different components to be the fixed component.
- ◇ Using more basic signal models, starting with only 2 components.
- ◇ Cutting lineshapes at 5σ (normally there is no cut).
- ◇ Generating the integration from toy MC rather than a numerical method.
- ◇ Using normal Dalitz plot background histograms rather than square ones.
- ◇ Setting the $f_0(980)$ mass to $1.1\,\mathrm{GeV}/c^2$, so that the Flatté peaks within the Dalitz plot.
- ◇ Trying each of the different nonresonant models (Taylor, Exponential and flat).

Each test requires the generation of roughly half a million toy MC events, meaning that only two tests could be done per day. After doing the above tests for a few weeks and getting no closer to pin-pointing the cause of the problem it was decided to be impractical to solve in within a reasonable time scale.

Instead the biases are taken into account via an extra systematic error on each component. This error is taken to be the difference between the data fitted value and the mean of the toy distribution. Extra toy MC was generated and fitted to get results for the second best fits on the B^+ and B^- datasets. Toy distribution means are shown in Tables 5.10-5.12.

5.4.4 Full Monte Carlo tests

Migration studies showed that the experimental resolution should only have a small effect upon the position of events in the Dalitz plot. To check that the fit returns correct results despite neglecting this effect samples of fully simulated MC were tested. As the process for getting specific sets of MC generated at *BABAR* involves a long waiting period it was decided to instead reweight a sample of 1.314 million $B^\pm \to K^\pm K^\mp K^\pm$ nonresonant MC events. `Laura++` was used to generate an amplitude model and then select events based upon the position at which they were generated (taken from MC truth information). Toy MC generated from the $q\overline{q}$ and $B\overline{B}$ background models was then added in appropriate fractions.

Seven samples were generated according to the best handful of results for both B^+ and B^- datasets (see Section 5.3.1). Each sample contained only $\sim$500 events due to difficulties encountered finding enough events to make up the $\phi(1020)$.

The results of these tests can be seen in Tables 5.13-5.19. All samples show both results for the χ_{c0} indicating that the model cannot distinguish between the two.

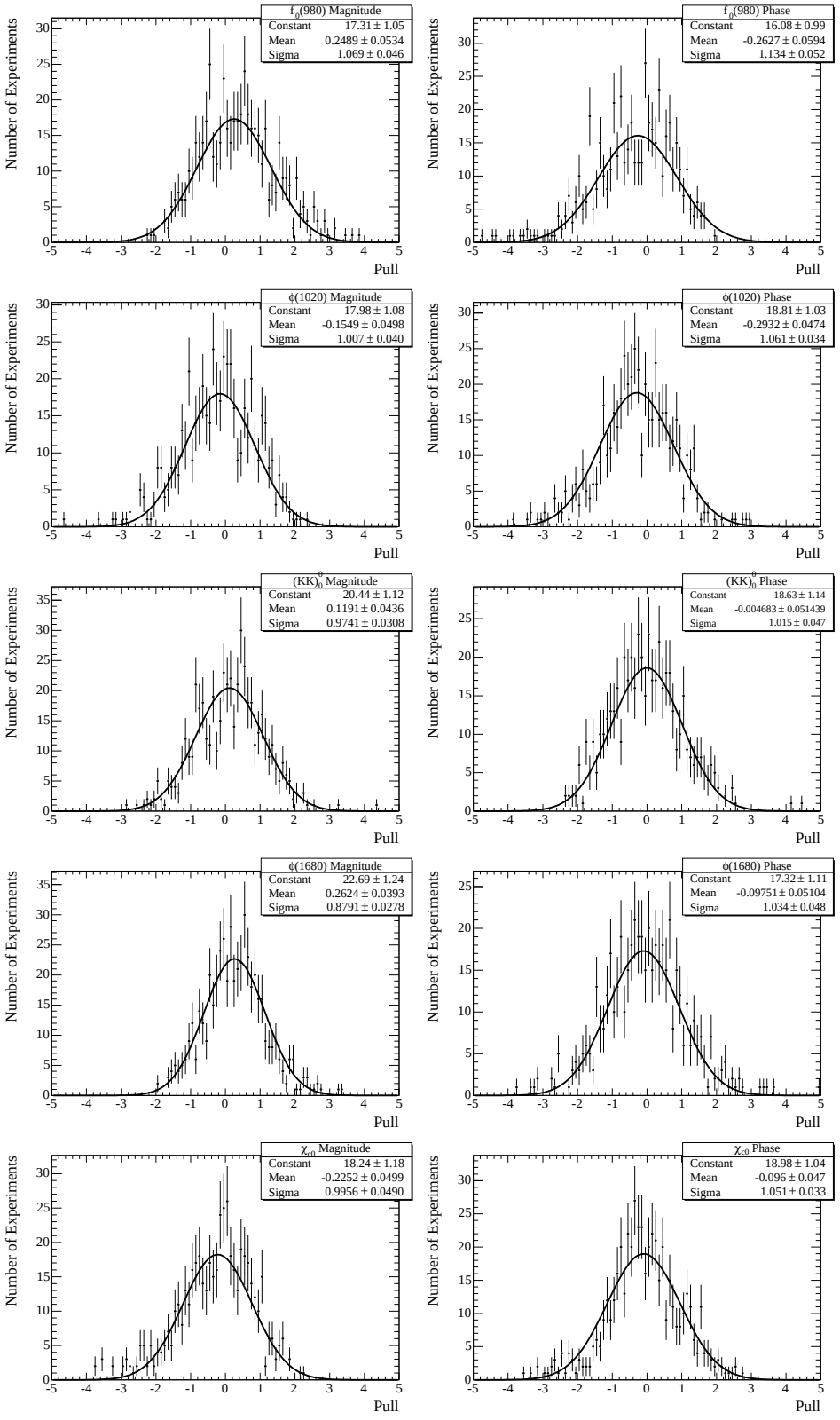

Figure 5.6: *B^+ pull plots. The left-hand column shows magnitude pulls and the right is phase pulls. Top row is $f_0(980)$, second is $\phi(1020)$, middle is $(KK)^0_0$, second bottom is $\phi(1680)$ and the bottom row shows χ_{c0}.*

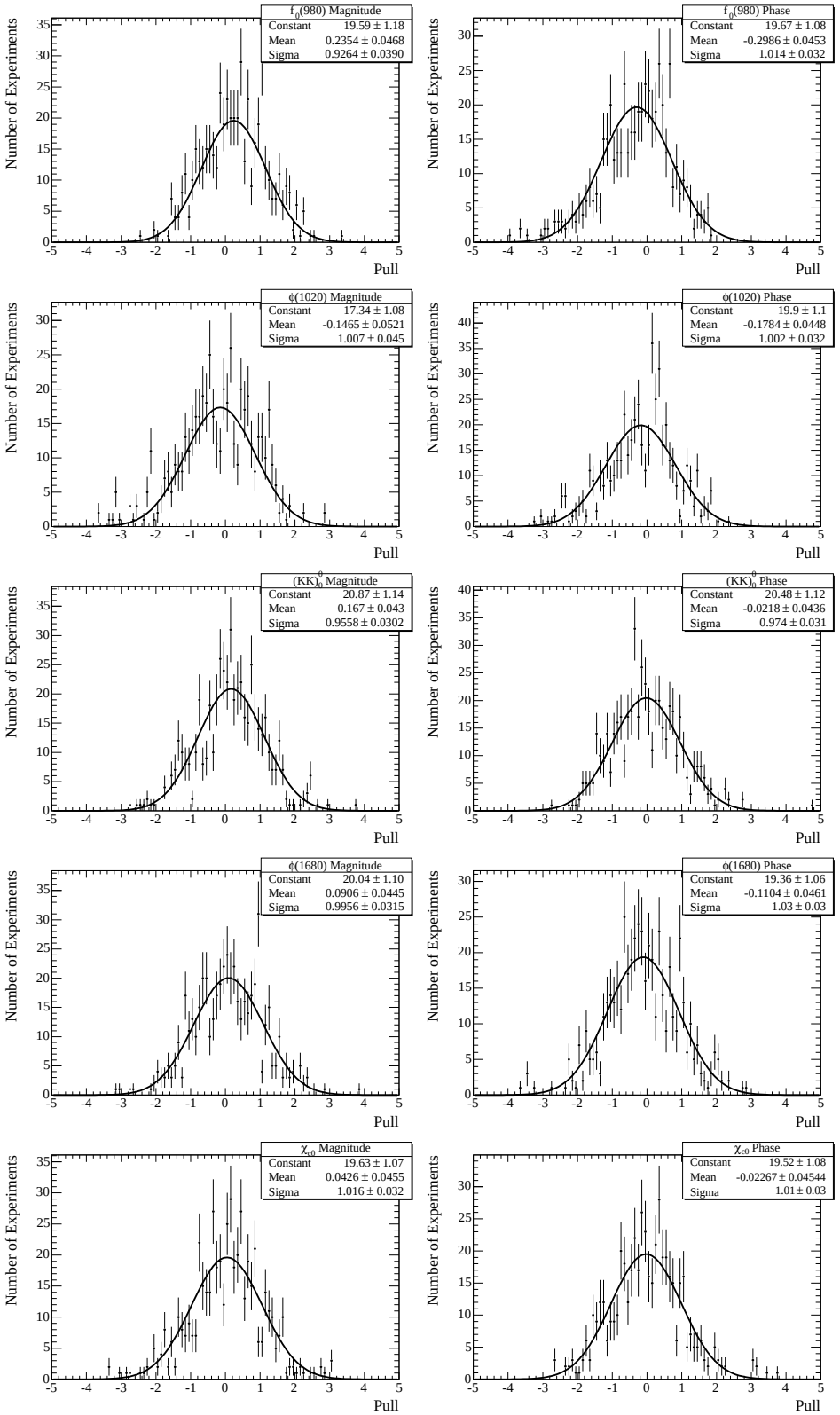

Figure 5.7: *B^- pull plots. The left-hand column shows magnitude pulls and the right is phase pulls. Top row is $f_0(980)$, second is $\phi(1020)$, middle is $(KK)^0_0$, second bottom is $\phi(1680)$ and the bottom row shows χ_{c0}.*

	B^+ Best Fit		B^+ 2nd Best Fit	
	Mean	Width	Mean	Width
Nonresonant Fit Fraction (%)	58.09 ± 0.49	9.54 ± 0.44	53.70 ± 0.42	8.22 ± 0.40
$f_0(980)$ Fit Fraction (%)	27.93 ± 0.41	8.07 ± 0.41	24.39 ± 0.45	8.64 ± 0.44
$\phi(1020)$ Fit Fraction (%)	10.773 ± 0.074	1.437 ± 0.068	11.183 ± 0.072	1.401 ± 0.070
$(KK)^0_0$ Fit Fraction (%)	11.48 ± 0.15	3.01 ± 0.13	9.93 ± 0.15	2.85 ± 0.13
$\phi(1680)$ Fit Fraction (%)	0.924 ± 0.040	0.679 ± 0.053	0.687 ± 0.082	0.827 ± 0.081
χ_{c0} Fit Fraction (%)	5.532 ± 0.065	1.235 ± 0.062	3.116 ± 0.052	0.923 ± 0.053

Table 5.10: *B^+ Fit Fraction distribution means and widths from toy MC samples using the nominal fit results.*

	B^- Best Fit		B^- 2nd Best Fit	
	Mean	Width	Mean	Width
Nonresonant Fit Fraction (%)	52.25 ± 0.47	8.61 ± 0.51	52.26 ± 0.46	9.04 ± 0.45
$f_0(980)$ Fit Fraction (%)	30.01 ± 0.40	7.38 ± 0.37	26.78 ± 0.40	7.65 ± 0.41
$\phi(1020)$ Fit Fraction (%)	12.757 ± 0.093	1.691 ± 0.086	13.025 ± 0.068	1.349 ± 0.068
$(KK)^0_0$ Fit Fraction (%)	8.87 ± 0.12	2.15 ± 0.12	9.71 ± 0.14	2.48 ± 0.14
$\phi(1680)$ Fit Fraction (%)	2.557 ± 0.062	1.160 ± 0.053	2.784 ± 0.062	1.171 ± 0.057
χ_{c0} Fit Fraction (%)	3.372 ± 0.039	0.765 ± 0.039	6.406 ± 0.064	1.262 ± 0.065

Table 5.11: *B^- Fit Fraction distribution means and widths from toy MC samples using the nominal fit results.*

	B^+ Best Fit	B^+ 2nd Best Fit	B^- Best Fit	B^- 2nd Best Fit
$f_0(980)$ Phase	2.104 ± 0.012	2.222 ± 0.013	1.863 ± 0.010	1.974 ± 0.010
$\phi(1020)$ Phase	-3.074 ± 0.014	-3.012 ± 0.016	2.851 ± 0.011	2.992 ± 0.012
$(KK)^0_0$ Phase	-0.851 ± 0.010	-0.833 ± 0.010	-1.498 ± 0.010	-1.285 ± 0.010
$\phi(1680)$ Phase	-0.268 ± 0.027	-0.312 ± 0.015	-1.223 ± 0.014	-1.169 ± 0.013
χ_{c0} Phase	0.551 ± 0.012	-0.349 ± 0.018	-0.532 ± 0.015	0.624 ± 0.009

Table 5.12: *Phase distribution means from toy MC samples using the nominal fit results.*

Otherwise most components are fitted quite well considering the low statistics. Perhaps most reassuring is that the leading solutions (Tables 5.13 and 5.16) are the most stable. The $f_0(980)$ phase is the most commonly poorly fitted component. However, because systematic uncertainties are not calculated for these tests the effect looks worse than it really is. One other point to note is that the phases wrap around at $\pm\pi$, thus explaining some of the $\phi(1020)$ phase results.

5.5 Systematic Uncertainty

To calculate the systematic uncertainty on each component of the Dalitz fit seven factors are studied:

- ◇ the $B\overline{B}$ background fraction.
- ◇ the $B\overline{B}$ background distribution histogram.
- ◇ the $q\overline{q}$ background fraction.
- ◇ the $q\overline{q}$ background distribution histogram.
- ◇ the efficiency histogram.
- ◇ the fit bias.
- ◇ the model dependency.

This section details the studies made of each factor. The results table (Table 5.1) shows the full systematic uncertainty for each component, which is generated by summing in quadrature the uncertainties for the seven factors listed above.

NLL	χ_{c0}Mag	χ_{c0}Pha	$\phi(1020)$M	$\phi(1020)$Pha	$f_0(980)$M	$f_0(980)$Pha	$(KK)^0_0$M	$(KK)^0_0$Pha	$\phi(1680)$M	$\phi(1680)$Pha	#Fits
Generated:	0.32	0.60	0.45	-3.04	0.66	2.13	0.45	-0.82	0.13	-0.13	—
3015.3	0.20±0.05	-1.17±0.42	0.45±0.06	1.94±0.40	0.60±0.09	1.26±0.18	0.43±0.08	-0.32±0.30	0.16±0.07	-0.38±0.50	17/200
3016.4	0.31±0.05	0.96±0.31	0.46±0.06	2.07±0.45	0.57±0.09	1.34±0.21	0.44±0.10	-0.17±0.34	0.16±0.07	-0.34±0.50	174/200

Table 5.13: *Magnitude and Phase results for the reweighted Monte Carlo test based on the best Likelihood fit for the B^+ sample. The experiment used 384 signal events, 18 $B\overline{B}$ and 133 $q\overline{q}$ events.*

NLL	χ_{c0}Mag	χ_{c0}Pha	$\phi(1020)$M	$\phi(1020)$Pha	$f_0(980)$M	$f_0(980)$Pha	$(KK)^0_0$M	$(KK)^0_0$Pha	$\phi(1680)$M	$\phi(1680)$Pha	#Fits
Generated:	0.24	-0.95	0.47	-3.02	0.65	2.25	0.44	-0.82	0.13	-0.17	—
2992.4	0.23±0.05	-0.95±0.40	0.43±0.06	2.11±0.40	0.71±0.09	1.36±0.20	0.43±0.10	-0.31±0.34	0.11±0.07	-0.65±0.64	39/200
2994.0	0.33±0.06	0.41±0.50	0.46±0.07	2.38±0.47	0.70±0.10	1.58±0.25	0.57±0.15	0.11±0.33	0.11±0.07	-0.67±0.56	134/200
2998.3	0.29±0.05	0.84±0.36	0.39±0.06	0.60±0.65	0.55±0.10	0.55±0.35	0.44±0.08	0.91±0.39	0.12±0.07	-1.13±0.56	16/200

Table 5.14: *Magnitude and phase results for the reweighted Monte Carlo test based on the second best Likelihood fit to the B^+ sample. The experiment used 377 signal events, 18 $B\overline{B}$ and 131 $q\overline{q}$ events.*

NLL	χ_{c0}Mag	χ_{c0}Pha	$\phi(1020)$M	$\phi(1020)$Pha	$f_0(980)$M	$f_0(980)$Pha	$(KK)^0_0$M	$(KK)^0_0$Pha	$\phi(1680)$M	$\phi(1680)$Pha	#Fits
Generated:	0.29	0.46	0.40	-2.93	0.73	2.22	1.07	0.56	0.10	0.43	—
3303.8	0.20±0.04	-1.15±0.41	0.40±0.05	2.29±0.38	0.68±0.08	1.44±0.17	0.55±0.09	-0.21±0.26	0.11±0.06	-0.28±0.61	97/200
3304.6	0.31±0.05	0.70±0.28	0.42±0.05	2.53±0.44	0.65±0.09	1.62±0.21	0.68±0.11	0.18±0.20	0.10±0.07	-0.18±0.70	93/200
3308.4	0.28±0.04	1.05±0.26	0.35±0.05	0.33±0.47	0.52±0.08	0.49±0.23	0.54±0.07	0.94±0.24	0.08±0.06	-1.10±0.74	7/200

Table 5.15: *Magnitude and phase results for the reweighted Monte Carlo test based on the third best Likelihood fit to the B^+ sample. The experiment used 414 signal events, 20 $B\overline{B}$ and 143 $q\overline{q}$ events.*

NLL	χ_{c0}Mag	χ_{c0}Pha	$\phi(1020)$M	$\phi(1020)$Pha	$f_0(980)$M	$f_0(980)$Pha	$(KK)^0_0$M	$(KK)^0_0$Pha	$\phi(1680)$M	$\phi(1680)$Pha	#Fits
Generated:	0.25	-0.52	0.48	2.85	0.72	1.85	0.41	-1.49	0.21	-1.14	—
2736.9	0.27±0.06	-1.12±0.33	0.49±0.07	2.10±0.45	0.65±0.10	1.23±0.20	0.40±0.08	-0.84±0.37	0.18±0.09	-1.00±0.51	79/200
2738.6	0.39±0.07	0.45±0.30	0.52±0.08	2.49±0.53	0.68±0.12	1.61±0.27	0.79±0.14	0.44±0.22	0.02±0.12	0.16±4.87	66/200
2740.2	0.37±0.06	0.63±0.36	0.49±0.07	2.23±0.52	0.61±0.10	1.31±0.26	0.44±0.10	-0.51±0.35	0.20±0.09	-0.91±0.53	52/200

Table 5.16: *Results from the reweighted Monte Carlo fit to the best Likelihood fit to the B^- sample. The experiment used 352 signal events, 15 $B\overline{B}$ and 111 $q\overline{q}$ events.*

NLL	χ_{c0}Mag	χ_{c0}Pha	$\phi(1020)$M	$\phi(1020)$Pha	$f_0(980)$M	$f_0(980)$Pha	$(KK)^0_0$M	$(KK)^0_0$Pha	$\phi(1680)$M	$\phi(1680)$Pha	#Fits
Generated:	0.36	0.70	0.49	3.01	0.67	1.98	0.40	-1.28	0.22	-1.07	—
2647.4	0.38±0.11	-0.99±0.33	0.70±0.15	3.03±0.62	0.66±0.18	1.72±0.41	0.37±0.11	-1.17±0.57	0.17±0.11	-1.68±0.68	82/200
2647.7	0.52±0.13	0.88±0.32	0.72±0.17	-2.91±0.80	0.55±0.23	1.95±0.65	0.38±0.12	-0.91±0.54	0.18±0.11	-1.64±0.67	74/200
2647.8	0.39±0.06	1.08±0.31	0.54±0.08	1.63±0.50	0.56±0.10	0.95±0.29	0.37±0.09	-0.97±0.42	0.26±0.08	-1.17±0.40	15/200
2649.7	0.35±0.09	-1.30±0.38	0.64±0.13	3.04±0.62	0.75±0.17	1.91±0.35	0.94±0.19	0.49±0.24	0.11±0.12	2.84±1.23	6/200
2650.0	0.50±0.12	0.57±0.34	0.69±0.15	-2.85±0.72	0.67±0.21	2.15±0.51	0.96±0.23	0.60±0.32	0.15±0.14	2.98±1.08	6/200

Table 5.17: *Results from the reweighted Monte Carlo fit to the second best Likelihood fit to the B^- sample. The experiment used 343 signal events, 14 $B\overline{B}$ and 108 $q\overline{q}$ events.*

NLL	χ_{c0}Mag	χ_{c0}Pha	$\phi(1020)$M	$\phi(1020)$Pha	$f_0(980)$M	$f_0(980)$Pha	$(KK)^0_0$M	$(KK)^0_0$Pha	$\phi(1680)$M	$\phi(1680)$Pha	#Fits
Generated:	0.19	-1.19	0.38	-0.08	0.40	0.08	0.81	1.58	0.11	2.98	—
2746.6	0.41±0.07	0.94±0.31	0.55±0.09	0.25±0.42	0.54±0.12	0.54±0.27	0.62±0.11	1.55±0.40	0.15±0.12	-2.21±0.57	82/200
2746.7	0.27±0.06	-1.50±0.41	0.51±0.08	0.28±0.42	0.55±0.11	0.60±0.24	0.60±0.10	-1.31±0.36	0.11±0.13	-2.35±0.69	19/200
2747.9	0.43±0.07	1.27±0.29	0.58±0.09	1.17±0.46	0.70±0.10	0.89±0.27	0.33±0.12	-2.24±0.90	0.31±0.08	-1.17±0.39	66/200
2748.2	0.28±0.06	-1.46±0.38	0.54±0.08	1.42±0.43	0.71±0.10	0.98±0.23	0.32±0.09	-1.62±0.71	0.31±0.08	-1.01±0.36	39/200
2751.7	0.26±0.06	-1.25±0.37	0.54±0.10	-2.46±0.62	0.40±0.17	0.72±0.34	0.35±0.09	-0.49±0.41	0.20±0.07	-0.44±0.48	6/200
2752.4	0.39±0.10	1.56±0.33	0.53±0.15	-0.75±0.87	0.44±0.24	0.05±0.55	0.29±0.12	-0.18±0.61	0.22±0.08	-0.51±0.46	6/200

Table 5.18: *Results from the reweighted Monte Carlo fit to the third best Likelihood fit to the B^- sample. The experiment used 358 signal events, 15 $B\overline{B}$ and 112 $q\overline{q}$ events.*

NLL	χ_{c0}Mag	χ_{c0}Pha	$\phi(1020)$M	$\phi(1020)$Pha	$f_0(980)$M	$f_0(980)$Pha	$(KK)^0_0$M	$(KK)^0_0$Pha	$\phi(1680)$M	$\phi(1680)$Pha	#Fits
Generated:	0.35	0.63	0.48	-2.61	0.65	2.45	1.17	0.80	0.16	1.53	—
2802.4	0.44±0.08	-0.71±0.27	0.61±0.09	-2.78±0.51	0.57±0.16	1.99±0.34	0.85±0.15	0.48±0.23	0.08±0.09	2.15±1.80	117/200
2803.4	0.30±0.07	-1.17±0.34	0.59±0.09	3.07±0.44	0.60±0.13	1.61±0.26	0.48±0.10	-0.53±0.36	0.12±0.10	-1.14±0.80	78/200

Table 5.19: *Results from the reweighted Monte Carlo fit to the forth best Likelihood fit to the B^- sample. The experiment used 363 signal events, 15 $B\overline{B}$ and 114 $q\overline{q}$ events.*

5.5.1 Efficiency and Background Histograms

The fit model uses three histograms to describe the $q\overline{q}$ background, $B\overline{B}$ background and efficiency distributions across the Dalitz plot. To calculate systematic uncertainties for the use of these histograms multiple similar histograms are generated and their effect upon the fit results is studied.

Every bin of each histogram has an associated error. For each histogram 100 new histograms are produced by varying its bin contents randomly within the error bounds. The systematic uncertainty on a fit component due to the uncertainty from each histogram is given by the root-mean-square (RMS) of its distribution in the results of fits to the 100 new histograms. Table 5.20 shows the results of this procedure.

5.5.2 Background Fractions

The fit model also uses two numbers setting out the expected fractions of the $q\overline{q}$ and $B\overline{B}$ backgrounds. To calculate a systematic uncertainty for using these numbers 300 fits are made whilst varying the fractions randomly within their error bounds. The uncertainty is then given by the RMS of the distribution of each component. Results of this experiment can be seen in Table 5.20.

5.5.3 Fit Bias

The procedure used to study fit biases is fully described in Section 5.4.3.

In summary 500 sets of toy MC are generated and fitted for both the B^+ and B^- models. Small fit biases are seen in all components. The systematic uncertainty

Uncertainty Source	$B\overline{B}$ Fraction		$B\overline{B}$ Histogram		$q\overline{q}$ Fraction		$q\overline{q}$ Histogram		ϵ Histogram		Fit Bias		Model		Total	
Data Sample	B^+	B^-	B^+	B^-	B^+	B^-	B^+	B^-	B^+	B^-	B^+	B^-	B^+	B^-	B^+	B^-
Nonresonant Fit Fraction (%)	0.281	0.283	0.291	0.380	0.336	0.934	2.020	0.632	0.314	0.610	1.635	0.785	1.280	3.745	2.961	4.063
$f_0(980)$ Fit Fraction (%)	0.336	0.221	0.387	0.477	0.032	0.346	1.993	0.524	0.560	0.497	2.820	1.930	1.430	3.130	3.814	3.800
$f_0(980)$ Phase	0.009	0.008	0.011	0.018	0.005	0.012	0.061	0.018	0.010	0.013	0.047	0.037	0.090	0.130	0.120	0.139
$\phi(1020)$ Fit Fraction (%)	0.052	0.031	0.044	0.213	0.018	0.008	0.150	0.192	0.279	0.244	0.252	0.124	0.110	0.160	0.425	0.429
$\phi(1020)$ Phase	0.010	0.007	0.013	0.018	0.005	0.012	0.076	0.013	0.016	0.015	0.053	0.049	0.060	0.115	0.113	0.128
$(KK)^0_0$ Fit Fraction (%)	0.117	0.198	0.091	0.102	0.052	0.237	0.517	0.209	0.163	0.247	0.795	0.650	1.570	1.560	1.848	1.751
$(KK)^0_0$ Phase	0.003	0.004	0.020	0.013	0.003	0.004	0.064	0.017	0.012	0.012	0.007	0.012	0.060	0.195	0.091	0.197
$\phi(1680)$ Fit Fraction (%)	0.059	0.021	0.074	0.033	0.010	0.017	0.224	0.035	0.057	0.042	0.074	0.286	2.060	0.175	2.076	0.342
$\phi(1680)$ Phase	0.006	0.002	0.033	0.020	0.004	0.017	0.070	0.025	0.016	0.022	0.020	0.041	1.035	0.225	1.038	0.233
χ_{c0} Fit Fraction (%)	0.035	0.014	0.024	0.041	0.021	0.030	0.540	0.036	0.043	0.048	0.172	0.168	0.055	0.100	0.573	0.211
χ_{c0} Phase	0.003	0.003	0.014	0.010	0.003	0.004	0.204	0.010	0.011	0.007	0.015	0.027	0.030	0.040	0.208	0.053
Efficiency (%)	0.007	0.007	0.005	0.007	0.001	0.000	0.020	0.017	0.063	0.062	0.010	0.020	0.045	0.080	0.080	0.106

Table 5.20: *Systematic uncertainties from the Dalitz fit. The uncertainties listed are in the same units as the fit result, i.e. fit fractions are percentages and phases are in radians.*

on a component is taken to be the difference between the fitted data value and the mean of the toy distribution. Toy distribution means are shown in Tables 5.10-5.12. Table 5.20 shows the uncertainties on each component due to fit biases.

5.5.4 Model Dependency

To give an idea of the stability of each component in the fit the differences encountered during the addition tests are studied (see Section 5.4.2). The uncertainty on a component is taken to be the largest difference between the nominal fit and the three addition tests. These uncertainties are shown in Table 5.20.

5.6 Total Rate Measurement

After the event selection described in Chapter 3 2072 events are left in the Signal Box. Of these 1058 are B^+ and 1014 are B^- events. The fractions of signal and background given by the fit to $m_{\rm ES}$ (see Section 4.5.3) are shown in Table 5.21. The distributions of $m_{\rm ES}$ in the Signal Strip is shown by Figure 5.8.

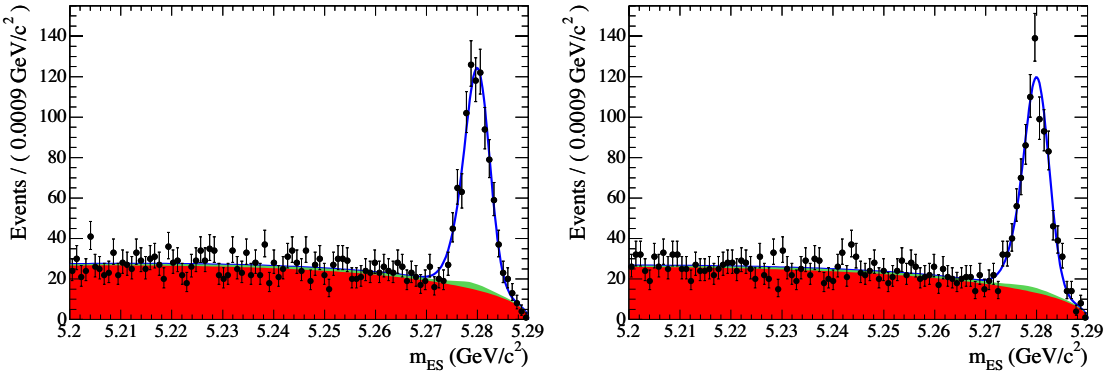

Figure 5.8: *The $m_{\rm ES}$ fits to data events; the blue curve is the total model, the solid red is continuum and the solid green is $B\overline{B}$ background. The left plot shows B^+ events and the right B^-.*

The fits yield the same number of B^+ and B^- signal events giving an overall asymmetry of zero. The combined sample can therefore be used to calculate the branching fraction of $B^\pm \to K^\pm K^\mp K^\pm$ using:

$$\mathcal{B}(B^\pm \to K^\pm K^\mp K^\pm) = \frac{N_{sig}}{\bar{\epsilon}\,\epsilon_c\,N_{B\overline{B}}}, \tag{5.2}$$

where N_{sig} is the number of signal events (given by the fit to $m_{\rm ES}$), $N_{B\overline{B}}$ is the number of $B\overline{B}$ pairs (see Section 3.2.1), $\bar{\epsilon}$ is the average efficiency and ϵ_c is the efficiency correction (see Section 5.7). The result for the total branching fraction is:

$$\mathcal{B}(B^\pm \to K^\pm K^\mp K^\pm) = (35.1 \pm 1.3 \pm 2.1) \times 10^{-6} \tag{5.3}$$

where the first error is statistical and the second systematic.

Category	Combined Sample	B^+ sample	B^- sample
Signal events	1516 ± 46	758 ± 33	758 ± 32
$q\overline{q}$ events	486 ± 19	254 ± 14	231 ± 13
$B\overline{B}$ events	65 ± 7	35 ± 4	31 ± 3
Signal fraction (%)	73 ± 3	72 ± 4	74 ± 4
$q\overline{q}$ fraction (%)	24 ± 1	24 ± 2	23 ± 2
$B\overline{B}$ fraction (%)	3.1 ± 0.3	3.3 ± 0.4	3.0 ± 0.3

Table 5.21: *Results for the fit to $m_{\rm ES}$ in the Signal Strip. The signal and $q\overline{q}$ errors come from the fit, whereas the $B\overline{B}$ error comes from uncertainties with the various efficiencies and branching fractions.*

5.7 Systematic Uncertainties on the Total Rate Measurement

The branching fraction is given by Equation 5.2, where the sources of uncertainty are $N_{B\overline{B}}$, N_{sig}, $\bar{\epsilon}$ and ϵ_c.

The uncertainty on $N_{B\overline{B}}$, the number of $B\overline{B}$ pairs, is 1.1% [68]. The uncertainty on the number of signal events, N_{sig}, is due to the fixed $B\overline{B}$ component in the $m_{\rm ES}$ fit. The error is determined by twice running the $m_{\rm ES}$ fit, once using the lower bound for the number of $B\overline{B}$ events and then using the upper bound. The difference in N_{sig} is almost symmetric about the nominal value for the two extremes. This gives an uncertainty of 0.2%.

The uncertainty on the average efficiency, $\bar{\epsilon}$, is made up of four components:

- ◇ The statistical uncertainty from the Dalitz fit, which is taken from the width of the efficiency distribution in the toy MC tests detailed in Section 5.4.3. This

is 0.5% for both B^+ and B^-.

- ◇ Systematic uncertainty from the histogram and fraction fluctuation tests as detailed in Section 5.5. The overall uncertainty from these sources is 0.5% for both B^+ and B^-.

- ◇ Systematic uncertainty due to tracking efficiency. This was studied in a previous *BABAR* measurement of the $B^\pm \to K^\pm K^\mp K^\pm$ inclusive branching fraction to be 0.8% per track [17], giving a total systematic uncertainty of 2.4% for the three tracks.

- ◇ Systematic uncertainty due to particle identification corrections. This was again studied in the same previous analysis [17]. The uncertainty per selector used was found to be 1.0%. As both a kaon selector and and electron selector were used this totals 1.4% per particle, giving an overall uncertainty of 4.2%.

The efficiency corrections, ϵ_c, are determined by a study of the control channel $B^+ \to \overline{D}^0\pi^+$, where $\overline{D}^0 \to K^+\pi^-$. This decay is preferred over $B^+ \to \overline{D}^0 K^+$ ($\overline{D}^0 \to K^+K^-$) because of its much higher branching fraction of $(189 \pm 12) \times 10^{-6}$ compared with $(1.4 \pm 0.2) \times 10^{-6}$. The difference given by using a channel with a final state of $K^\pm\pi^\mp\pi^\pm$ is assumed to be negligible.

The differences in selection efficiencies between data and a large sample of MC are measured and the correction needed for the MC is calculated. Details of the numbers for each of the selection requirements can be seen in Table 5.22. The uncertainty from ϵ_c is determined to be 3.0%.

Summing these quantities in quadrature gives an overall systematic uncertainty of 5.8% on the total rate. This corresponds to $(35.1 \pm 2.1) \times 10^{-6}$.

Requirement	Data Before	Data After	Data Efficiency	MC Before	MC After	MC Efficiency	Correction
$\cos\theta_{Thr}$	14293	13206	0.924	76770	71435	0.931	0.992 ± 0.013
Fisher	13206	10794	0.817	71435	59261	0.830	0.984 ± 0.014
$m_{\rm ES}$	10794	10814	1.001	59261	59252	1.000	1.001 ± 0.015
ΔE	10814	10363	0.958	59252	57387	0.969	0.989 ± 0.015
Total							0.965 ± 0.029

Table 5.22: *Selection requirement efficiency corrections. The error on the corrections comes from $\sqrt{n}$ for each of the data and MC numbers used. The total correction comes from the multiplication of the four separate corrections, and the uncertainties are summed in quadrature. The overall fractional uncertainty on the correction is 0.030.*

5.8 Upper Limits

For the smaller components, including those covered in the addition tests, 90% confidence upper limits are calculated. To generate the upper limits toy MC experiments are run where the sources of systematic uncertainty are fluctuated as in Section 5.5. A cut is then imposed upon the likelihood distribution of these experiments such that only the most likely 90% remain. The upper limit is then said to be the highest fit fraction of the remaining experiments.

Fit fraction upper limits are shown in Table 5.23. The final branching fraction upper limits, shown in Table 6.2, conservatively use the larger of the B^+ and B^- fit fraction results.

Component	90% Confidence level upper limit	
	B^+	B^-
χ_{c0} Fit Fraction (%)	< 8.2	< 7.8
$\phi(1680)$ Fit Fraction (%)	< 3.8	< 4.2
$f_2(1270)$ Fit Fraction (%)	< 3.2	< 2.8
$f_2'(1525)$ Fit Fraction (%)	< 2.5	< 6.7
$f_0(1710)$ Fit Fraction (%)	< 9.5	< 6.0

Table 5.23: *90% confidence level upper limits on fit fractions.*

6

Discussion and Conclusion

A summary of the fit fraction and phase results is given in Table 6.1. The uncertainty for most components is high. The most notable aspect of the phase results is that they are consistent between charge conjugate states (The fitter wraps phases at $\pm\pi$, thus the $\phi(1020)$ phases are consistent).

The significance of the $\phi(1680)$ is very low in B^+ and quite low in B^-. The main reason behind its inclusion in the nominal fit was that it alleviated some of the problems with multiple results in the B^- fit. The multiple results observed with the χ_{c0} are also seen by the BELLE collaboration's analysis of the $B^\pm \to K^\pm K^\mp K^\pm$

	B^+	B^-	Combined Result
Nonresonant Fraction (%)	$54.3 \pm 9.5 \pm 3.0$	$51.7 \pm 9.0 \pm 4.1$	$53.0 \pm 9.5 \pm 4.1$
Nonresonant Phase	0.0 FIXED	0.0 FIXED	0.0 FIXED
$f_0(980)$ Fraction (%)	$23.3 \pm 8.7 \pm 3.8$	$26.5 \pm 7.7 \pm 3.8$	$24.9 \pm 8.7 \pm 3.8$
$f_0(980)$ Phase	$2.21 \pm 0.41 \pm 0.12$	$1.96 \pm 0.23 \pm 0.15$	$2.08 \pm 0.41 \pm 0.15$
$\phi(1020)$ Fraction (%)	$11.2 \pm 1.4 \pm 0.43$	$13.0 \pm 1.7 \pm 0.43$	$12.1 \pm 1.7 \pm 0.43$
$\phi(1020)$ Phase	$-2.99 \pm 0.46 \pm 0.11$	$2.97 \pm 0.25 \pm 0.13$	$3.13 \pm 0.46 \pm 0.13$
$(KK)_0^0$ Fraction (%)	$9.9 \pm 3.0 \pm 1.8$	$8.6 \pm 2.5 \pm 1.8$	$9.3 \pm 3.0 \pm 1.8$
$(KK)_0^0$ Phase	$-0.84 \pm 0.19 \pm 0.09$	$-1.38 \pm 0.23 \pm 0.20$	$-1.11 \pm 0.23 \pm 0.20$
$\phi(1680)$ Fraction (%)	$0.74 \pm 0.83 \pm 2.1$	$2.4 \pm 1.2 \pm 0.34$	$1.6 \pm 1.2 \pm 2.1$
$\phi(1680)$ Phase	$-0.27 \pm 0.52 \pm 1.0$	$-1.16 \pm 0.30 \pm 0.23$	$-0.71 \pm 0.52 \pm 1.0$
χ_{c0} Mean Fraction (%)	$4.5 \pm 1.2 \pm 0.64$	$5.0 \pm 1.3 \pm 0.34$	$4.8 \pm 1.3 \pm 0.64$
χ_{c0} Phase A	$-0.35 \pm 0.33 \pm 0.21$	$-0.56 \pm 0.26 \pm 0.04$	$-0.46 \pm 0.33 \pm 0.21$
χ_{c0} Phase B	$0.58 \pm 0.21 \pm 0.21$	$0.65 \pm 0.22 \pm 0.06$	$0.62 \pm 0.22 \pm 0.21$

Table 6.1: *Dalitz plot fit results. The first error is statistical and the second is systematic. The mean of the two leading solutions is taken for all components other than the χ_{c0} phase, where both solutions are given. The combined result is the mean of both B^+ and B^- results.*

Dalitz plot [34] and a parallel *BABAR* analysis [69]. Both analyses used different fitting software and different nominal signal models from this analysis and so one can conclude that the multiple solutions problem is independent of these factors.

Also consistent between this analysis and the aforementioned Dalitz analyses is a large, non-uniform nonresonant term and a large, wide, undetermined resonance around $1.5\,\mathrm{GeV}/c$. All three analyses see two solutions for the $(KK)_0^0$ (1500) magnitude, one unphysically large solution and a smaller solution. This analysis is however the only one to favour the smaller solution. However when the same exponential nonresonant model as BELLE is used then the large solution is favoured. The same $1.5\,\mathrm{GeV}/c$ feature is seen in the *BABAR* analysis of $B^0 \to K_S^0 K^+ K^-$ [70].

A paper published in 2005 by Minkowski and Ochs based upon the BELLE results in [34] postulates that the feature around 1.5 GeV/c might be caused by the constructive interference of $f_0(1500)$ and a wide glueball background [71]. Further interference between the glueball and $f_0(980)$ also has the potential to remove the need to use a non-uniform nonresonant model.

Partial branching fractions are calculated by multiplying the fit fractions by the total rate, $(35.1 \pm 1.3 \pm 2.1) \times 10^{-6}$. The statistical and systematic errors are also combined. The branching fraction and asymmetry results are summarised by Table 6.2.

Mode	$\mathcal{B}(B \to \text{Mode})(10^{-6})$	90% CL UL (10^{-6})	A_{CP} (%)
$K^\pm K^\mp K^\pm$ Total	$35.1 \pm 1.3 \pm 2.1$		$0.0 \pm 3.0 \pm 4.2$
$K^\pm K^\mp K^\pm$ nonresonant	$18.6 \pm 3.4 \pm 1.8$		$-2 \pm 13 \pm 5$
$f_0(980)K^\pm$; $f_0(980) \to K^+K^-$	$8.7 \pm 3.1 \pm 1.4$		$6 \pm 21 \pm 11$
$\phi(1020)K^\pm$; $\phi(1020) \to K^+K^-$	$4.3 \pm 0.6 \pm 0.3$		$7.4 \pm 8.0 \pm 2.5$
$(KK)_0^0 K^\pm$; $(KK)_0^0 \to K^+K^-$	$3.3 \pm 1.1 \pm 0.7$		$-7 \pm 25 \pm 14$
$\chi_{c0}K^\pm$; $\chi_{c0} \to K^+K^-$	$1.7 \pm 0.5 \pm 0.1$	< 2.9	$6 \pm 17 \pm 6$
$\phi(1680)K^\pm$; $\phi(1680) \to K^+K^-$		< 1.5	
$f_2(1270)K^\pm$; $f_2(1270) \to K^+K^-$		< 1.1	
$f_2'(1525)K^\pm$; $f_2'(1525) \to K^+K^-$		< 2.4	
$f_0(1710)K^\pm$; $f_0(1710) \to K^+K^-$		< 3.3	

Table 6.2: *Summary of measurements of branching fractions (averaged over charge conjugate states), 90% confidence upper limits on branching fractions and CP asymmetries. The first error is statistical, and the second is systematic.*

Due to the large uncertainties the statistical significance of the $f_0(980)$ and $(KK)_0^0$ branching fractions is low. Upper limits are however not given as any such limit would apply only to this particular signal model, and therefore would be potentially misleading. Section 1.5.1 describes how the BES collaboration's $f_0(980)$ results give

the ratio of $\frac{\mathcal{B}(f_0(980)\to K^+K^-)}{\mathcal{B}(f_0(980)\to\pi^+\pi^-)}$ to be 0.92 ± 0.07. This is consistent with the ratio of our $f_0(980) \to K^+K^-$ measurement and the previous $f_0(980) \to \pi^+\pi^-$ measurement by *BABAR*, which is 0.92 ± 0.41, where the error is given by combining the statistical and systematic errors in quadrature. It is also consistent with the ratio 0.69 ± 0.32 reported in the parallel *BABAR* analysis [69].

Using the $\phi(1020) \to K^+K^-$ and $\chi_{c0} \to K^+K^-$ branching fractions given in [9] the overall branching fractions for $B^\pm \to \phi(1020)K^\pm$ and $B^\pm \to \chi_{c0}K^\pm$ are calculated to be $(8.6 \pm 1.3 \pm 0.6 \pm 0.1) \times 10^{-6}$ and $(3.1 \pm 0.9 \pm 0.2 \pm 0.3) \times 10^{-4}$, where the final error is due to the uncertainty on the branching fraction. Both are consistent with previous measurements ([17], [34], [35], [36]). It is worth noting that of the two solutions for χ_{c0} the "A" solution ($(2.1 \pm 0.6 \pm 0.2 \pm 0.2) \times 10^{-4}$) is consistent with the PDG average of $(1.6^{+0.5}_{-0.4})$, whereas the "B" solution ($(4.1 \pm 0.9 \pm 0.3 \pm 0.5) \times 10^{-4}$) is not.

The asymmetry results are all consistent with zero, which is consistent with previous experiments ([32], [35], [36], [69]). Current experimental uncertainties are however too high to be able to probe the theoretical asymmetries predicted by [19] and [23].

This analysis has seen evidence of an unknown state at around $1.5\,\mathrm{GeV}/c$. Also a relatively large branching fraction for $B^\pm \to f_0(980)K^\pm$; $f_0(980) \to K^+K^-$has been measured, albeit with large uncertainty. With improved statistics, and if a way can be found to eliminate the fit biases seen in this analysis, there is definitely the potential to reduce these uncertainties greatly. It would be interesting to fit to the model proposed by Minkowski and Ochs to examine whether it would be a better fit to the data, and whether the current nonresonant model could be dispensed with in favour of a more traditional flat model.

With relatively unknown states taking up almost 90% of the Dalitz plot there is obviously plenty of scope for further investigation.

References

[1] T.D. Lee and C.N. Yang. Question of parity conservation in weak interactions. *Phys. Rev.*, 104:254–258 (1956).

[2] T.D. Lee and C.N. Yang. Nobel lectures (1957).

[3] C.S. Wu *et al.* Experimental test of parity conservation in beta decay. *Phys. Rev.*, 105:1413–1414 (1957).

[4] B.L. Ioffe, L.B. Okun and A.P. Rudik. *Soviet Phys. JETP*, 5:327 (1957).

[5] J.H. Christenson *et al.* Evidence for the 2π decay of the K_2^0 meson. *Phys. Rev. Lett.*, 13:138–140 (1964).

[6] A. Angelopoulos *et al.* (CPLEAR). First direct observation of time-reversal non-invariance in the neutral kaon system. *Phys. Lett.*, B444:43–51 (1998).

[7] M. Kobayashi, and T. Maskawa. *CP* violation in the renormalizable theory of weak interaction. *Prog. Theor. Phys.*, 49:652–657 (1973).

[8] Wolfenstein, Lincoln. Parameterization of the Kobayashi-Maskawa matrix. *Phys. Rev. Lett.*, 51:1945 (1983).

[9] S. Eidelman *et al.* Review of Particle Physics. *Phys. Lett.*, B592 (2004).

[10] P.F. Harrison and H.R. Quinn (*BABAR*). The *BABAR* Physics Book: Physics at an asymmetric B factory. pages 1–40 (1998).

[11] B. Aubert *et al.* (BaBar). Observation of direct *CP* violation in $B^0 \to K^+\pi^-$ decays. *Phys. Rev. Lett.*, 93:131801 (2004). `hep-ex/0407057`.

[12] J. Charles *et al.* (CKM Fitter). CKMfitter Group (updated results and plots available at: http://ckmfitter.in2p3.fr). *Eur. Phys. J.*, C41:1–131 (2005). `hep-ph/0406184`.

[13] E. Barberio *et al.* (Heavy Flavor Averaging Group (HFAG)). Averages of b-hadron properties at the end of 2005 (2006). `hep-ex/0603003`.

[14] M. Neubert. B physics and *CP* violation. *Int. J. Mod. Phys.*, A11:4173–4240 (1996). `hep-ph/9604412`.

[15] R. H. Dalitz. On the Analysis of τ-Meson Data and the Nature of the τ-Meson. *Phil. Mag.*, 44:1068 (1953).

[16] R. A. Briere *et al.* (CLEO). Observation of $B \to \phi K$ and $B \to \phi K^*$. *Phys. Rev. Lett.*, 86:3718 (2001). `hep-ex/0101032`.

[17] B. Aubert *et al.* (BABAR). Measurements of the branching fractions and charge asymmetries of charmless three-body charged B decays. *Phys. Rev. Lett.*, 91:051801 (2003). `hep-ex/0304006`.

[18] B. Aubert *et al.* (BABAR). Measurement of the branching fraction for $B^\pm \to \chi_{c0}K^\pm$. *Phys. Rev.*, D69:071103 (2004). `hep-ex/0310015`.

[19] M. Beneke and M. Neubert. QCD factorization for $B \to PP$ and $B \to PV$ decays. *Nucl. Phys.*, B675:333–415 (2003). `hep-ph/0308039`.

[20] A. Datta *et al.* Methods for measuring new-physics parameters in B decays. *Phys. Rev.*, D71:096002 (2005). `hep-ph/0406192`.

[21] C. Chen, Y. Keum and H. Li. Perturbative QCD analysis of $B \to \phi K$ decays and power counting. *Phys. Rev.*, D64:112002 (2001). hep-ph/0107165.

[22] H. Y. Cheng and K. C. Yang. Analysis of $B \to \phi K$ decays in QCD factorization. *Phys. Rev.*, D64:0074004 (2001). hep-ph/0012152.

[23] D. S. Du, H. J. Gong, J. F. Sun, D. S. Yang and G. H. Zhu. Phenomenological analysis of charmless decays $B \to PV$ with QCD factorization. *Phys. Rev.*, D65:094025 (2002). hep-ph/0201253.

[24] C. Chiang, M. Gronau, Z. Luo, J. L. Rosner and D. A. Suprun. Charmless $B \to VP$ decays using flavor SU(3) symmetry. *Phys. Rev.*, D69:034001 (2004). hep-ph/0307395.

[25] H. Y. Cheng and K. C. Yang. $B \to f_0(980)K$ decays and subleading corrections. *Phys. Rev.*, D71:054020 (2005). hep-ph/0501253.

[26] P. Colangelo, F. De Fazio and T. N. Pham. $B^- \to K^-\chi_{c0}$ decay from charmed meson rescattering. *Phys. Lett.*, B542:71 (2002). hep-ph/0207061.

[27] S. M. Flatté. Coupled-channel analysis of the $\pi\eta$ and $K\bar{K}$ systems near $K\bar{K}$ threshold. *Phys. Lett.*, B63:224 (1976).

[28] M. Ablikim *et al.* (BES). The σ pole in $J/\psi \to \omega\pi^+\pi^-$. *Phys. Lett.*, B598:149–158 (2004). hep-ex/0406038.

[29] E. M. Aitala *et al.* (E791). Study of the $D_s^+ \to \pi^-\pi^+\pi^+$ decay and measurement of f_0 masses and widths. *Phys. Rev. Lett.*, 86:765–769 (2001). hep-ex/0007027.

[30] T. A. Armstrong *et al.* (WA76). Study of the centrally produced $\pi\pi$ and $K\bar{K}$ systems at 85 and 300 GeV/c. *Z. Phys.*, C51:351–364 (1991).

[31] Heavy Flavor Averaging Group. URL http://www.slac.stanford.edu/xorg/hfag/.

[32] B. Aubert *et al.* (BABAR). Dalitz-Plot Analysis Of The Decays $B^{\pm} \to K^{\pm}\pi^{\mp}\pi^{\pm}$. *Phys. Rev.*, D72:072003 (2005). hep-ex/0507004.

[33] B. Aubert *et al.* (BABAR). An Amplitude analysis of the decay $B^{\pm} \to \pi^{\pm}\pi^{\pm}\pi^{\mp}$. *Phys. Rev.*, D72:052002 (2005). hep-ex/0507025.

[34] A. Garmash *et al.* (BELLE). Dalitz Analysis of the Three-Body Charmless Decays $B^+ \to K^+\pi^+\pi^-$ and $B^+ \to K^+K^+K^-$. *Phys. Rev.*, D71:092003 (2005). hep-ex/0412066.

[35] B. Aubert *et al.* (BABAR). Measurements of branching fractions in $B \to \phi K$ and $B \to \phi\pi$ and search for direct *CP* violation in $B^{\pm} \to \phi K^{\pm}$. *Phys. Rev.*, D69:01110291 (2004). hep-ex/0309025.

[36] D. Acosta *et al.* (CDF). First evidence for $B_s^0 \to \phi\phi$ decay and measurements of branching ratio and A_{CP} for $B^+ \to \phi K^+$. *Phys. Rev. Lett.*, 95:031801 (2005). hep-ex/0502044.

[37] W. Kozanecki. The PEP-II B-factory: Status and prospects. *Nucl. Instrum. Meth.*, A446:59–64 (2000).

[38] An Asymmetric B factory based on PEP: Conceptual design report. SLAC-0372.

[39] J. T. Seeman. PEP-II performance and plans. URL http://www.slac.stanford.edu/BFROOT/www/Organization/Spokespe%rson/P5rehearsals/seeman.ppt.

[40] M. Sullivan. PEP-II monthly integrated luminosity. URL http://www.slac.stanford.edu/grp/ad/pep-ii/stats/Lum_PEP-II_m%onthly.pdf.

[41] B. Aubert *et al.* (BABAR). The *BABAR* detector. *Nucl. Instrum. Meth.*, A479:1–116 (2002). hep-ex/0105044.

[42] A. Snyder. Effect of Vertex Cuts on CP Reach (1994). *BABAR* Note #177.

[43] A. J. S. Smith *et al.* A barrel IFR instrumented with limited streamer tubes. URL `http://www.slac.stanford.edu/BFROOT/www/Detector/LST/document%ation/LSTprop-A4-May30-ajss.pdf`.

[44] D.J. Lange and A. Ryd. EvtGen documentation (2003). *BABAR* Analysis Document #522.

[45] Torbjörn Sjöstrand. PYTHIA 5.7 and JETSET 7.4. URL `http://dino.ip.fmph.uniba.sk/pythia_html3/pythia57.html`.

[46] S. Agostinelli *et al.* (GEANT4). GEANT4: A simulation toolkit. *Nucl. Instrum. Meth.*, A506:250–303 (2003).

[47] P. Billoir. Track Fitting With Multiple Scattering: A New Method. *Nucl. Instr. Meth.*, A225:352 (1984).

[48] G. Mancinelli and S. Spanier. Kaon selection at the *BABAR* experiment (2001). *BABAR* Note #116.

[49] S. Eidelman *et al.* Review of Particle Physics. *Phys. Lett.*, B592:242 (2004).

[50] *BABAR* Particle ID webpage. URL `http://www.slac.stanford.edu/BFROOT/www/Physics/Tools/Pid/pid%.html`.

[51] W. T. Ford. Choice of kinematic variables in B meson reconstruction - Take 3 (2000). *BABAR* Analysis Document #53.

[52] K. Flood, G. Blaylock and J. Joyce. Thrust calculation at *BABAR* (2001). *BABAR* Analysis Document #305.

[53] R. A. Fisher. The use of multiple measurements in taxonomic problems. *Annals Eugen.*, 7:179–188 (1936).

[54] J. Beringer. A multivariate tagging algorithm with categories based on the physics of the B_{tag} decay (2002). *BABAR* Analysis Document #317.

[55] F. Wilson. Charmless Hadronic B-Decays NonCharm3BodyUser Instructions. URL `http://www.slac.stanford.edu/BFROOT/www/Physics/Analysis/AWG/%chrmls_hadronic/ThreeBody/Software/NonCharm3BodyUser_cm2.html`.

[56] ROOT, an object oriented data analysis framework. URL `http://root.cern.ch/`.

[57] M. Barrett and A. Hart. Analysis of the $B^{\pm} \to K^{\pm}K^{\mp}K^{\pm}$ Dalitz Plot (2006). *BABAR* Analysis Document #865.

[58] P. Harrison and J. Back. Laura++: The Likelihood Analysis Unbinned Reconstruction of Amplitudes Package. URL `http://www.slac.stanford.edu/BFROOT/www/Physics/Analysis/AWG/%chrmls_hadronic/ThreeBody/Software/Laura++/index.html`.

[59] J. Back. LAURA++ Manual - Likelihood Analysis Unbinned Reconstruction of Amplitudes (2004). *BABAR* Analysis Document #806.

[60] F. James and M. Roos. 'MINUIT' A System For Function Minimization and Analysis of the Parameter Errors and Correlations. *Comput. Phys. Commun.*, 10:343–367 (1975).

[61] C. Zemach. Three Pion Decays of Unstable Particles. *Phys. Rev.*, 133:B1201 (1964).

[62] C. Zemach. *Phys. Rev.*, 140:B97 (1965).

[63] H. Albrecht *et al.* (ARGUS). Exclusive hadronic decays of B mesons. *Z. Phys.*, C48:543–552 (1990).

[64] A. Dvoretskii. Dalitz Plot Analysis of Charmless Three Body B Decays $B^+ \to K^+h^+h^-$ ($h = K/\pi$) (2006). *BABAR* Analysis Document #643.

[65] Blatt, J. and Weisskopf, V. E. *Theoretical Nuclear Physics.* J. Wiley (New York) (1952).

[66] H. Y. Cheng and K. C. Yang. Nonresonant three-body decays of D and B mesons. *Phys. Rev.*, D66:054015 (2002). `hep-ph/0205133`.

[67] S. Fajfer, T. Pham and A. Prapotnik. *CP* Violation in the Partial Width Asymmetries for $B^- \to \pi^+\pi^-K^-$ and $B^- \to K^+K^-K^-$ Decays. *Phys. Rev.*, D70:034033 (2004). `hep-ph/0405065`.

[68] C. Hearty. Measurement of the Number of $\Upsilon(4S)$ Mesons Produced in Run 1 (B Counting) (2001). *BABAR* Analysis Document #134.

[69] B. Aubert *et al.* (BABAR). Dalitz plot analysis of the decay $B^\pm \to K^\pm K^\pm K^\mp$. *Phys. Rev.*, D74:032003 (2006). `hep-ex/0605003`.

[70] B. Aubert *et al.* (BABAR). Branching fractions and *CP* asymmetries in $B^0 \to K^+K^-K^0_S$ and $B^+ \to K^+K^0_SK^0_S$. *Phys. Rev. Lett.*, 93:181805 (2004). `hep-ex/0406005`.

[71] P. Minkowski and W. Ochs. B decays into light scalar particles and glueball. *Eur. Phys. J.*, C39:71–86 (2005). `hep-ph/0404194`.